Historical Perspective

Data evaluation for surface-sensitive label-free methods to obtain real-time kinetic and structural information of thin films: A practical review with related software packages

Andras Saftics [a,*], Sándor Kurunczi [a], Beatrix Peter [a], Inna Szekacs [a], Jeremy J. Ramsden [b], Robert Horvath [a,*]

[a] *Nanobiosensorics Laboratory, Institute of Technical Physics and Materials Science, Centre for Energy Research, 29-33 Konkoly-Thege Miklós út, H-1121 Budapest, Hungary*
[b] *Clore Laboratory, University of Buckingham, MK18 1EG, United Kingdom*

ARTICLE INFO

ABSTRACT

Interfacial layers are important in a wide range of applications in biomedicine, biosensing, analytical chemistry and the maritime industries. Given the growing number of applications, analysis of such layers and understanding their behavior is becoming crucial. Label-free surface sensitive methods are excellent for monitoring the formation kinetics, structure and its evolution of thin layers, even at the nanoscale. In this paper, we review existing and commercially available label-free techniques and demonstrate how the experimentally obtained data can be utilized to extract kinetic and structural information during and after formation, and any subsequent adsorption/desorption processes. We outline techniques, some traditional and some novel, based on the principles of optical and mechanical transduction. Our special focus is the current possibilities of combining label-free methods, which is a powerful approach to extend the range of detected and deduced parameters. We summarize the most important theoretical considerations for obtaining reliable information from measurements taking place in liquid environments and, hence, with layers in a hydrated state. A thorough treatmaent of the various kinetic and structural quantities obtained from evaluation of the raw label-free data are provided. Such quantities include layer thickness, refractive index, optical anisotropy (and molecular orientation derived therefrom), degree of hydration, viscoelasticity, as well as association and dissociation rate constants and occupied area of subsequently adsorbed species. To demonstrate the effect of variations in model conditions on the observed data, simulations of kinetic curves at various model settings are also included. Based on our own extensive experience with optical waveguide lightmode spectroscopy (OWLS) and the quartz crystal microbalance (QCM), we have developed dedicated software packages for data analysis, which are made available to the scientific community alongside this paper.

Contents

* Corresponding authors.
E-mail addresses: andras.saftics@gmail.com (A. Saftics), r74horvath@gmail.com (R. Horvath).

1. Introduction

Interaction between molecules in solution and on a solid surface is a common phenomenon. To understand surface adsorption processes at the solid–liquid boundary is of significant importance in bioprocessing [1], biomaterial research [2], polymer science [3], nanotechnology [4], biochemistry [5], affinity measurements [6,7] and biosensing [8], biofilm formation [9], development of coatings such as antifouling surfaces [10,6], self-assembly [11], geochemistry [12], water quality sensing [13], electrochemistry [14], corrosion [15], catalysis [16] as well as in toxicity analysis [17], to name but a few.

Although many techniques have been developed to quantitatively assess composition, structure and chemical behavior of surfaces and adsorbates, nanoscale measurements in liquids are still challenging. The physical techniques most used to characterize the structure, particle size and porosity of solid materials are spectroscopic and ultramicroscopic methods [16], including X-ray, neutron and electron diffraction spectroscopies, transmission electron microscopy, extended X-ray absorption fine structure analysis as well as nuclear magnetic resonance (NMR), infrared, Raman and ultraviolet (UV)-Raman spectroscopies [18]. The structure and chemical composition of surfaces can be analyzed by low-energy electron diffraction, electron energy loss spectroscopy, X-ray photoelectron spectroscopy, Auger electron spectroscopy, low-energy ion scattering and secondary ion mass spectrometry. For investigation of surface reactivity and the nature of adsorbates, techniques including thermal methods, Mössbauer spectroscopy, X-ray absorption near-edge spectroscopy, molecular spectroscopies of probe molecules, electron paramagnetic resonance, magic angle spinning NMR, sum frequency generation spectroscopy, polarization modulation-infrared reflection-absorption spectroscopy, photoluminescence, single molecule spectroscopy, steady-state isotopic transient kinetic analysis and temporal analysis of products.

Quantitative assessment of the processes (i.e., calculating the rates of chemical reactions and bond strengths) is critically important. The main physicochemical characteristic of molecular interactions — the dissociation constant (K_d) — relates to the binding affinity, indicating the strength of interaction. Some theoretical methods can predict binding affinity from structural models. Traditional experimental techniques, such as X-ray crystallography and NMR spectroscopy, provide bulk information about interactions of molecules with atomic resolution.

However, the behavior of multicomponent systems at a surface can differ significantly from that in the bulk. Traditional surface techniques usually require the system under investigation to be in a vacuum and hence cannot be used to monitor the kinetics of interactions in a liquid.

Label-free surface sensitive methods are excellent candidates to monitor interaction processes in liquids, without the need to label the interacting molecules, as they generate signals merely by their physical presence on the sensing surface [19]. They are able to achieve outstanding detection limits (down to as little as 0.1 pg mm^{-2} of surface adsorbed material [20]), and they can be designed to rapidly provide large number of measurements, fulfilling the needs of high-throughput screening (HTS) projects, which are extremely needed for understanding complex biological systems [21]. Examples of these methods employing different measurement principles are optical waveguide lightmode spectroscopy (OWLS), the quartz crystal microbalance (QCM) and the biologically sensitive field-effect transistor (BioFET) [22]. Label-free sensors have been used to measure the interactions of a wide range of biomolecules [23] (proteins, nucleic acids, carbohydrates and lipids) as well as to measure the biological effects of other organic and inorganic compounds such as toxins [24] and ions [25]. In addition, these methods are capable of monitoring the effects of molecular interactions as a cellular response, both for large cell populations or even for single cells.

The term "biosensing" does not have a unique definition in the literature. The various definitions that have been proposed do have in common that a biological entity — molecule (e.g., a protein), virus or cell — must be involved, either as a receptor to capture an analyte, or as the analyte (e.g., the components of blood). In a typical surface sensitive label-free biosensor measurement, one component, the biorecognition element or also called as bioreceptor (an antibody, enzyme, DNA, aptamer, mammalian cell or microorganism) is at a fix position bound to the solid sensor (transducer) surface. Another component, the analyte, is driven over the receptor-sensitized surface in liquid phase inside a fluidic system [26,27]. Based on the transducer type, the adsorbed layer generates an optical, mechanical, or electrical signal, in which a wealth of valuable information may be contained. Intense research has been carried out to derive important physicochemical properties of the adsorbed layers from these signals.

What makes the quantitative analysis of biosensor response especially difficult is that these processes are running simultaneously and influenced by multiple experimental parameters. In such biosensing

systems, the main processes are convection, diffusion and reaction (adsorption or association). It is crucial to qualify that in which regime such systems work (e.g., reaction–limited versus diffusion–limited, rapid collection versus full retention) and provide robust approximate relations conveying how various relevant quantities scale as the system parameters change [26]. These systems are similar to heterogeneous catalytic reactions, studied by the chemical engineering community before the advent of immunoassay and biosensor technologies. Today, a wide range of label-free biosensor technologies capable of high-resolution kinetic measurements have been developed and many instruments are available commercially and are being continuously improved pushing higher throughput and lower detection limits as well as enabling nanostructural analysis and measurement in complex biofluids. Label-free methods have enhanced analytical performance that is especially exploited in biointeraction analysis (BIA) and has lead label-free methods to become essential tools in drug discovery. In this field most of the examined solid–liquid interfacial processes are on the borderline between of physisorption and chemisorption. Although non-covalent interactions drive the adsorption of biomolecules on solid surfaces (forming thin films or establishing affinity–based ligand–analyte (L–A) pairs), as they inevitably will be in biolayers in an aqueous environment, an abundance of hydrogen bonds is also involved, significantly increasing layer stability.

In this review we summarize the most important techniques, their theoretical foundations, and the characteristic nanostructural and kinetic features that can be obtained (e.g., thickness, refractive index, viscoelasticity and water content of adsorbed layers, kinetic and equilibrium adsorption constants). Our main aim is to provide the basic equations and experimentally relevant examples for those who are dealing with kinetic data generated by surface-sensitive methods. We focus on two highly representative examples of optical and mechanical sensors, OWLS and QCM. In the endeavor of detecting various characteristics simultaneously on an examined system, combination of the highly sensitive label-free methods serves as a particularly powerful solution. We discuss the currently available possibilities of combinations and review the gain that this approach can provide, especially in the characterization of heavily hydrated interfacial layers.

Based on our own extensive experience we developed data analysis packages for OWLS and QCM techniques. We show through representative examples of the main features of these new software tools and make them available for the scientific community as a platform for evaluation of raw data and kinetic analysis. As we shall see, this evaluation approach provides comprehensive details of the adsorption process and the building up of interfacial layers.

Looking at the structure of this review, first we outline various label-free biosensors in Section 2, including measurement principles and important quantities that the presented techniques can measure and are characteristic to the examined layers. In Section 5, we describe that how one can extract structural information from the obtained biosensor data, and then in Section 3, we review the basic theory of kinetic modeling and go through the most significant circumstances that potentially influence the results from kinetic evaluation. In Section 4, we demonstrate the previous model considerations on the evaluation of real measurement data and simulating various model conditions. Finally, we dedicate Section 6 to present our developed software packages.

2. Surface-sensitive label-free techniques to monitor the solid–liquid interface

Label-free biosensors have powerful capabilities to monitor the dynamic behavior of binding to surfaces. In contrast to end-point biochemical assays (e.g., the enzyme-linked immunosorbent assay, ELISA), they provide real-time kinetic data about processes occurring at, and in close vicinity to, a surface. Besides detecting analytes and measuring their binding kinetics to immobilized receptors like antibodies, biosensor methods can also be used to unravel the structure

(e.g., chain conformation) of thin hydrated biolayers, delivering invaluable support for biomaterials research [28–30]. The best-established techniques capable of measuring kinetic data are optical biosensors [36], but mechanical or electrochemical transduction can also be used. In a typical label-free setup, the sensor "chip" comprising the adsorbing receptor surface is assembled with a flow cell connected to an injection system (e.g., peristaltic or syringe pump) that maintains a continuous flow of the analyte solution (the analyte being an ion, biomolecule, nanoparticle or cell). The "chip" also comprises the transducer that determines how the solid–liquid interface at which adsorption takes place is probed. A typical biosensor measurement cycle consists of three phases: (i) running a baseline when stable signal is reached on the surface equilibrated with the analyte-free liquid (usually an aqueous buffer solution), (ii) followed by the association (adsorption) process starting with the injection of analyte solution, (iii) and then finally dissociation (desorption or washing) process starting with the injection of analyte-free liquid again. Although most kinetic models in the literature take dissociation to be a first order process, only a minority of investigated systems actually follow such a law; many biochemical interactions are so strong that it would be necessary to wait for many days for dissociation to be complete and for the measurement to revert to the baseline upon washing [31].

In this section we provide an overview of the principles of the established label-free techniques (OWLS and QCM) suitable for kinetic and structure measurements. Then we review the latest developments in cutting-edge technologies and the possibilities offered by combining different classical setups.

2.1. Detection principles and major representatives

Optical methods detect refractive index (RI) changes, mechanical methods detect mass changes and electrochemical methods measure changes in charge distribution [32,294. A summary of representatives of these methods is shown in Fig. 1. Although the variety of biosensors is quite large, only a few achieved significant success, as manifested by commercial instruments widely used in laboratories around the world — surface plasmon resonance (SPR), OWLS, dual polarization interferometry (DPI) and QCM, which all have an extensive literature both regarding theory and applications [28,32–36].

Optical methods measure RI changes originating from the close vicinity of the sensor surface. Sensing is established through the evanescent electromagnetic (EM) field formed by the EM wave coupled into an optical transducer film. The evanescent field extends over the film surface and dies away with an exponentially decaying field intensity. Most commonly, the evanescent field is generated by surface plasmons of a metal layer excited using an irradiating light beam (SPR–based methods, Fig. 1 A) or by an EM wave propagating in a waveguide film by a series of total internal reflections (waveguide–based methods, Fig. 1 B, C). The great advantage of these techniques is that they offer high sensitivity by probing a large surface area only in the close vicinity of the surface (typically within a thickness of 100–200 nm). Local optical density changes in the evanescent field change the velocity and phase of the EM wave. In general, the detected response signal R is proportional to the total RI shift Δn at up to a distance z from the surface [37]:

$$R \propto \int_0^z \Delta n \cdot e^{-z/\sigma} \mathrm{d}z \qquad (1)$$

Here, σ denotes the field decay length (penetration depth). Measuring the polarization state of an incident EM wave reflected from a substrate surface is an alternative optical method for probing tiny RI changes on the surface. This principle is exploited in ellipsometry, shown in Fig. 1 D. Although ellipsometry is capable of measuring the kinetics of biolayer formation, it has remained a complementary technique rather than a standalone biosensor, due to its moderate sensitivity and the complicated optical models needed for evaluating the raw data.
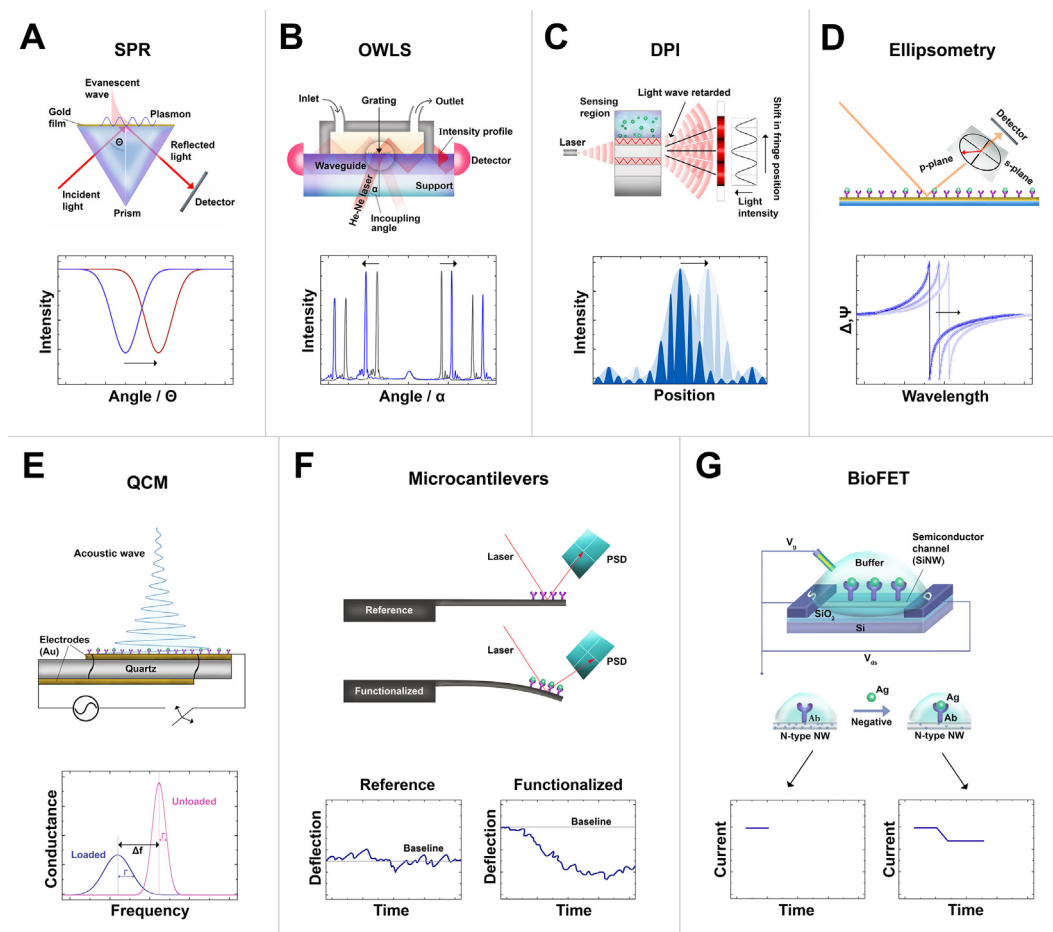
Fig. 1. Detection principle of label-free biosensor methods. All subfigures involve a visualization of the most relevant part of the biosensor (positioned in the top) as well as a graph (underneath) showing the raw measurement data that includes the biointeraction signal. A. SPR biosensor. The surface plasmons are excited by the incident light coupled in by a prism. The intensity of reflected light is measured by a photodetector. At a specific angle Θ where surface plasmons are excited, intensity minimum is recorded in the angle-spectrum. B. OWLS. Discrete waveguide modes (TE and TM polarizations) are excited by an incident laser light coupled into the waveguide film via an optical grating. Resonance peaks are detected at two incident angles α termed incoupling angles, corresponding to the two waveguide mode polarizations. C. DPI. The end face of the sensor chip is broadly illuminated by laser light coupled into the two waveguide films (top: sensing, down: reference waveguide) in which TE and TM modes are excited. The beams coupled out from the waveguides interfere with each other resulting in a 2D interference pattern detected in the far field on a charged coupled device (CCD) array. D. Spectroscopic ellipsometry. The ellipsometric angles Ψ and Δ characterizing the polarization state of light reflected from the sample surface are detected as a function of the incident light wavelength. E. QCM. The shear mode oscillation of the quartz crystal generates a standing acoustic plane wave. Resonance peaks are detected as a function of frequency and the resonance frequency is detected together with the band width of the resonance peak. F. Microcantilevers. An incident laser beam is reflected from the cantilever towards a position sensitive detector (PSD) measuring the cantilever deflection due to an added mass as a function of time. G. BioFET. The source (S) and drain (D) electrodes are connected with a silicon nanowire (SiNW) semiconductor channel which is the sensing element of the device. In the case of an n-type SiNW, the binding of a negatively charged biomolecule results in a drop in the measured electrical current. The diagrams and graphs are adapted from the below listed references. [(D-E) Adapted from Ref. [28], copyright 2018 AIP Publishing, used under CC BY 4.0; (F) from Ref. [42], copyright 2015 Springer; (G) from Ref. [43], copyright 2014 de Gruyter]

Biosensors with mechanical transduction principle are often termed acoustic wave devices as their detection method is based on the generation of standing acoustic waves by mechanical oscillation of the transducer. The most successful representation of mechanical transduction is the QCM technique (Fig. 1 E), which offers sensitive measurement with robust interrogation of the piezoelectric quartz crystal sensor chip. Other mechanical methods, like microcantilevers (Fig. 1 F) have failed to provide stable and reproducible kinetic signals and have not become popular for kinetic measurements, whereas QCM has amply demonstrated its potential, especially for investigating the highly hydrated layers formed by synthetic polymers or biomaterials [38–40].

Translating the presence of biomolecules to an electrical signal is an alternative label-free detection method [32]. Field-effect transistor (FET) technology is quite promising as a transducer [43]. The biosensor-related realization is usually termed a BioFET. Charged biomolecules adsorbing on a semiconductor channel change the local surface charge density and thus the conductivity of the semiconductor, resulting in a shift in the measured electrical current (Fig. 1 G). The above list of label-

free methods capable of monitoring adsorption kinetics is not complete. Such additional techniques (e.g., streaming potential measurement [41]) is outside the scope of this review.

2.1.1. Surface plasmon resonance (SPR) biosensor and biointeraction analysis (BIA)

SPR is probably the most common label-free biosensor technique — it was the earliest to be commercialized and has been aggressively marketed. SPR biosensors exploit the charge-density oscillation excited by EM waves at the interface of two media which have dielectric constants of opposite signs, like a metal (gold) and a dielectric (glass) [32, 44]. For a basic SPR setup, see Fig. 1 A. Due to the enormous literature about SPR–based biosensing [44–46], we do not feel that it is necessary to go into further details here. A few additional comments are made in Section 2.1.2. One important point that has received less attention than would be appropriate is that, because of the intrinsically low sensitivity of SPR (about an order of magnitude less than that is achievable by waveguide–based methods [47]) it was found necessary to "fill the

evanescent field" by coating the gold layer in which the surface plasmons resonate with a thick layer of a dextran hydrogel to which the receptors could readily be immobilized. This greatly increased the number of binding events that could be sensed and compensated for the low intrinsic sensitivity. The development was favored by the circumstance that a major product of the company, Pharmacia AB, which was the first to successfully develop a commercial SPR instrument (Biacore) was the Sephadex range of dextrans. Hence there was great in-house expertise in the manipulation of such materials. A parallel advantage was that binding took place in a quasi-three-dimensional medium (the volume fraction of the dextran being very small), allowing the homogeneous binding kinetics familiar to biochemists to be used for data analysis. It was not initially realized that the hydrogel exerts Hofmeister-like effects [48] on the medium, which can significantly chemically alter ligand–receptor interactions compared with those in pure water. At the same time diffusion within the hydrogel is not unhindered as in bulk solution, which affects the overall binding kinetics through its influence on transport [49]. On the other hand, the hydrogel somewhat mimics cytoplasm, in which many of the reactions studied with biosensors take place in reality, hence the hydrogel might be considered a more realistic medium than aqueous buffer.

Of note, immobilization can heavily alter the local environment of the immobilized molecules changing their binding properties compared to interaction values measured in bulk solution. A recent systematic study using GCI illuminated that the k_a rate and K_d values of the binding events are heavily influenced, but the k_d values not [50]. This should be kept in mind when comparing the results of surface sensitive technologies to other methods measuring binding events in bulk solutions (for example, isothermal titration calorimetry [50–52]). The above observation about the tuned binding constants has been also observed in living cells when the local environment of the receptors were varied by enzymatic digestion of the glycocalyx [53].

In the nearly 700 million USD per year market of SPR biosensors [54], the industry leader position is occupied by Biacore, currently owned by the company Cytiva (Little Chalfont, UK; formerly part of GE Healthcare Life Sciences). The flagship instruments are Biacore S200 [55] in terms of leading sensitivity (reported baseline noise of <0.015 RU (resonance unit) $\approx$ 0.15 pg mm^{-2}) as well as Biacore 8 K+ [56] regarding throughput (samples can be measured on 12×384–well microplates in one run on an 8–channel sensor chip).

2.1.2. Optical waveguide lightmode spectroscopy (OWLS)

If an EM wave is confined into a thin layer which has a thickness less than the wavelength of incident light and RI higher than its surrounding media, and the wave is coupled into the layer allowing constructive interference between the waves reflected from the two interfaces facing each other, discrete waveguide modes can propagate [32]. Versatile incoupling and readout methods have made waveguide–based transduction technology a leader in the field of biosensors, which also demonstrates great promise for the development of new generation biosensors (see later Section 2.2.5). Unlike SPR, which early on became dominated by large commercial instrument makers who strove after ease of use rather than biophysicochemical insight, many OWLS users have built their own equipment. Commercial instrument companies making OWLS apparatus are small and have worked closely with cutting-edge researchers to develop their instruments. This happy circumstance has undoubtedly facilitated the development of the new generation of biosensing technology (Section 2.2.5).

In OWLS, the evanescent EM field is generated by coupling an external laser beam into the optical waveguide film of a planar sensor chip, as illustrated in Fig. 1 B. For the so-called monomode OWLS, the waveguide (F) is typically a 160–200 nm thick high-RI (e.g., SiO$_2$–TiO$_2$) dielectric film (S) deposited on silica or alkali-free glass (e.g., AF45 glass) using the sol–gel technique or physical vapor deposition. The light is coupled into the waveguide through an optical grating embossed or written into the waveguide film. The read-out is based on scanning

the angle of the incident beam by a precision goniometer and recording the discrete incoupling angles (α) at which waveguide modes are excited, i.e. at which propagating standing electromagnetic waves are formed in the waveguiding layer. In monomode OWLS, the zeroth order mode of each of the two possible polarization states can be excited, namely the transverse electric (TE) and transverse magnetic (TM) modes. The excitation of modes is detected by continuously measuring the intensity of light leaving the ends of the optical chip. It is preferable to place a photodiode at both ends in order to compensate for any variation of grating alignment. Furthermore, measuring two α values independently, with the two oppositely placed photodiodes, makes it possible to determine the exact values of the incident angles by determining and taking into account the autocollimation angle (that corrects the perpendicular incident angle to 0°), use of which cannot be avoided due to the high angular precision required by OWLS. This enables OWLS to work without the need for any calibration, making it unique among the evanescent wave–based label-free techniques. If excited, intensity peaks appear in the angle-spectrum (Fig. 1 B). The incoupling angle α depends on the effective RIs of the waveguide, N_{TE} and N_{TM}. The definition of N_{TE} and N_{TM} involves the optogeometrical parameters of all the layers through which light passes, including the RI of air (n_0), substrate (n_S) and covering sample medium (n_C), as well as the RI and thickness of the waveguide film (n_F, d_F) and adsorbed layer (n_A, d_A). Any RI variation in the evanescent field that may originate, e.g., from a new liquid medium or biomolecule adsorption, results in change of N and detunes α. The incoupling angles are recorded sequentially, hence surface events can be monitored in real time. By recording α_{TE} and α_{TM}, one can determine N_{TE} and N_{TM}, and thus the n_A and d_A parameters of the target layer. The relation between N_{TE} and N_{TM} as well as n_A and d_A is described by the 4–layer mode equation. The exact values of n_F and d_F are usually determined from the baseline section of the recording, during which analyte-free solution flows over the surface. If n_C and n_S are known, n_F and d_F can be calculated using the 3–layer mode equation.

The RI of many pure liquids, including water, have been extensively researched and tabulated values and interpolation formulae are available for all relevant wavelengths and temperatures. The RI of unknown liquids and solutions can be independently measured by a refractometer, or can be calculated from Eq. (2) if the RI of the medium in which the adsorbing molecules are dissolved (n_{medium}), the concentration of the bulk solution (c_B) and the RI increment dn/dc of the solution are known:

$$n_B = n_{medium} + c_B \mathrm{d}n/\mathrm{d}c \tag{2}$$

Here, dn/dc is defined as the slope of an n_B vs. c_B graph and its value can be simply determined by refractometric measurements of analyte solutions prepared at different concentrations. Early work with proteins suggested that a "universal" value of 0.1840 mL g^{-1} obtained [57], but this was later shown to be erroneous on both theoretical and experimental grounds [58]: dn/dc depends on both the actual protein (its atomic and bond composition) and the solvent — usually an aqueous buffer. A considerable compilation of dn/dc values of different biomolecules has been made [59]. Using the determined n_A and d_A values, the surface mass density M can be calculated by the de Feijter's formula as follows [57]:

$$M = d_A \frac{n_A - n_{solvent}}{\mathrm{d}n/\mathrm{d}c} \tag{3}$$

The two guided lightmode polarization states enable the measurement of two independent waveguide characteristics, N_{TE} and N_{TM}, and thus the determination of two optogeometrical parameters of the adlayer, n_A and d_A. The fact that the TE and TM modes are sensitive to the overall orientation of components in the adlayer enables nanoscale conformational changes to be examined (details in Section 5). These capabilities make the OWLS a powerful technique for the simultaneous

analysis of both layer formation kinetics and its nanostructure [60–62]. Such a structural analysis is not possible by a conventional SPR biosensor, as only the TM mode can propagate and hence only a single polarized mode (N_{TM}) can be monitored. Thus, n_A and d_A cannot be separated and M is determined according to an approximate "calibration" of the SPR signal (typically 1 RU ≈ 1 ng cm^{-2} is used) [63]. The OWLS 210 biosensor system of MicroVacuum Ltd. [64] (Budapest, Hungary) offers a detection limit < 1 ng cm^{-2} and the independent measurement of n_A and d_A. OWLS has been used for the kinetic and structural analysis of protein adsorption [65–69], DNA [70–72] and synthetic polymer [73,74] layers as well as measuring the kinetics of living mammalian [75,76,299] and bacterial [77,78] cell adhesion. OWLS is popular in membrane protein and lipid studies. For instance, with this technique it is possible to investigate the formation of lipid bilayers from vesicles [79], lipid bilayer structures [80,297,300], the affinity and kinetics of protein–lipid interactions [81,82], and structural changes during such interactions [83].

2.1.3. Dual polarization interferometry (DPI)

Similar to OWLS, dual polarization interferometry (DPI) is a real-time and quantitative analytical technique that allows the RI and thickness of thin films and molecular layers adsorbed on a waveguide surface to be measured [84–86]. As with OWLS, DPI is a very sensitive method with a dimensional resolution of an order of ångströms perpendicular to the plane of the waveguide [84]. The principle of the DPI technique is that a laser light is divided into two beams which enter into two vertically stacked single-mode planar waveguides, a sensing and a reference one; recombination of the two beams in the far field creates a two-dimensional interference pattern. To excite alternately the two orthogonal polarization modes of the waveguides, the linearly polarized laser is rotated. The thickness of the adsorbed layer and the RI can be calculated by measuring the interferogram for both polarizations. If the polarization is switched rapidly, conformational changes associated with molecular interactions can be observed in real-time. DPI has been used in membrane protein and lipid studies. For instance, with this technique it is possible to investigate the formation of lipid structures [87].

A typical DPI setup uses three flow channels, one of which is a reference channel. In the reviewed studies about detection of protein structure changes, binding events, etc., the most used DPI instruments are the AnaLight Bio200 and AnaLight 4D from Farfield Group Ltd. (UK) [85,88–90], although this company has been declared insolvent and dissolved. It had declared that the AnaLight Bio200 gives quantitative data on real-time changes in thickness with a resolution of 0.1 Å and surface density with a resolution of 0.1 pg mm^{-2} of the immobilized layer [91], implying that the instrument can detect small molecules with a molecular weight below 100 Da with a mass resolution of 5 Da. Indeed, bisphenol A specific aptamer was immobilized on the sensor chip surface through biotin–avidin interaction, and the limit of detection (LOD) for bisphenol A concentration measurement was determined. Using the mass as well as thickness signals, 1.7 μM and 2.5 μM of LOD values were separately demonstrated [92]. The software provided with the instrument facilitates comprehensive analysis of both structural changes and interaction kinetics in quantitative units. Although DPI can only handle layers formed *in situ*, the multiple path length dual polarization interferometer (MPL-DPI) has the ability to characterize layers coated *ex situ*, which increases the number of condensed matter systems that can be studied; sample preparation may be easier too [93].

2.1.4. Quartz crystal microbalance (QCM)

QCM employs a vibrating element (resonator) whose mechanical oscillation generates bulk acoustic waves (BAW) propagating inside the resonator and extending beyond its surface. The resonator is an AT-cut quartz crystal disk mounted between gold electrodes on its two sides. Applying AC voltage through the resonator induces shear mode oscillation within the crystal via the piezoelectric effect, generating standing acoustic plane waves with a propagation direction normal to the surface. This shear wave propagates through the crystal and extends beyond its boundary with an exponentially decaying intensity. Besides vibrating at the fundamental resonance frequency, overtone oscillations are also generated. The crystal structure permits only odd overtone resonance frequencies (f_n) to be excited, defined by:

$$f_n = n\frac{v}{2d_Q} = n\frac{v}{\lambda} \tag{4}$$

where n denotes the overtone number ($n = 1, 3, 5, 7$, etc.), d_Q is the thickness of the quartz disk, v is the velocity and λ is the oscillation wavelength. The penetration depth of the acoustic wave is the largest at the fundamental frequency (around 250 nm) and decays with the overtone number [94]. If an adlayer is formed on the surface, it detunes the resonance frequency. A viscoelastic adlayer generate energy dissipation during the oscillation at the corresponding odd overtone characterized by another measured parameter, the dissipation factor (D_n). For the measurement of f_n and D_n, most QCM instruments use one of two different readout methods [95,96]: (i) an impulse excitation (ring-down) method measuring the decay of the crystal oscillation after the excitation is turned off; or (ii) an impedance analysis method measuring the impedance frequency spectrum with a network analyzer. Both techniques realize simultaneous measurement of the shift in f_n and D_n at each measurement epoch, where the shift at time t is defined as: $\Delta f_n = f(t) - f(t = 0)$, $\Delta D_n = D(t) - D(t = 0)$, respectively.

The best-known QCM system, the QCM-D (QCM with dissipation monitoring, Biolin Scientific AB [97] (Gothenburg, Sweden)) measures using the ring-down procedure [98,99]. The applied driving voltage is intermittently terminated inducing a decay in the crystal oscillation. Fitting the recorded amplitude results in fit parameters of decay time (τ) and f_n, allowing the calculation of D_n:

$$D_n = \frac{1}{\pi f_n \tau_n} = \frac{U_{dissipated}}{2\pi U_{stored}} \tag{5}$$

where $U_{dissipated}$ the energy dissipated in one oscillation cycle and U_{stored} the energy stored in the oscillating system. An example for the impedance analysis method is the QCM-I system manufactured by MicroVacuum Ltd. [100]. Here, impedance spectra (conductance as a function of frequency) for the different overtones are measured, and the resonance peaks are fitted (see Fig. 1 E), where the fit parameters are the resonance frequency and the half-width at half-maximum (Γ). The dissipation factor can be expressed herein as [96]:

$$D_n = \frac{2\Gamma_n}{f_n} \tag{6}$$

The oscillation decay and the impedance spectrum measured in the time and frequency domain, respectively, are the Fourier transform of each other [95,295]. As such, D provided by the QCM-D and QCM-I readout methods are equivalent and can be evaluated using the same methods [95,96,295].

According to the simplest evaluation model of a thin and rigid adlayer, the detected Δf_n normalized with its corresponding overtone number ($\Delta f_n/n$) is proportional to the added surface mass per unit area:

$$M^S = -C\frac{\Delta f_n}{n} \tag{7}$$

called the Sauerbrey equation [101], where C is a mass sensitivity constant dependent on the physical properties of the quartz crystal (for a 5 MHz AT-cut crystal a value of $C = 17.7$ ng cm^{-2} Hz^{-1} is typically used [95]) and M^S is the surface mass density calculated with the Sauerbrey equation. The criteria for applying the Sauerbrey equation have been thoroughly discussed elsewhere [101,102]. Although they assume experimentally unrealistic conditions (e.g., the medium is vacuum), the

Sauerbrey equation has been found to be usable for the evaluation of measurements made in a liquid medium, where the adlayer is rigid and its thickness is only a few nm. However, when the adlayer is thick or is viscoelastic, the Sauerbrey equation significantly underestimates the mass deposited on the sensor surface. Many biomaterials are viscoelastic due to their tendency to bind a large amount of water. In order to accurately evaluate data measured on such biolayers, a more complex model explicitly incorporating viscoelasticity is needed, which involves ΔD_n for data evaluation. The viscoelastic case and the Sauerbrey limit can be well estimated by qualitative data analysis methods. As such, if there is a small dependence of $\Delta f_n/n$ on n or if the magnitude of ΔD_n is below 2×10^{-6} or, according to Reviakine et al., $\Delta D_n/(-\Delta f_n/n) << 4 \times 10^{-7}$ Hz, the adlayer can be treated as rigid [99,102–104].

To calculate the realistic mass of a viscoelastic adlayer beyond the Sauerbrey limit, a model considering the measured ΔD_n values is needed. Such a continuum mechanical model was developed by Voinova and co-workers. The model assumes that as a Kelvin–Voigt material, the viscoelastic adlayer can be described by an elastic (spring) and viscous (dashpot) element, holding that the crystal is fully elastic. The Voinova model [105] is mostly referred to as the standard Kelvin–Voigt model and it serves as the core model of the data analysis software of QCM-D, currently called *Dfind* (Biolin Scientific AB), formerly known as *QTools*). This model is a specialized case of a more comprehensive model [99,106]. In practice, the Voinova model takes both the measured Δf_n and ΔD_n for the calculation of three adlayer parameters: thickness (d_A), shear viscosity (η_A) and shear elastic modulus (μ_A), and it requires knowledge of the adlayer mass density (ρ_A). The model can be extended to consider multiple adlayers. The equations of this Kelvin–Voigt model are:

$$\xi_1 = \sqrt{-\frac{\omega_n^2 \rho_A}{\mu_A + i\omega_n \eta_A}}; \xi_2 = \sqrt{i\left(\frac{\omega_n \rho_B}{\eta_B}\right)} \tag{8a}$$

$$\alpha = \frac{\left(\frac{\xi_1}{\xi_2}\right)\left(\frac{\eta_A - i\mu_A}{\omega_n \eta_B}\right) + 1}{\left(\frac{\xi_1}{\xi_2}\right)\left(\frac{\omega_n \eta_B - i\mu_A}{\omega_n \eta_B}\right) - 1}; \beta = \xi_1 \left(\frac{\omega_n \eta_A - i\mu_A}{\omega_n}\right)\left[\frac{1 - \alpha \, \exp{(2\xi_1 d_A)}}{1 + \alpha \, \exp{(2\xi_1 d_A)}}\right] \tag{8b}$$

$$\Delta f_n = \text{Im}\left(\frac{\beta}{2\pi \rho_Q d_Q}\right) \tag{9a}$$

$$\Delta D_n = -\text{Re}\left(\frac{\beta}{\pi f_n \rho_Q d_Q}\right) \tag{9b}$$

where ω is the angular frequency ($\omega_n = 2\pi f_n$) and i is the imaginary unit. The method of determining adlayer parameters is based on the calculation of Δf_n and ΔD_n from known initial parameter values (d_A^0, η_A^0, μ_A^0) first. The calculated Δf_n^c and ΔD_n^c values are then compared to the measured Δf_n^m and ΔD_n^m at each overtone involved in the analysis. Using standard deviation values $std_{\Delta f_n^m}$ and $std_{\Delta Dnm}$ that characterize the measured Δf_n^m and ΔD_n^m, a χ^2 error function can be computed as follows:

$$\chi^2 = \sum_{n=1}^{k}\left[\frac{\left(\Delta f_n^m - \Delta f_n^c\right)^2}{\left(std_{\Delta f_n^m}\right)^2} + \frac{\left(\Delta D_n^m - \Delta D_n^c\right)^2}{\left(std_{\Delta D_n^m}\right)^2}\right] \tag{10}$$

Until the computed χ^2 is not accepted (minimum is not reached) an iterated set of parameter values are chosen, and the above calculation method is repeated. If a χ^2 minimum is found, the decision of accepting the parameter values can be made by visually checking the fit or by assessing the value of χ^2. This fit method can be performed independently, point-by-point, at each measurement time resulting in a set of Δf_n^{fit} and ΔD_n^{fit} as well as d_A^{fit}, η_A^{fit}, μ_A^{fit} in time [105,107,108]. Once the parameters are calculated, the surface mass can be determined based on the resulted d_A and given ρ_A values:

$$M^V = d_A \rho_A \tag{11}$$

Unfortunately environmental noise (e.g., mechanical irregularities in peristaltic pumping) significantly interferes with the fundamental frequency and dissipation, thus they are usually not considered in the evaluation [103,109].

The standard Kelvin–Voigt model considers a complex shear modulus written as $G^* = G' + iG'' = \mu_A + i\omega\eta_A$, where the G' storage modulus characterizes the elasticity and the G'' loss modulus characterizes the viscous behavior of the material. The model assumes a frequency-independent G' and applies a simple linear frequency–dependence for G''. In reality, both G' and G'' depend on the frequency and the dependence is not likely to be linear. Nevertheless, some studies applied the standard Kelvin–Voigt model for characterizing various types of viscoelastic adlayers apparently successfully [103,104,107,110,111]. Some works invoked a linear frequency–dependence of both μ_A and η_A for improving the fit of the model to the data [108,112,113]. Other approaches for dealing with the different shapes of frequency–dependence use a power law for the expression of μ_A and η_A. A thoroughly detailed such a model has been applied by Johannsmann, using an equivalent circuit approach for the viscoelastic system description [95,96] (a software called *QTM* applying this model is available to download [114]). Another model involving power-law analysis is connected to the group of Shull [115,116] and has been applied in some recent studies [116–119]. The current version of the *Dfind* software (Biolin Scientific AB) also allows for the use of an extended Kelvin–Voigt model involving power-law frequency dependence [120]. An excellent guide to choosing the proper analysis method was published by Reviakine and co-workers [99]. Other data analysis methods considering various model cases (e.g., fully elastic, fully viscous and viscoelastic adlayer; thin and thick films) can be found [120–122].

Another great QCM data analysis guide is the paper of McNamara et al. [303]. In this study, the authors outline a quantitative method that can be used to select a special combination of f and D harmonics (e.g., ΔD_3, Δf_5, Δf_{13}) which should be included in the analysis to get reliable values representing the true parameters of the underlying system. The method relies on the Kelvin-Voigt model to calculate Δf_n and ΔD_n. A full package of MATLAB code that runs the sensitivity-based evaluation is also available to the paper (fit of experimental data is not included). Interestingly, according to the authors' report, it is possible that the best results can be found from fitting Δf harmonics only.

QCM has been extensively used for revealing the properties of soft biomaterials. The application of QCM in combination with optical techniques to characterize hydrated thin layers is further detailed in Section 5. Also, in a number of studies QCM was applied for extracting quantitative kinetic information in order to investigate, e.g. the dynamics of IgG oligomer formation [123], DNA hybridization [124], the interaction of proteins with cell surface carbohydrates [125], polydopamine-coated surfaces [126] as well as biopharmaceuticals with Protein A-modified surfaces [127]. The QSense Pro QCM-D instrument (Biolin Scientific AB) provides simultaneous measurement of eight independent sensors with a maximum mass and dissipation sensitivity of ~0.5 ng cm^{-2} and ~0.04 × 10^{-6}, respectively [128].

2.2. Novel label-free optical biosensor techniques in kinetic measurements

In addition to the OWLS technique, recently introduced waveguide-based instruments such as the resonant waveguide grating (RWG) and grating-coupled interferometry (GCI) biosensors have shown the potentials of the measurement principle in terms of high throughput and achieving even higher sensitivities [20,129,130]. The measurement principles of five novel optical techniques are visualized in Fig. 2. An important limitation of these techniques is, however, that water, trapped in the analyte layer, cannot be detected, because they monitor RI
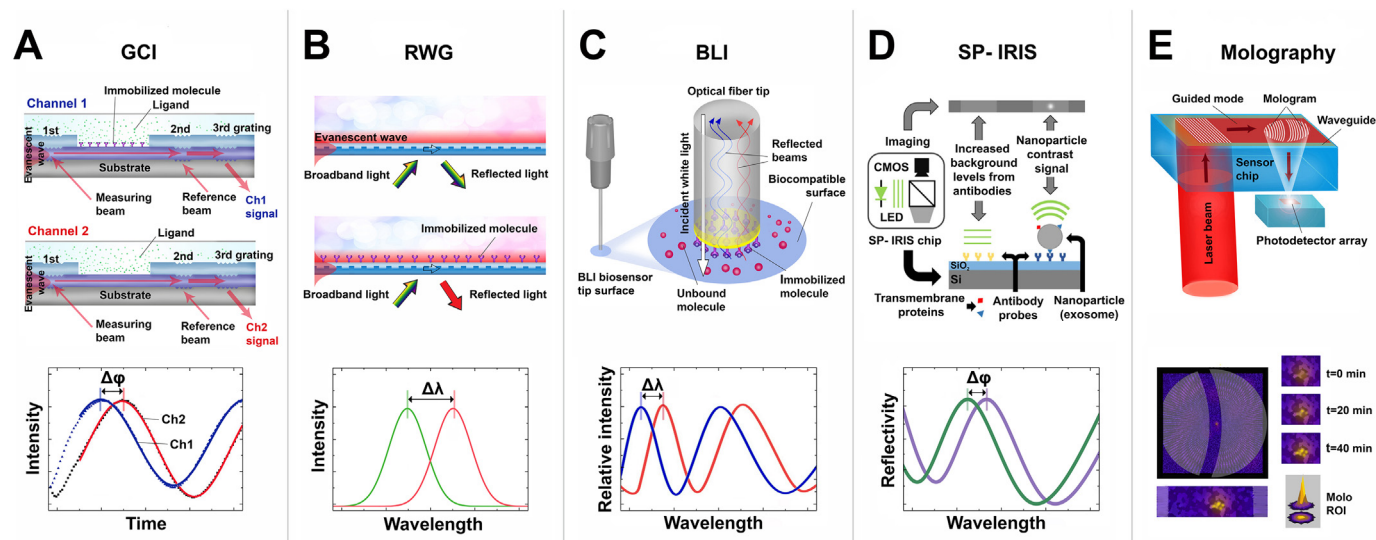
Fig. 2. Measuring principles of cutting-edge label-free optical biosensor technologies. Schemes on the top and graphs on the bottom represent the measurement setup and raw measurement data of the corresponding technique. The diagrams and graphs are adapted from the below listed references. [Adapted (A) from Ref. [132], copyright 2020 Royal Society of Chemistry; (C) copyright Sartorius AG; (D) from Ref. [133], copyright 2017 Springer Nature; (D) from Ref. [176], copyright 2016 Springer Nature used under CC BY; (E) from Ref. [134], copyright 2019 American Physical Society]

contrast relative to the aqueous background. This fact means that only the "dry" mass of analyte molecules can be effectively determined [67,131].

2.2.1. Grating coupled interferometry (GCI)

The highest sensitivity among label-free biosensors is provided by techniques exploiting interference–based detection methods [20,135]. GCI is one of the most successful realization of these methods, that has just recently started to demonstrate its capabilities in kinetic studies.

The main difference between an OWLS and GCI setup is that GCI couples a second laser beam into the waveguide layer in which the two beams interfere with each other and the characteristics of this interference is monitored. Fig. 2 A presents the arrangement of a GCI setup. A GCI chip can incorporate multiple fluidically separated channels (i.e., flow cells); two such channels can be seen in the figure. This is a very useful feature to facilitate the simultaneous acquisition of kinetic curves corresponding to slightly different conditions [136]. The sensor chip has three separate diffraction gratings embedded in the waveguide film, made from Ta_2O_5. The waveguide sits on a glass substrate and the top of the waveguide is coated by a SiO_2 film, which covers the entire waveguide except the area used for sensing. A laser beam — called the measuring beam — is coupled into the waveguide film through the 1st grating. A guided mode is launched and in the region of the sensing window its evanescent field is in contact with the sample solution. The role of the 2nd grating is to couple the reference beam into the waveguide film. The measuring and reference beams interfere with each other inside the waveguide and the combined beam carries the interference characteristics. The SiO_2 film is used to prevent the evanescent field of the combined beam from penetrating into the medium and undergoing a phase shift caused by RI changes in the medium. The 3rd grating serves as an outcoupler of the combined beam, which is directed towards a photodetector. In contrast to DPI, where the interference pattern is spatially analyzed, GCI monitors the phase shift as a function of time. This detection method is realized by a time-varying phase modulation provided by a liquid crystal modulator (LCM) positioned in the path of the reference light before incoupling. The phase modulation of the reference beam translates the phase information of interference into a time-varying intensity change (see Fig. 2 A, bottom graph). Any RI changes in the evanescent field lead to a phase shift in the guided wave resulting in a change of the time-dependent signal characteristics.

The $\Delta\varphi$ phase shift is determined by fitting the measured curves at each measurement time and calculated as a difference from the baseline: $\Delta\varphi = \varphi(t) - \varphi(t_0)$. $\Delta\varphi$ is proportional to change in the RI [20,137,138]. A great benefit of the method is that multiple channels can be integrated on the same chip and at least one channel can be used as a reference channel.

The first GCI instrument, WAVE, was launched by Creoptix AG [139] (Wädenswil, Switzerland) and has shown its potential in the field of BIA even during its short presence in the market. Owing to a noise level < 0.01 pg mm^{-2}, the technique offers the measurement of surface mass below 1 pg mm^{-2}, making the WAVE perhaps the most sensitive label-free biosensor [20]. The sensitivity allows for binding kinetic measuerements of analytes with a molecular weight (MW) below 100 Da. Millisecond time resolution together with a fast-flowing fluidic system is designed to resolve very fast binding kinetics characterized by high on- and off-rates (up to $k_a \approx 3 \times 10^9$ M^{-1} s^{-1} and $k_d \approx 10$ s^{-1}). Owing to this performance and high-throughput capability (a 4–channel sensor, able to handle a 2×384–well plate), the technique is especially suitable for fragment–based screening in drug discovery. The operation and data analysis software *WAVEcontrol* includes a versatile kinetic analysis functionality. GCI has found a broad range of applications in plant biology [140–147], cancer research [148], drug discovery [149] as well as the characterization of natural active agent–protein interactions [132]. As recently presented, the top sensitivity of GCI allows for acquiring reliable kinetics of MW <100 Da analytes, making possible to reveal the interaction of Ni(II) ions (52 Da) with Ni-specific protein molecules [50].

2.2.2. Resonant waveguide grating (RWG) biosensor

Similar to OWLS and GCI, resonant waveguide grating (RWG) biosensors also use a diffraction grating embedded in a waveguide film to couple light into a waveguide. In the case of RWG the same grating is used for outcoupling the guided EM wave, practically meaning that the grating together with the waveguide serves as a resonant mirror (see Fig. 2 B). The criterion of constructive interference is only satisfied at a specific illuminating wavelength, called the resonant wavelength (λ_R). Any RI changes within the penetration depth of the evanescent field (ca. 150 nm) detunes the resonance and thus the waveguide modes can no longer be excited by the illuminating light with wavelength λ_R. Waveguiding can be resumed at another resonant

wavelength ($\lambda_R' \neq \lambda_R$). The shift in resonant wavelength ($\Delta\lambda = \lambda_R' - \lambda_R$, see the difference between resonance peaks in Fig. 2 B) is proportional to variations of N occurring in the waveguide-coating-medium system. An advantage of the RWG method is that light beams at a nominally normal incident angle can be applied to illuminate the biosensor [21,150]. This is significant for sampling large number of biosensor elements simultaneously, which is necessary for HTS [21]. Measuring samples in a typical high-throughput system often directly takes place in microplates [21].

A widely used RWG biosensor is the Epic benchtop (BT) system from Corning Inc. [151] (Corning, NY, USA). A typical commercial Epic microplate consists of a glass substrate, a waveguide film (made of the biocompatible Nb_2O_5 material) with the embedded grating structure as well as a biofunctional coating [152]. The Epic instrument monitors $\Delta\lambda$ by sweeping the wavelength of broadband illuminating light over a 15 nm wide wavelength range with a 0.25 pm precision and records the resonant wavelength with a CCD detector. The Epic has a LOD of 2.2×10^{-6} RIU (refractive index unit), which corresponds to 0.078 ng cm^{-2} in surface mass [129]. The great benefit of the technique is that the sensors are realized in the standard microplate format, where each well of a 96– or 384–well plate contains an independent sensor element in the center position, and all can be simultaneously interrogated. Moreover, $\Delta\lambda$ of each well is measured in real-time with a resolution of 3 s, allowing the user to collect high-resolution kinetic data over long time intervals. The detection method and microplate–based construction make the Epic system an powerful technique for performing high-throughput label-free biochemical and cellular assays in real-time [21,153–155]. The Epic BT is provided with a controller and data collection software (*LFAassay*) which, however, does not include tools for kinetic analysis to the date of this article.

RWG technology has found a number of applications especially in cell biology and cell–based measurements for drug discovery. Recently, the technology was successfully applied to monitor the kinetics of cell adhesion [156–158] cell–surface and cell membrane receptor–ligand interactions [17,130], binding affinity [159], cytotoxicity [24], cellular signaling [160,161], and the functional state of surface-bound cells down to the single cell level [162]. Natural products were examined with this method as well on different cell lines [163], like hazardous herbs [164], and the popular green tea polyphenol epigallocatechin gallate (EGCG) [165,166]. Nanoparticle penetration into cells could also be monitored [167]. Experiments with extracellular vesicles (EVs) [168] and an endothelial label-free biochip (EnLaB) assay [169] have been reported recently. Using a calibration methodology with robotic fluidic force microscopy (FluidFM), cell adhesion force kinetics of single cell populations have been monitored [162]. Clearly many diverse biological and biophysical process and phenomena can be examined thanks to the sensitivity and high-throughput capability of RWG biosensor.

2.2.3. Bio-layer interferometry (BLI)

Bio-layer interferometry (BLI) is an optical label-free technique for measuring biomolecular interactions (see Fig. 2 C). The technique analyzes the interference pattern of white light that is guided in an optical fiber and reflected from two interfaces: an internal reference layer and a layer of immobilized protein on a sensing tip. 384 Binding of an analyte in solution to the immobilized ligand on the biosensor tip surface increases the optical thickness at the tip and causes a shift in the interference pattern. This results in a wavelength shift ($\Delta\lambda$), which is a direct measure of the alteration in thickness of the biological adlayer. Only molecules binding to or dissociating from the tip surface can change the interference pattern creating a response profile that can be monitored in real time. Unbound molecules, changes in the flow rate or in the RI of the medium have no significant effect on the interference pattern. This relative insensitivity to the medium extends the technique's capability to monitor crude samples without prepurification [171]. BLI has already been applied in vaccine research, for instance in clinical studies, epitope design, pathogen diversity and distribution studies,

nucleic acid and molecular pathogen–host interaction studies as well as host immune response characterization [170,172].

The BLI technology is commercially available as the FortéBio Octet system (Sartorius AG, Göttingen, Germany), offering a sensitive analytical tool for measuring affinity and kinetics with a dynamic range of >150 Da, affinities in the range of 10 pM – 1 mM as well as association and dissociation rates in the range of $k_a = 10^1–10^7$ M^{-1} s^{-1} and $k_d = 10^{-6}–10^{-1}$ s^{-1}, respectively [171]. With this technique, fast results can be obtained; for instance, in the study of Mechaly et al., measurement was carried out with a LOD of 10 pg mL^{-1} for ricin and 1×10^4 pfu mL^{-1} for *F. tularensis* within 17 min [173]. The FortéBio provides BLI instruments from 2–channel (Octet K2, up to 2 assays in parallel) to high-throughput ones working with 384–well tilted-bottom microplates and 96–well microplates (Octet HTX and Octet RED384) [171].

2.2.4. Interferometric reflectance imaging sensor (IRIS)

A simple reflectance–based interferometric detection method has been devised by Özkumur and co-workers [174]. As an optical label-free method, IRIS owns all the advantageous points of those methods with an additional improvement for multiplexed measurements. The solid support of arrayed biomolecules is a silicon chip that has a thick uniform oxide layer on top. In its original form a tunable laser is incident on the array and reflection spectra are recorded from hundreds of spots simultaneously. The detection principle is that in case of a layered substrate, if light reflects from the substrate layer interfaces (Si–SiO$_2$ and SiO$_2$–air interface), characteristic spectral reflectance appears. Added mass on the SiO$_2$ surface changes the optical path length difference generating a shift in the detected wavelength-dependent reflectivity curve. The next generation of the IRIS platform employs multiple discrete LED sources making this technology more accessible, while it can achieve similar performance [175].

More recently, single particle interferometric reflectance imaging sensor (SP-IRIS) technology was developed where an enhanced contrast in the scattering signal from nanoparticles enabled multiplexed detection of viruses in serum or whole blood. The SP-IRIS method was able to count the number of particles, estimate particle size, and phenotype exosomes from purified samples from cell culture, or directly from clinical sample, down to a sample volume of 20 μL [176]. Tested with dynamic monitoring of antigen–antibody binding, a noise floor of 5.2 pg mm^{-2} was demonstrated.

On the market, the SP-IRIS technology has been realized as the ExoView R100 instrument of NanoView Biosciences (Brighton, MA, USA) targeting complex EV characterization [177]. The system applies the label-free SP-IRIS method together with fluorescent detection to analyze EVs at the single particle level. SP-IRIS is used to measure the size distribution of EVs with counting and determining single EV size of as low as 50 nm. One chip accepts 35 uL of sample solution. Fluorescent detection is used to identify EV membrane proteins and other biomarkers.

2.2.5. Focal molography

Focal molography is the newest among the biosensor techniques reviewd in this paper. It is still under intensive development in a collaboration of Roche Diagnostics and ETH Zürich and has not been launched as a commercial instrument. It is worth presenting as a next-generation label-free optical biosensor that may open up new perspectives for kinetic measurements. The theoretical background of focal molography and application as a BIA technology was first described by Fattinger in 2014 [178].

In focal molography (a neologism coined from "focal molecular holography"), detection is based on probing the *mologram* by laser light coupled into a monomode waveguide film that constitutes the sensor chip. The mologram is defined as a synthetic hologram, which is a precise nanopatterned assembly of receptor molecules. It is fabricated on a graft-copolymer layer attached to the waveguide film, where a submicrometer array of ridges (lines carrying the active sites) and

inactive grooves are formed by a photolithographic process. The special arrangement of receptors is designed to diffract the probing coherent laser light and focus it into a diffraction–limited focal spot. The spot is captured by a photodetector array where the molographic signal is recorded as the total light intensity of the focal spot.

The unprecedented advantage of focal molography is that it can intrinsically discriminate specific binding from NSB, which otherwise always degrades biosensing signals [179]. This is realized by the special coherent assembly of the mologram, where the ridges and grooves are in effect the measuring and reference regions. As such, comprising hundreds of such separate regions, the technique can collect reference-corrected signal originating from a large number of tiny measuring and reference regions. Moreover, scattering by non-specifically bound molecules that are randomly distributed in the copolymer layer do not contribute to the coherent signal [133,134]. NSB makes measurements in complex bodily fluids difficult by obscuring the signal of specific binding [179,180]; hence focal molography is expected to be a breakthrough in the selective detection of specific biomolecular interactions [181].

Based on measurements performed on a therapeutic antibody diluted in human plasma sample, the LOD was determined to be 200 ng mL^{-1} (1.3 nM). As an assay-independent measure, the upper limit bound of LOD expressed in surface load was found to be ~5 pg mm^{-2}. It is expected that further optimization in the lithography and readout method would improve the LOD by at least two orders of magnitude [133]. As recently demonstrated, the technique can also be applied in highly specific cell–based assays [182]. Due to the potential for multiplexing (several molograms on one single chip) and miniaturization, focal molography may be a future technology for point-of-care diagnostics [133,183].

3. Modeling adsorption kinetics

To quantitatively interpret experimental adsorption kinetic data, a kinetic model is needed that represents the adsorption mechanism and involves parameters that biophysicochemically characterize the system. When considering biomolecular interactions, the interaction of molecules with surfaces can be considered as specific or non-specific. In the case of specific binding the surface is usually assumed to be an array of distinct and independent binding sites, which strictly determine the positions where analytes can bind. In contrast, non-specific binding defines the surface as a continuum everywhere potentially available for adsorbing species, at least initially as an empty surface; randomly adsorbed species create exclusion zones even for non-specific binding [184,185]. Hence, classification of a binding surface as a continuous or distinct array is somewhat arbitrary as it depends upon the size of the adsorbing ligand relative to the size of the binding sites constituting the adsorbent surface, with their arrangement also playing a role [37,184]. In many natural adsorption processes, the surface unambiguously presents a continuum to the adsorbing species, not an ordered array of independent, non-overlapping sites larger than the adsorbing ligand as assumed in the Langmuir model, and the sequential addition of molecules at randomly chosen positions engenders gaps between the adsorbed molecules which cannot later be filled. Similar reasoning applies to molecules adsorbing at randomly distributed discrete sites [186].

The most relevant field for the kinetic analysis of specific interactions is drug discovery, whereas non-specific adsorption kinetics find major interest in biosensor technologies, membrane and implant development, and maritime industries, where developing antifouling coatings has crucial importance. In such field not only the structures but also the kinetics may be complex, and the models devised to interpret the measured kinetics must appropriately match this complexity. It is important to recognize that many of the processes, including association, dissociation and many types of macromolecular conformational changes may operate on very different timescales, a proper understanding of which is essential for arriving at meaningful conclusions

[184,187]. A practical summary of parameters that should be considered in the analysis of biomolecule adsorption data in terms of structure and kinetics was published by Migliorini et al. [188].

3.1. Fundamentals of adsorption kinetics. The Langmuir model

The Langmuir model can be considered as the fundamental theory of binding kinetics. It was devised for describing gas adsorption at discrete active sites on solid surfaces. A system may follow the Langmuir model if it fulfils specific restrictions as described elsewhere [189]. It is not prima facie obvious why a theory developed for ultraclean crystalline metal surfaces in high vacuum and at low temperature, in which every metal atom on the surface constitutes a binding site for a gas atom or small molecule, should be applicable to biomacromolecules adsorbing on a surface from solution, but for small antigens binding to immobilized antibodies it seems that the requisite conditions can be fulfilled.

Let us consider a solution of adsorptives in contact with a solid surface. Adsorptives or, more specifically, protein molecules or any particle P can adsorb onto binding sites S^* of the surface resulting in adsorbed particles A, that can be also interpreted as P–S^* complexes, highlighting the adsorbate-surface interactions. The adsorption and desorption process can be described by the following reversible reaction scheme:

$$P + S^* \underset{k_d}{\overset{k_a}{\rightleftharpoons}} A \tag{12}$$

The rates of the forward (adsorption/association) and backward (desorption/dissociation) reactions are characterized by rate constants k_a and k_d, respectively. Considering that only monolayer formation is permitted (which is realistic for several proteins, e.g. bovine serum albumin, BSA) and the maximal coverage is defined by the surface density of the layer resulting from complete occupation of sites S^*, the fractional coverage (Θ) can be expressed as:

$$\Theta = \frac{M}{M_{max}} = \frac{M}{m/a} = \nu a \tag{13}$$

where ν and M are the number per unit area and mass per unit area (also referred as surface mass or simply mass) of the adsorbed molecules, respectively. M_{max} is the surface mass density that corresponds to the theoretically achievable maximal coverage (100% occupancy), a is the area occupied by one adsorbate bound to the binding site and m is the mass of one adsorbing species. The surface concentration of the available binding sites can be defined as the fraction of available sites (Φ), which is inversely related to Θ.

Based on the law of mass action, the net rate equation of the adsorption process written in terms of the time derivative of ν is:

$$\frac{d\nu}{dt} = k_{a,num} c_{B,num} (\nu_{max} - \nu) - k_d \nu \tag{14}$$

where $k_{a,num}$ is the adsorption/association rate constant, $c_{B,num}$ is the bulk concentration of species per unit volume (both quantities are set to the number of adsorbing species) and $\nu_{max} = 1/a$ is the maximal number of analytes per unit area that can be bound to the surface representing complete occupancy. ν_{max} is therefore the total number of binding sites per unit area. We can use mass M instead of ν if we multiply by m, obtaining:

$$\frac{dM}{dt} = k_{a,mass} c_{B,mass} (1 - \Theta) - k_d M \tag{15}$$

Note, that we introduced here the kinetic rate parameter $k_{a,mass} = k_{a,num}/a$ which will be later referred to as k_a with typical units of cm s^{-1}. Also, $c_{B,mass} = m c_{B,num}$ will be further simply used as c_B The Langmuir model assumes the simplest case when all the binding sites that are not occupied by adsorbates are available for adsorption and a "monolayer" coverage ($\Phi = 0$) can be reached:
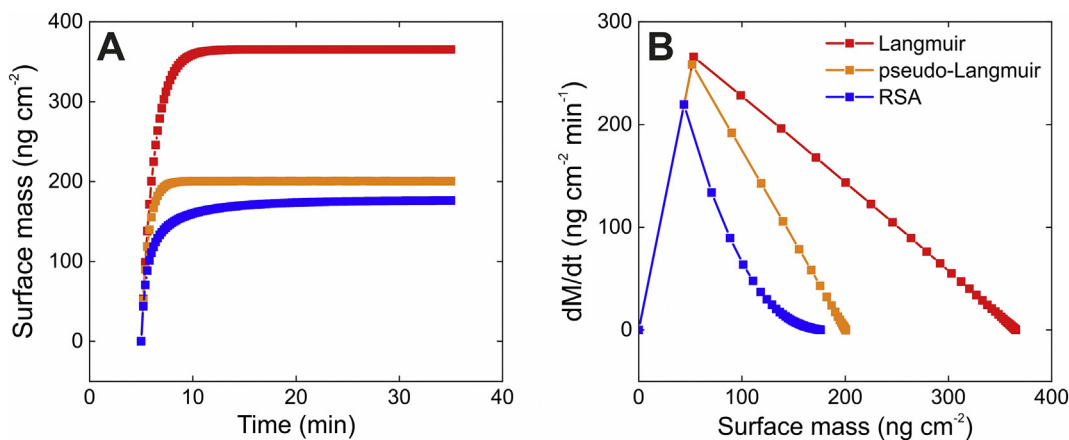
Fig. 3. Characteristics of the Langmuir model compared to random sequential adsorption (RSA). The curves are based on simulated data. Graph A shows simulated curves that demonstrate what we can obtain from a typical biosensor measurement. Graph B presents processed data where the mass derivative dM/dt was calculated and plotted against the surface mass M. The so-called pseudo-Langmuir data were simulated using the same conditions as for Langmuir ($\Phi = 1 - \Theta$), except that instead of allowing 100% coverage, a jamming limit of $\Theta_j = 0.547$ was set (see details in Section 3.3). Although the pseudo-Langmuir data are closer to the RSA, the shape of the curve is clearly different. Model conditions in simulations (symbols of hydrodynamic conditions are detailed in Section 3.5): $k_a = 5.0 \times 10^6$ cm s^{-1}, $k_d = 1.0 \times 10^4$ s^{-1}, $a = 30$ nm^2; MW = 66.5 kDa, D = 8.1 $\times$ 10 7 cm2 s 1, $c_B = 1000$ µg mL-1, Q = 1 µL s-1, dcS/dt = 0, flow cell: OWLS SH 0812-08, δD = 77.6 µm; Langmuir: $\Phi = 1 - \Theta$, $\Theta_j = 1$; pseudo-Langmuir: $\Phi = 1 - \Theta$, $\Theta_j = 0.547$; RSA: Φ calculated according to Eq. (22), $\Theta_j = 0.547$ (spherical object).

$$\Phi = 1 - \Theta \tag{16}$$

One simple way is for checking whether the observed adsorption/binding process follows the Langmuir equation is plotting the measured $M(t)$ data as dM/dt vs. M curve (see red line in Fig. 3B). In case of a Langmuir-type adsorption, the measured points should fall on a straight line determined by Eq. (15) [186]. (See Fig. 4.)

In affinity kinetic analysis, and thus in the vast majority of reported SPR measurements, the measured response R ("resonance units", with unit of RU) is assumed — unfortunately not always correctly — to be directly proportional to the number of bound analytes (i.e., $R \propto \nu$), and the following formula is widely used [190]:

$$\frac{dR}{dt} = k_{a,resp} c_{B,num} (R_{max} - R) - k_d R \tag{17}$$

which is essentially the same as Eqs. (14) or (15). Here, R_{max} is the maximal response (proportional to the amount of S^* binding sites) and the typical units of $k_{a,resp}$ is M^{-1} s^{-1} (to get this, Eq. (14) is multiplied by the Avogadro number $N_{Av} = 6 \times 10^{23}$ mol^{-1}). To be able to compare

k_a values obtained from Eq. (15) and Eq. (17) ($k_{a,mass}$ and $k_{a,resp}$) one can use the practical formula:

$$k_{a,resp} = 10^{-17} k_{a,mass} N_{Av} a = 6 \times 10^6 k_{a,mass} a \tag{18}$$

where $k_{a,resp}$, $k_{a,mass}$ and a are given in their widely used M^{-1} s^{-1}, cm s^{-1} and nm^2 units, respectively. Using this conversion, one can see that the value of k_a strongly depends on the mode of interaction. For example, in the case of the non-specific adsorption (NSB) of BSA from HEPES buffer onto silica [191], $k_{a,mass} = 1.1 \times 10^{-6}$ cm s^{-1} which is equivalent to $k_{a,resp} = 1.9 \times 10^2$ M^{-1} s^{-1} ($a = 29$ nm^2). As expected, this value is much below the $k_{a,resp}$ values characteristic to specific receptor-analyte interactions, and besides, non-specific adsorption would not be expected to fulfil the Langmuir criteria. Typical value of kinetic rate constants characterizing the adsorption of proteins are in the range of $k_{a,mass} = 10^{-6}$–10^{-4} cm s^{-1} [192] and for desorption $k_d \approx 10^{-4}$ s^{-1} [186]. For the adsorption of microbial cells, a value of $k_{a,mass} \approx 10^{-5}$ cm s^{-1} seems to be typical [192]. Assuming a full "monolayer" coverage ($\Theta = 1$) at saturation, the effective surface area occupied by a
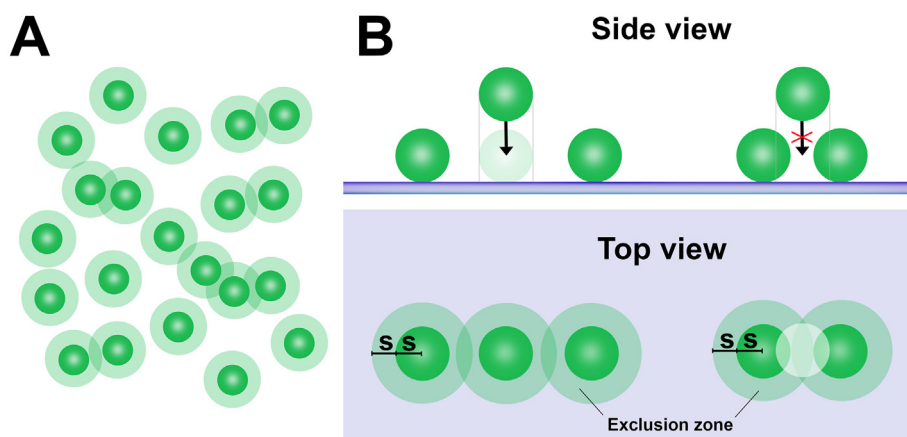
Fig. 4. Arrangement rules according to the RSA model. The "footprint" of one spherical object (green circle) with radius s is $a = s^2\pi$. Each sphere has an exclusion zone (light green halo around spheres) and thus the total occupied area of one sphere is $4s^2\pi$. While overlapping of exclusion zones is permitted, the distance between the center positions of two spheres cannot be smaller than $2s$. Besides the top view of a larger number of adsorbed spheres (A), three separate spheres both with side and top views are also shown providing a clear example of the RSA rules (B). [Adapted from Ref. [187], copyright Marcel Dekker Inc.; from Ref. [212] copyright American Physical Society]. Model conditions in simulations (symbols of hydrodynamic conditions are detailed in Section 3.5): $k_a = 5.0 \times 10^{-6}$ cm s^{-1}, $k_d = 1.0 \times 10^{-4}$ s^{-1}, $a = 30$ nm^2; MW = 66.5 kDa, D = 8.1 $\times$ 10^{-7} cm^2 s^{-1}, $c_B = 1000$ µg mL^{-1}, Q = 1 µL s^{-1}, dcS/dt = 0, flow cell: OWLS SH-0812–08, $\delta_D = 77.6$ µm; Langmuir: $\Phi = 1 - \Theta$, $\Theta_j = 1$; pseudo-Langmuir: $\Phi = 1 - \Theta$, $\Theta_j = 0.547$; RSA: Φ calculated according to Eq. (22), $\Theta_j = 0.547$ (spherical object).

single receptor molecule can be calculated from the measured M_{max} and the known m using Eq. (13).

Despite its restricting assumptions, which are seldom justified in biology, the Langmuir model is still widely used for kinetic analysis of specific interactions, perhaps because of its simplicity. It is offered to the user as the first approach in data evaluation, e.g. both the Biacore and Creoptix WAVE analysis softare packages apply the Langmuir model, calling it "1:1 kinetics". However, the model usually fails to describe non-specific adsorption kinetics, such as the adsorption of protein molecules on sensor surfaces. The two main deviations from the Langmuir model are (i) the sensor surface (a metal or dielectric film) must be considered as a continuum, not an array of individual binding sites — which even if they existed would be far smaller than the analyte — and (ii) adsorbates can reside on the surface for several days or longer ($k_d < 10^{-6}$ s^{-1} instead of the $\approx 10^{-4}$ s^{-1} typical of ligand–receptor dissociation in homogeneous solution [186]), meaning that the adsorption was practically irreversible, contradicting Eq. (12). Extended versions of the Langmuir theory have been discussed [193], but they cannot satisfactorily overcome its fundamental limitations. The only reported cases where the Langmuir model was found to be applicable to analytes binding to a continuum is where the ligands are mobile on the surface and can form clusters [194,195]. These results were obtained with sensor chips coated with a lipid bilayer. In such cases a in Eq. (13) is the area occupied per analyte molecule and true monolayer coverage is achievable. Obviously to have clustering there must be interaction between the adsorbed species, hence the "no interactions" restriction of the Langmuir model is flouted, yet nevertheless the model is successful.

3.2. Bivalent model

Whereas the Langmuir model restricts one adsorbing species or analyte to bind at one surface binding site only, the bivalent model allows the bivalent analyte, that is equipped with two binding sites (e.g., an antibody), to bind first to one surface site and then consecutively to a second one (forming A_1 and A_2 complexes, respectively) [179,190,196]. The model has been extensively used to study antibody affinity profile [197] and cell signaling [198]. Model scheme and rate equations written in terms of R response units are as follows:

$$P + S^* \underset{k_{d2}}{\overset{k_{a1}}{\rightleftharpoons}} A_1 \; ; \; A_1 + S^* \underset{k_{d2}}{\overset{k_{a2}}{\rightleftharpoons}} A_2 \tag{19}$$
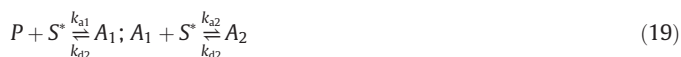
$$\frac{dR_{A1}}{dt} = [k_{a1,resp} c_{B,num}(R_{max} - R_{A1} - R_{A2}) - k_{d1} R_{A1}] \tag{20a}$$
$$- [k_{a2,resp} R_{A1}(R_{max} - R_{A1} - R_{A2}) - k_{d2} R_{A2}]$$

$$\frac{dR_{A2}}{dt} = [k_{a2,resp} R_{A1}(R_{max} - R_{A1} - R_{A2}) - k_{d2} R_{A2}] \tag{20b}$$

where the total response $R_{total} = R_{A1} + R_{A2}$ and $R_{A1} = R_{A2} = 0$ at $t = 0$. The two-step binding kinetics is characterized by rate constants k_{a1}, k_{a2}, k_{d1}, k_{d2} (or their response–based versions as seen in the given equations).

3.3. The RSA model

Deviations from the Langmuir adsorption model are well known and discussed in textbooks [187,199]. Even if there is no affinity between adsorbed species, they cannot occupy each other's space and in this sense they do interact. Theoretically this short-range interaction can be taken into account by the pair interaction energy (potential). The deposition of proteins on the surface results in gaps between the adsorbed molecules small enough to exclude subsequent arrivals. The random sequential adsorption (RSA) model takes this into account along with other important features, namely that rigid particles are deposited on

the surface at random positions selected sequentially, and that adsorption (deposition) is irreversible [200,201]. Experiments [202] verified the major predictions [200,201] of the RSA model: a short- and intermediate-time kinetics markedly different from that of the Langmuir model and a slow asymptotic approach to saturation. The original RSA model has been extended to take into account desorption and protein relaxation on the surface [203–209]. The astonishing success of the very simple basic RSA model was later shown to reside in the fact that the hydrodynamic friction experienced by particles as they approach the adsorbing surface perpendicular to it randomizes the motion such that it compensates for the highly spatially correlated redeposition attempts of a particle that has been rejected due to the prior presence of deposited particles [210,211].

In kinetic equations, RSA yields a Φ whose value is always below the Langmuir $1 - \Theta$. The describing Θ–dependence of Φ has been approximated theoretically and confirmed by systematic numerical simulations for objects with varying geometrical shapes [201,213–215]. The RSA model satisfactorily accounts for the observation that the plateau of adsorption (the "jamming limit", Θ_j) of a protein onto a continuum is typically less than half the value expected for a packed monolayer. The coverage can be thus redefined as:

$$\Theta = \frac{M}{\Theta_j m/a} \tag{21}$$

In the case of adsorbing disks, $\Theta_j \approx 55\%$. The physical meaning of Θ_j is that although there is still plenty of unoccupied space, there is no free surface large enough to accommodate an additional adsorbate. Schaaf and Talbot found that for spherical adsorbates (subtending disks) the available surface function is [201]:

$$\Phi = (1-\Theta)^3 / \left(1 - 0.812 \cdot \Theta - 0.2336 \cdot \Theta^2 + 0.0845 \cdot \Theta^3\right) \tag{22}$$

where the jamming limit is $\Theta_j = 0.547$. For typical spherocylindrical objects [213,214]:

$$\Phi = (1-\Theta)^4 / \left(1 - 1.403 \cdot \Theta - 0.895 \cdot \Theta^2\right) \tag{23}$$

with a jamming limit $\Theta_j = 0.581$; a range of aspect ratios was investigated. Three-dimensional expansion of the RSA model for spheroidal particles has been established by Adamczyk and Weroński [215].

Characteristics of a system following the RSA model is demonstrated in Fig. 3, especially in graph B. As compared to the Langmuir model, a nonlinear end tail appears in the RSA dM/dt vs. M plot originating from the nonlinear Φ function. Such characteristic of an unknown system may suggest an RSA behavior. However, for note, this type of non-linearity can also originate from more complex kinetic models involving more adsorbate states on the surface (shown e.g., in Section 4), even without calculating Φ according to the RSA model.

The Langmuir model defines a as a virtually occupied area that can be much larger than the actual area of the adsorbate in contact with the surface if the binding sites are sparsely distributed. The RSA model however provides a quantity that describes the adsorbate–surface interaction with a physically greater relevance. In this case a appearing in Eq. (21) can be interpreted as the actual area of a single adsorbate interacting with the surface, also termed as molecular footprint.

3.4. Multiple molecular states on the surface

The simplest kinetic model assumes only one state on the surface. This is doubtless valid for isotropic spheres of a metal or a simple binary compound such as CdTe but is an unrealistic description of a complex protein. In many cases, the complexity is manifested as multiple orientational and conformational states in which the adsorbates can be present on the surface. A biopolymer can undergo conformational changes that significantly increase the number of interfacial interactions [216].

As the probability of breaking up these interactions simultaneously is also increased, the probability of desorption becomes almost vanishingly small ($k_d < 10^{-6}\,s^{-1}$) and the adsorption becomes practically irreversible [186]. In this case, a relatively simple approach is to separate the total surface adsorbed mass into reversibly and irreversibly adsorbed forms, viz. $M = M_r + M_i$. What makes the two states distinguishable on the surface is their different footprints a_r and a_i [207]. Eq. (21) is thus modified:

$$\Theta = \frac{1}{\Theta_j}\left(\frac{M_r}{m/a_r} + \frac{M_i}{m/a_i}\right) \tag{24}$$

Two-state RSA can encompass many variants, such as the adsorption of a single species that changes its conformation on the surface and a single species that can adsorb in two different orientations, and the kinetics of surface conformational change can be explicitly incorporated into the model [204–206,208]. If the data quality is good enough, as it should be from an SPR, OWLS or GCI measurement, the rate constants can all be determined by fitting [207].

3.5. Dealing with mass transport and hydrodynamics

The adsorption process requires sufficient analytes close to the surface; their presence is maintained by transport from the bulk solution. The zeroth approximation is to say that the concentration close to the surface is always equal to the bulk concentration (c_B); i.e., the analyte is uniformly distributed within the entire volume of the flow cell and all parts of the biosensor surface are exposed to the same constant analyte concentration (one may refer to this as the "well-mixed" approach but in reality mixing can never be that good due to the friction at the walls). In this case, one can set c_B as the concentration of analytes in the rate equation Eq. (15).

Stable hydrodynamic conditions can be best obtained by applying laminar flow in the flow chamber, e.g. by a peristaltic pump or, even better (to avoid rhythmic pulsations) a syringe pump. The laminar flow is characterized by a low Reynolds number Re (which is, however, dependent on the flow geometry and only gives a rough estimation of the flow regime). Nevertheless, laminar flow normally obtains for $Re < 2000$ for a long, straight cylindrical tube, and in practical biosensors it can be as low as 1–10. On the other hand, even values larger than 2000 can maintain laminar flow if disturbance that would drive it into turbulence is avoided. Due to the characteristic parabolic velocity profile of laminar flow in a cylindrical tube, the number of analytes is inevitably depleted close to the surface and the transport through this vicinal region may be crucial both in terms of biosensor measurement outcome and in the kinetic analysis of the data.

The presence of the depletion zone does not necessarily mean that transport is adsorption rate-limiting. If the rate of binding event is much slower than the transport, the kinetics are independent of transport and the flow cell can be treated as a well-mixed system. If the binding is fast, transport has a significant effect and can even dominate the kinetics [217,187,218]. This case is termed mass transport limited (MTL), recognition of which plays a crucial role in kinetic analysis and in the design of flow cells.

To fully treat mass transport, we must know the spatiotemporal concentration distribution in the flow cell, which can be achieved by solving the full convective–diffusive partial differential equation (PDE). Although this approach assures high accuracy in principle, the high computational demands of the numerical solution make it unsuitable for end-users trying to fit the model to their data [219]. Furthermore, errors introduced by discretization do not guarantee reliable results. With rational approximations, however, the problem can be made more tractable. In practice, dealing with transport means that we should only know the concentration in the close vicinity of the surface (c_S). What considerations enter the calculation of c_S? Starting with the mathematical description of the convective–diffusive system, we go through the derivation of the framework that is used to deal with transport in adsorption kinetic analysis.

3.5.1. The PDE model

The fundamentals of concentration variations in streaming solutions confined in a chamber whose solid wall is a site of heterogeneous chemical reaction were originally discussed in terms of electrochemical problems. The PDE describing this system is closely related to the Navier–Stokes equations, which should be taken into account for a full hydrodynamic treatment of the system. In the field of biosensors, the PDE model was first applied for total internal reflection (TIR) measurement analysis [220–222]; the equations were adapted for the Biacore SPR flow cell [223], and further developed by Christensen [224] and others [217,225]. Based on these studies (in particular following the formalism of Myszka and co-workers), we introduce the model conditions and governing equations as follows. Let us assume a flow chamber of rectangular cross-section (i.e., a channel) with length l, half-height h (full height $b = 2h$) and width w as shown in Fig. 5. The coordinates are given in the Cartesian system with x, y and z axes parallel to the sides l, w and h, respectively, where the origin is the inlet at the left bottom edge of the channel on the sensing surface (bottom plane). The solution enters with a flow direction parallel to x, linear flow velocity (flow rate) u_x and free analyte concentration c_B. We assume fully developed laminar flow along the entire length of the channel with its characteristic parabolic velocity profile on the vertical xz plane, described along the coordinate z by $u_x(z) = u_{max}(z/b)(1 - z/b)$. As such, the flow rate is
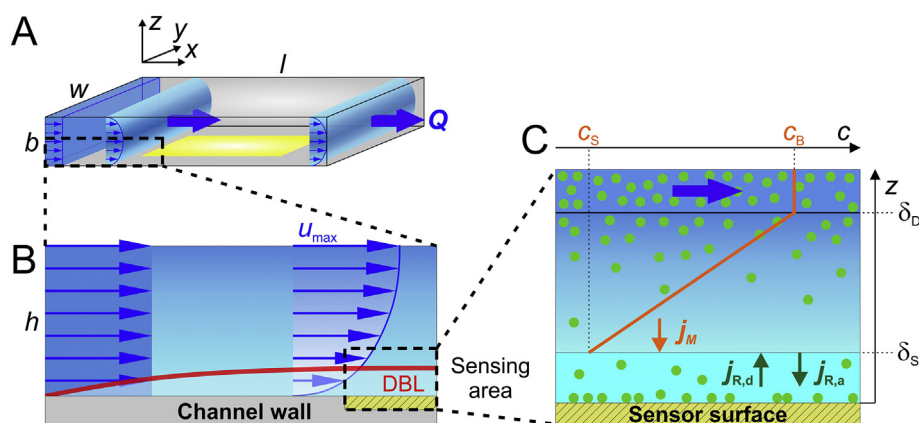
Fig. 5. A. Scheme of a flow channel in which the concentration variation is described by the standard PDE model. B–C. Two compartment model. Parabolic velocity distribution of a fluid with laminar flow. Concentration profile in the diffusion boundary layer.

zero at the bottom ($z = 0$) and top ($z = b$) channel boundaries and reaches its maximal value u_{max} in the center ($z = h$). Considering a mean velocity value of $u_{mean} = (2/3)u_{max}$ and cross-section area bw, the volumetric flow rate can be written as $Q = bw(2/3)u_{max}$. For most channels, $w >> h$, hence concentration variations in the y direction can be simply neglected.

The PDE model of this system has Eq. (25) as the governing equation with boundary conditions Eq. (26a) [217,225] and initial conditions Eq. (27a). The spatiotemporal free analyte concentration $c(t,x,z)$ is thus described by Eq. (25). According to the model, the mass transport of analyte to the sensor surface is determined only by diffusion and convective flow, where the y component of diffusion as well as y and z components of the flow velocity are neglected. Other driving forces relevant for mass transport such as the presence of a substrate electric field [226,227] may also be included in the model. While at the sensor surface boundary ($z = 0$) the transported analyte mass flux density (j_M) should be equal to the binding/adsorption rate (reaction flux density, j_R) (26a), at the top boundary it should be zero due to the unreactive and impenetrable channel wall (26b). Note, j_R is equal to the chosen cumulative equation for the mass derivative, e.g. Eq. (15). The concentration is constant with value of the injection concentration c_{inj} (26c) at the inlet boundary, and as a reasonable approximation the analyte leaves the cell at the outlet due to convective flow only (26d). The system's initial conditions are determined by the association (at $t = 0$) (27a) and dissociation (at $t = t_d$) (27b).

$$\frac{\partial c(t,x,z)}{\partial t} = D\left(\frac{\partial^2 c(t,x,z)}{\partial x^2} + \frac{\partial^2 c(t,x,z)}{\partial z^2}\right) - u_x(z)\frac{\partial c(t,x,z)}{\partial x} \quad (25)$$

at $z = 0$ $D\frac{\partial c(t,x,z)}{\partial z} = k_a c(t,x,0)\phi(t,x) - k_d M(t,x)$ $\quad (26a)$

at $z = b$ $D\frac{\partial c(t,x,z)}{\partial z} = 0$ $\quad (26b)$

at $x = 0$ $\frac{\partial c(t,x,z)}{\partial x} = 0, c(t,0,z) = c_{inj}$ $\quad (26c)$

at $x = l$ $\frac{\partial c(t,x,z)}{\partial x} = 0$ $\quad (26d)$

at $t = 0$ $c(0,x,z) = 0$ $\quad c_{inj} = c_B$ $\quad M = 0$ $\quad (27a)$

at $t = t_d$ $c(t_d,x,z) = c_{t_d}$ $\quad c_{inj} = 0$ $\quad M = M_{t_d}$ $\quad (27b)$

The PDE model can be solved only numerically. Numerical solutions of similar systems are extensively detailed in the literature, starting with the solution of equivalent electrochemical problems [228,229]. In the field of biosensing, the related papers cover mostly numerical simulations (using both finite difference (e.g., the Crank–Nicholson scheme) [220,224] or finite element methods [26,217,225,230–236]) adapted to the Biacore SPR flow chamber with specific receptor–ligand binding according to simple Langmuir kinetics, which might be appropriate for receptors immobilized in a dextran hydrogel, but then the hydrodynamic profiles will be more complicated than those shown in Fig. 8. To the best of our knowledge, a numerical solution of the PDE model involving RSA–based kinetics at a planar surface of receptors for which Fig. 8 is applicable has not been published. Vijayendran and co-workers showed that certain assumptions (e.g., neglecting convection but considering the diffusion equation for relevant dimensions) can make the PDE model more computationally tractable [237]. The full numerical solution is primarily used for simulations and, by retaining the complexity of the actual system, it can serve as an absolute standard for testing the validity of simpler models [219]. Simplified versions of the PDE model (e.g., the two-compartment model) became widespread because analytical solutions to the equations for the proper convective–diffusive

system are accessible through the steady-state approximation. Constantly increasing computational power may, however, soon enable the full set of equations to be numerically solved and simultaneously fitted to the data.

3.5.2. Two-compartment model

The two-compartment model is based on the analysis of the relative contribution of convection and diffusion to analyte transport. Far from the surface, well within the solution body, the concentration is maintained by convection at around c_B. Although in most of the volume of the channel transport is governed by convection, its contribution to analyte transport vanishes in the close vicinity of the surface (Fig. 8), causing significant depletion in analyte concentration, and molecular diffusion dominates transport. The relationship between convective and diffusive transport can be characterized by a dimensionless ratio called the Péclet number (Pe). Defined in direction x and taking l and h as characteristic channel distances, Pe is:

$$Pe = \frac{convection\ rate}{diffusion\ rate} = \frac{u_x(z)\left|\frac{\partial c}{\partial x}\right|}{D\left|\frac{\partial^2 c}{\partial x^2}\right|} = \frac{ul}{Dh^2} \quad (28)$$

If $Pe >> 1$ the depletion zone is much thinner than h and, in this case, convection is the dominant transport mechanism, if $Pe << 1$ molecular diffusion predominates across the channel. Various flow conditions have been discussed by Squires et al., showing that typical value of Pe can be in the order of 10^5, but that low Pe values are essential for sensors designed to achieve the full collection of analytes from their solution on a sensor surface [26]. The region near the surface where the analyte is depleted is called the diffusion boundary layer (DBL) and has the characteristic thickness δ_D.

The DBL concept was first introduced by Nernst as the "diffusion layer" (stagnant film) model [238]. The model assumes that under steady-state conditions Fick's first law becomes simplified as the flux through the thin stagnant film towards the interface, depending on the constant concentration gradient measured at the two boundaries of the film: $j_M = D\partial c/\partial z \approx D(c_B - c_S)/\delta_D$. Here, D/δ_D can be defined as a mass transfer coefficient (k_m, typical units of cm s^{-1}) determining the rate of the mass transport process. A simplified version of the (25)–(27) PDE model can be obtained if we divide the inside space of the flow cell into two plane-parallel compartments according to the DBL concept. Let us suppose that the concentration in the outer compartment is uniform both in space and time and equal to the injected bulk concentration c_B. The inner compartment is the DBL itself, and the boundary between the two compartments is determined by the DBL thickness δ_D. If the following assumptions are made: (i) the concentration is in a steady-state ($dc/dt = 0$); (ii) the velocity profile close to the surface is linear (in case of rectangular channel geometry, $v(z) = 4zu_{max}/h$ at $z/h << 1$); (iii) diffusion in the direction of convective flow can be neglected ($\partial^2 c/\partial x^2 = 0$); and (iv) the surface acts as a perfect sink ($c_S = 0$, i.e., it can bind analytes infinitely fast and has infinite capacity), then the (25) convective–diffusive equation can be simplified [222] to

$$0 = D\left(\frac{\partial^2 c}{\partial z^2}\right) - u_x(z)\frac{\partial c}{\partial x} \quad (29)$$

This system can be analytically solved as first shown by Lévêque [239] for an equivalent heat transport problem. The problem was extensively detailed in terms of mass transport by Levich, who delivered the solution for the case of laminar flow in tube and for various other systems [240]. The flux density governed by diffusion towards the cylindrical wall of a tube can be written as

$$j_{\mathrm{M}} = \frac{D}{\delta_{\mathrm{D}}} c_{\mathrm{B}} = 0.67 \left(\frac{u_{\max}}{Drx}\right)^{1/3} D c_{\mathrm{B}} = k_{\mathrm{m}} c_{\mathrm{B}} \tag{30}$$

where r is the inner tube radius and x is the distance from the tube inlet to the position of interest (e.g., where the biosensing measurement is taking place) exposed to the mass flux. This is the Lévêque solution, which actually does not consider any interfacial binding kinetics. One main implication directly obtained from this formula is that it gives an analytical expression for the DBL thickness as $\delta_{\mathrm{D}} = (1/0.67)(Drx/u_{\max})^{1/3}$ and thus also for k_{m}.

Levich's related research mainly focused on electrochemistry, in particular to calculate the limiting electric current of electrochemical cells under fluid motion. Based on his landmark work, further efforts of Blaedel [241,242], Klatt [243] and Matsuda [244] provided the solution of Eq. (29) for various electrode designs including tubular and channel electrodes [245–248]. In case of tube geometry with circular cross section Eq. (30) applies, while for channels where the cross section is rectangular, the flux density is

$$j_{\mathrm{M}} = \frac{D}{\delta_{\mathrm{D}}} c_{\mathrm{B}} = 0.67 \left(\frac{u_{\max}}{Dhx}\right)^{1/3} D c_{\mathrm{B}} = k_{\mathrm{m}} c_{\mathrm{B}} \tag{31}$$

Here, h is the inner half thickness of the channel as shown in Fig. 5 B. Note that this expression is identical to Eq. (30) using the substitution of $r = h$. Regarding Eqs. (30) and (31), the extensive literature is quite confusing since many publications use different equation forms, which makes it hard to recognize that they are, in fact, identical. It can be seen that δ_{D} depends on coordinate x with power 1/3 along the channel, providing its characteristic shape as shown in Fig. 5 B. Also depending on the channel height, the value of δ_{D} is in the order of 10–100 μm. For instance, considering a standard OWLS flow cell with dimensions of $l = 8$ mm, $x = 4$ mm, $w = 2$ mm, $h = 0.4$ mm (assuming channel geometry) as well as volumetric flow rate of $Q = 1$ μL s^{-1} and protein molecules with $D = 8.8 \times 10^{-7}$ cm^2 s^{-1}, the value of δ_{D} is 79.8 μm.

The above theoretical and experimental studies in electrochemistry provided a solid foundation for the discussion of mass transport problems in biosensors. As shown by Lok et al. for a fluidic cell of a total internal reflection fluorescence (TIRF) system and by Sjölander and Urbaniczky [223] for SPR cells, practically the same flux formula is valid as the formula applied for electron transport in channel electrodes. In the case of OWLS fluidics, Ramsden and Kurrat used the formula provided by Levich for tubes [187,249,250] written as: $\delta_{\mathrm{D}} = (1/0.67)[(2/3) DrxA/Q]^{1/3}$, where the rxA term can be combined in one parameter that depends only on cell geometry [27,251]. For the widely used Biacore SPR setups, the average $<k_{\mathrm{m}}>$ is expressed by the following formula [252,253]:

$$\langle k_{\mathrm{m}} \rangle = 0.98 \left(\frac{D}{b}\right)^{2/3} \left(\frac{Q}{0.3wl}\right)^{1/3} \tag{32}$$

where b is the full thickness of the channel ($b = 2h$) as well as w and l are the channel width and length, respectively. This equation defines an average k_{m} (and thus average flux) over the full length l of the channel, and it can be directly obtained from Eq. (31) by integrating from $x = 0$ to l according to x and dividing with l [224,254]. Another version of Eq. (32) can be found in Refs [254,255], where the length of the sensing area and its location in the flow cell relative to the inlet are also taken into account.

When the surface is assumed to be a perfect sink, i.e., all the analytes are continuously bound to the surface with an infinitely fast rate ($k_{\mathrm{a}} \to \infty$ if there were no energy barrier [184]), the surface concentration is zero ($c_{\mathrm{S}} = 0$) and the flux is $j_{\mathrm{M}} = k_{\mathrm{m}} c_{\mathrm{B}}$. This is valid for electrons in electrochemistry but not for analyte binding in biosensing. When the binding process has an energy barrier (finite k_{a}), not all analytes transported to the surface will be immediately bound. Thus, the energy barrier retards adsorption and opposes depletion in the immediate vicinity of

the surface resulting in $c_{\mathrm{S}} > 0$ (although still lower than c_{B}) and $j_{\mathrm{M}} = k_{\mathrm{m}}(c_{\mathrm{B}} - c_{\mathrm{S}})$. This means that the binding process will be no longer fully transport–limited [184]. Note that the thickness of this vicinal region demarcated by the distance δ_{S} from the surface is of the order of molecular dimensions (i.e., a few nm) as illustrated in Fig. 5 C. As shown by Ramsden [187], the change of analyte concentration within this layer can be written as

$$\frac{dc_{\mathrm{S}}}{dt} = \frac{1}{\delta_{\mathrm{S}}} \left[D \frac{c_{\mathrm{B}} - c_{\mathrm{S}}}{\delta_{\mathrm{D}} - \delta_{\mathrm{S}}} - k_{\mathrm{a}} c_{\mathrm{S}} \phi + k_{\mathrm{d}} M \right] \tag{33}$$

This equation should be solved simultaneously together with the rate equations written in terms of adsorbed mass (see Eq. (15)). In this way, the PDE model could be reduced to a system of coupled ordinary differential equations (ODE). The main difficulty of solving these equations is that we do not accurately know the value of δ_{S}. Another way for dealing with the influence of binding kinetics to the surface concentration is the projection of dc_{S}/dt into the whole DBL, merging δ_{S} and δ_{D} [219,225,256–258]:

$$\frac{dc_{\mathrm{S}}}{dt} = \frac{1}{\delta_{\mathrm{D}}} \left[D \frac{c_{\mathrm{B}} - c_{\mathrm{S}}}{\delta_{\mathrm{D}}} - k_{\mathrm{a}} c_{\mathrm{S}} \phi + k_{\mathrm{d}} M \right] \tag{34}$$

This latter approach became standard in the two-compartment analysis when dc_{S}/dt is taken into account [225]. However, the accurate form is Eq. (33), as the volumetric concentration c_{S} should be defined in a thin film close to the surface (Fig. 5 C). Being an undetermined parameter, the $1/\delta_{\mathrm{S}}$ term often referred to be as the ratio of unit volume and surface area (S/V). Intermediate between Eqs. (33) and (34) is if we define an average concentration c_{D} in the DBL that can be written as $c_{\mathrm{D}} = c_{\mathrm{B}} - (c_{\mathrm{B}} - c_{\mathrm{S}})/2$, then its change in time is $dc_{\mathrm{D}}/dt = 1/2(dc_{\mathrm{S}}/dt)$. Considering that Eq. (34) is an expression for dc_{S}/dt, we find:

$$\frac{dc_{\mathrm{S}}}{dt} = \frac{1}{\delta_{\mathrm{D}}/2} \left(D \frac{c_{\mathrm{B}} - c_{\mathrm{S}}}{\delta_{\mathrm{D}}} - k_{\mathrm{a}} c_{\mathrm{S}} \phi + k_{\mathrm{d}} M \right) \tag{35}$$

The thickness of the surface zone where dc_{S}/dt should be considered can be eliminated from Eqs. (33) and (34) if we make further assumptions. Let us assume that the flux j_{M} and j_{R} are balanced, which means that c_{S} is in a steady-state ($dc_{\mathrm{S}}/dt = 0$) [184,250,252]. If we also suppose that next to δ_{D}, δ_{S} can be neglected ($\delta_{\mathrm{D}} - \delta_{\mathrm{S}} \approx \delta_{\mathrm{D}}$), this allows for the elimination of δ_{S}. Reordering Eq. (33) one obtains an explicit formula for c_{S}:

$$c_{\mathrm{S}} = \frac{c_{\mathrm{B}} D/\delta_{\mathrm{D}} + k_{\mathrm{d}} M}{k_{\mathrm{a}} \Phi + D/\delta_{\mathrm{D}}} \tag{36}$$

which is coupled with the equation describing the adsorption:

$$\frac{dM}{dt} = k_{\mathrm{a}} c_{\mathrm{S}} \Phi - k_{\mathrm{d}} M \tag{37}$$

The presence of Φ makes it clear that not only the energy barrier but also the presence of previously adsorbed analytes prevent the surface from being a perfect sink.

The approach of Eq. (36) is the standard method for calculating c_{S} when mass transport is considered. The use of k_{m} enables a simple interpretation of the coupled transport-adsorption process using the sequential scheme:

$$P_{\mathrm{B}} \underset{k_{\mathrm{m}}}{\overset{k_{\mathrm{m}}}{\rightleftharpoons}} P_{\mathrm{S}} \underset{k_{\mathrm{d}}}{\overset{k_{\mathrm{a}}}{\rightleftharpoons}} A_{\mathrm{r}} \tag{38}$$

where P_{B} and P_{S} represents analytes in the bulk phase and in the vicinity of the surface, respectively, and A_{r} denotes the reversible adsorbed form of the analyte. This interpretation became widely used for explaining mass transport limitations in the SPR literature [218,252,253,259]. In the field of protein adsorption kinetics, the effect of hydrodynamics is

mostly incorporated in δ_D. Nevertheless, the two methods are actually equivalent, and they can be easily converted to each other using the substitution $k_m = D/\delta_D$.

As discussed by Karlsson et al. [252], using this k_m–based interpretation of transport limitation, distinguishing between the transport- and binding–limited domains becomes straightforward. Substituting Eq. (36) into Eq. (37) one obtains

$$\frac{dM}{dt} = \frac{k_a}{1 + k_a\Phi/k_m} c_B\Phi - \frac{k_d}{1 + k_a\Phi/k_m} M \qquad (39)$$

where the term $k_f = k_a/(1 + k_a\Phi/k_m)$ can be taken as the forward and $k_r = k_d/(1 + k_a\Phi/k_m)$ as the reverse rate constants of the entire process (38). It can be deduced from Eq. (39) that if the ratio $k_a\Phi/k_m << 1$, then $k_f = k_a$ and $k_r = k_d$, meaning that adsorption is far from the transport–limited domain and is binding–limited. In case of $k_a\Phi/k_m >> 1$, then $k_f < k_a$ and $k_r < k_d$, presenting a transport–limited system. It can be additionally inferred from Eq. (36) that in this case $c_S \approx Mk_d/k_a$ (assuming $c_Bk_m/k_a \to 0$).

Eq. (39) also helps to understand how the association and dissociation phases of the entire adsorption curve can be distinguished in the data evaluation. In the initial linear phase of the association section, the adsorbed mass is small ($M \approx 0$), thus $k_fc_B\Phi$ dominates and k_rM can be neglected. Looking at the dissociation section, if it is assumed that $c_B = 0$ from the starting time of washing (which does not always hold as shown in Section 3.5.3), then $dM/dt = k_rM$ and the kinetics are not affected by c_S. As a result, for the binding–limited case k_a and k_r can be determined by analyzing the initial phase of association section and the entire dissociation section separately. The analysis of initial phase also enables k_m to be determined. As Φ has its highest value at the starting point of the adsorption ($\Phi = 1$ at $t = 0$) and decreases over time, transport limitation is most probable at the beginning of the process. Here, practically the ratio k_a/k_m determines whether a transport or binding limitation must be considered. When the kinetics is heavily transport–limited (initial phase), practically $k_f = k_m$ and $dM/dt = k_mc_B\Phi$. This relation allows k_m to be determined by fitting the initial phase of the M vs. t dataset and taking the slope of the fitted line [260]. The strategy also allows for the determination of D: once k_m is obtained, D can be calculated using Eqs. (31) or (32) [225]. As seen from Eq. (39), within the intermediate domain ranging between the two limits, the simple linear formula $k_f^{-1} = k_a^{-1} + k_m^{-1}$ can be used for the determination of k_a in the initial phase from the experimentally observed k_f and calculated k_m. Nevertheless, Déjardin and co-workers [261,262] showed that this method can result in considerable error as δ_D is assumed to be independent of k_a and c_S (Lévêque solution), however this is not true. Analyzing the exact solution of Eq. (29) when adsorption is also considered, they provided more accurate linear approximations for the two limits determining an intermediate domain in between. As such, close to binding control, $k_f^{-1} = 0.827k_a^{-1} + k_m^{-1}$, while close to transport control, $k_f^{-1} = k_a^{-1} + 0.684k_m^{-1}$. Here, k_a is related to a given position x on the surface. It was also pointed out that considering the average value of the rate parameters over the full length of the channel ($<k_f>$, $<k_a>$, $<k_m>$), the error is smaller. Déjardin et al. developed a formula that describes the relationship of k_f, k_a as well as k_m and allows for calculating k_a from initial phase data. For further details about this model, see Ref. [262]. Nevertheless, under certain conditions, the adsorption regime may strongly vary along the length of the channel.

As demonstrated by a thorough analysis in the paper of Myszka and co-workers [225], the two-compartment model can provide excellent accuracy when fitting transport–limited data and it serves as a fair approximation of the PDE model. The simplicity, implying a meagre use of computational resources, and its straightforward interpretation has made the two-compartment approach the primary method in the kinetic analysis of measurements under transport limitation [219]. However, the model tends to fail if transient regimes influence the kinetics, e.g. when an analyte solution is suddenly injected into the flow cell.

With the motivation of refining the two-compartment model, three- [219] and multi-compartment [258] models have been developed. Future access to even larger computational power may allow these models to be further elaborated.

3.5.3. Flushing effect

Standard kinetic models are assuming that the bulk concentration changes infinitely fast when, for example, the baseline phase of a biosensing run is switched to the analyte adsorption phase; i.e., concentration as a function of time follows a step function [184]. However, depending on the geometry of the flow cell, changing one solution to another (flushing the cell with the next solution) may take significant time. Changing water to an aqueous glycerol solution is an effective test to see how the bulk concentration actually develops under given hydrodynamic conditions. Glycerol is a suitable compound since it does not adsorb to the sensor surface, diffuses relatively fast ($D_{glycerol} = 1.06 \times 10^{-5}$ cm^2 s^{-1} vs. $D_{protein} \approx 10^{-7}$ cm^2 s^{-1}), and thus the obtained signal is practically not affected by diffusive transport.

The RI change in Fig. 6 A demonstrates such an experiment with OWLS employing an SH812-08 flow cell (MicroVacuum Ltd.) and 1 μL s^{-1} flow of, first, DI water, then 6% (w/w) aqueous glycerol solution, and lastly again DI water. This observed time–dependence in the variation of concentration can strongly affect the biosensor response. Note that in case of an OWLS or other optical biosensing experiment, where the adsorbed mass is calculated from the effective RIs using n_C of the bulk solution, which is proportional to c_B, the n_C profile should be taken into account. A simple method of considering the concentration variations during flushing is to model its kinetics with the logistic function (Richard's curve), which has the form [263]:

$$Y = Y_0 + \frac{Y_{max} - Y_0}{(1 + e^{-qt})^{1/g}} \qquad (40)$$

where Y_0 and Y_{max} are the initial and maximal values of the fitted curve and q and g are fitting parameters. As shown in Fig. 6 B–C, the change in n_C during the two flushing phases could be fitted with this equation with excellent accuracy. The obtained fit parameters (given in the figure caption) can then be used when flushing affects the transport–limited section of the adsorption kinetic curve. The flushing curve can be incorporated if the steps in the original $c_B(t)$ curve are replaced by a continuous sigmoid-like shape determined by the fitted q and g parameters (Y_{max} should be equal to c_B as well as Y_0 is determined at the curve baseline). Further details about the inclusion of flushing effects in kinetic analysis will be given in Section 4.1.

4. Searching for the best fitting kinetic model; effect of varying model parameters

One can obviously see on a typical adsorption curve that the signal (commonly expressed as adsorbed mass) converges to saturation. In addition, a significant number of adsorbates may desorb when the solution is exchanged to baseline buffer, but a comparable number remains on the surface. Thus, the washing phase plays a key role in analyzing adsorption curves, as it demonstrates that there is both a reversibly and a quasi-irreversibly adsorbed amount, indicating that the adsorbates may have at least two different states on the surface.

A model that considers both reversibly and irreversibly adsorbed molecules on the surface should define two distinct states for the adsorbate characterized by separate mass values, M_r and M_i, respectively. In a label-free measurement, a total adsorbed mass, $M = M_r + M_i$, is observed. Two types of models that provide the simplest approach for describing such a system are the two-state parallel and consecutive models, schematically illustrated in Fig. 7. Our example system shown in the figure is represented by the adsorption of wild-type flagellin (FliC) molecules on hydrophobized OWLS sensor surfaces, characterized
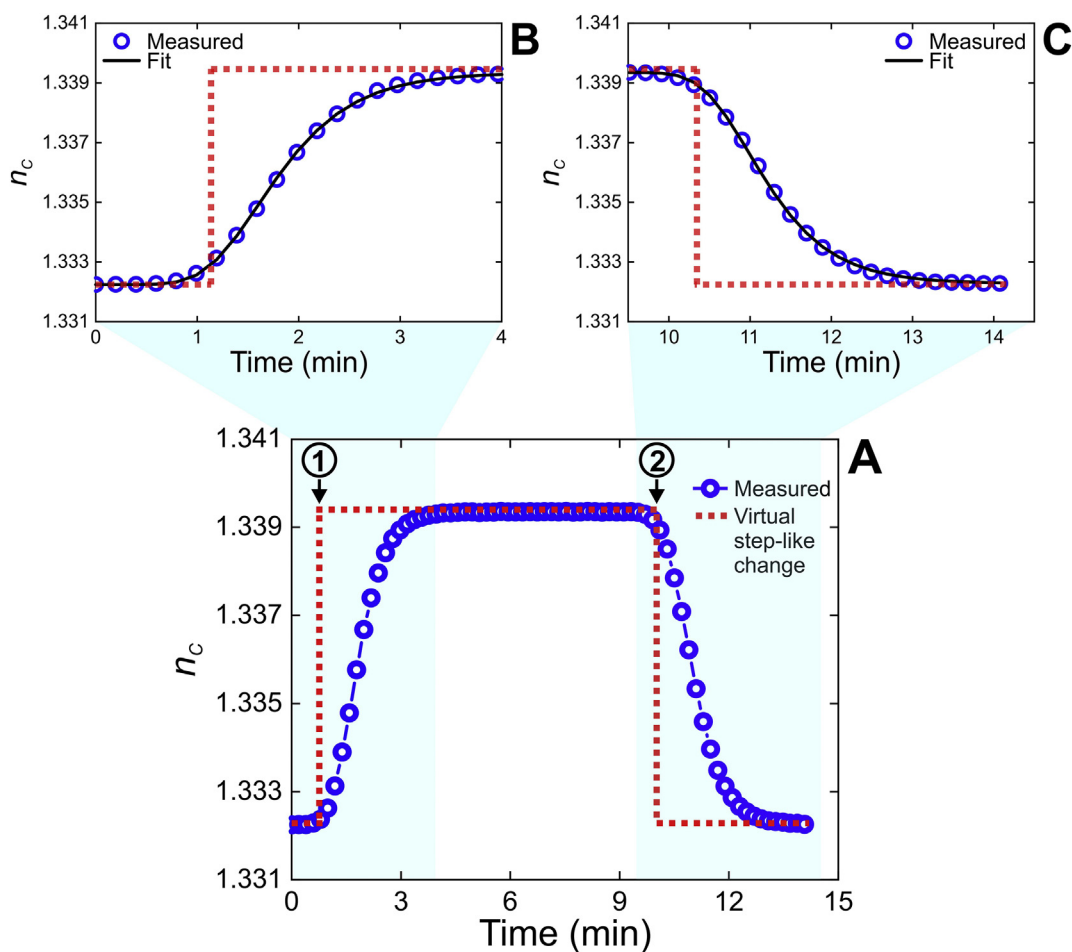
Fig. 6. A. Flushing of an SH812-08 OWLS flow cell with 6% (*w/w*) glycerol solution. Measured solution RI (n_C) as a function of time (blue circles). Experimental phases: introduction of glycerol solution (1) and DI water (2) into the flow cell. n_C values were calculated based on the 3–layer mode equations. The dashed red lines represent the unrealistic, but commonly usedcase, when the change of bulk concentration in the flow cell is assumed to be immediate and is described by a step function. B–C. Two relevant sections of the flushing curve were fitted by Eq. (40) (logistic function), resulting in the fitted curves (black solid line) and the following fit parameters: $q = 0.03277$, $g = 0.04284$ (B); $q = 0.03018$, $g = 0.06972$ (C).
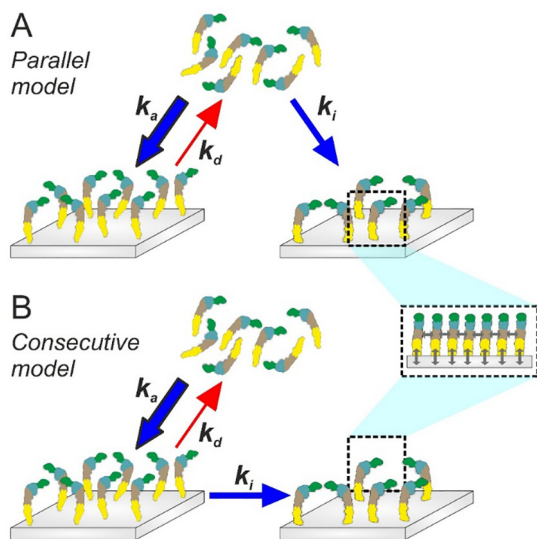
Fig. 7. Schemes of the two-state parallel and consecutive adsorption kinetic models. The example schemes shown here represent flagellin adsorption on a hydrophobic surface. In the presence of kosmotropic salts [251], flagellin molecules adsorb on hydrophobic surfaces predominantly through their disordered hydrophobic D0 domain (shown in yellow; other domains are represented with different colors) and form a layer where molecules are oriented perpendicularly to the surface. As illustrated with blue, wider arrows, kosmotropic salts significantly increase k_a. [Adapted from Ref. [251], copyright 2018 American Chemical Society].

in several studies in detail [251,264,265]. The bacterial filament monomer flagellin is an intensively studied protein owing to the ease of its modification by genetic engineering techniques, yielding various forms for a wide range of applications such as biorecognition element or anti-fouling coating (e.g., we showed that compact layers made of flagellin molecules can regulate bacterial adhesion [78]). Flagellins possess intrinsic anisotropy as they are asymmetric molecules with a capsule-like ellipsoidal shape. The anisotropy enables layers formed from the same molecules but different in surface mass, thickness and orientation under varying external conditions to be designed. The salt composition of the liquid medium can drastically affect the orientation of flagellin on the surface.

The reaction schemes and equations corresponding to the two models are given below. The equations on the left and right represent the parallel and the consecutive model, respectively.

Two-state parallel model	Two-state consecutive model
$P \underset{k_d}{\overset{k_a}{\rightleftharpoons}} A_r ; P \overset{k_i}{\rightarrow} A_i$ (41)	$P \underset{k_d}{\overset{k_a}{\rightleftharpoons}} A_r \overset{k_i}{\rightarrow} A_i$ (42)
$\dfrac{dM_r}{dt} = k_a c_S \Phi - k_d M_r$ (43)	$\dfrac{dM_r}{dt} = k_a c_S \Phi - k_d M_r - k_i M_r$ (44)
$\dfrac{dM_i}{dt} = k_i c_S \Phi$ (45)	$\dfrac{dM_i}{dt} = k_i M_r$ (46)
$\dfrac{dc_S}{dt} = \dfrac{1}{\delta_D/2}(D\dfrac{c_B-c_S}{\delta_D} - (k_a+k_i)c_S\Phi + k_d M_r)$ (47)	$\dfrac{dc_S}{dt} = \dfrac{1}{\delta_D/2}(D\dfrac{c_B-c_S}{\delta_D} - k_a c_S\Phi + k_d M_r)$ (48)
$c_S = \dfrac{c_B D/\delta_D + k_d M_r}{(k_a+k_i)\Phi + D/\delta_D}$ (49)	$c_S = \dfrac{c_B D/\delta_D + k_d M_r}{k_a\Phi + D/\delta_D}$ (50)

Both models consist of a coupled ODE system involving two ODEs for describing mass changes and one for considering variations in c_S (Eqs. (47) and (48)). Here, dc_S/dt calculation follows Eq. (35). In case of assuming $dc_S/dt = 0$, this latter ODE can be eliminated and c_S is calculated according to Eqs. (49) and (50). The formula for expressing Φ depends on the chosen RSA model where the shape of the adsorbates must be considered (Eqs. (22) or (23)). When calculating Θ using M_r and M_i, one can also take into account whether the two states are described with one footprint (a) (Eq. (21)) or whether they have two distinct footprints (a_r and a_i) (Eq. (24)).

In order to bring these detailed kinetic models into a realistic context and show their power in practice, we demonstrate their application to the kinetic modeling of FliC adsorption, which represents a much more complex process than simple Langmuir-type binding. Fig. 8 A shows the adsorption curves of FliC molecules added to the sensor surface in solutions containing different salts, NaF (chaotropic) or NaClO$_4$ (kosmotropic) [251]. Surface mass curves fitted using the two/state parallel model are also presented (Fig. 8 B, G). The salts were selected from the Hofmeister series, ions of which can regulate hydrogen bonding interactions of proteins and surfaces [48,251]. As demonstrated in Fig. 8, the salt has a significant effect on the adsorption kinetics. Both the data corresponding to reversibly and irreversibly adsorbed states are shown and plotted in different formats. The dM/dt vs. time graph shows the magnitude of rates over the measurement interval (Fig. 8 C, H) and the dM/dt vs. M graph indicates the relevant regimes and mechanism of adsorption (Fig. 8 D, I). In the latter graph, the slow increase in dM/dt shows that the adsorption is transport–limited and then, reaching the maximum rate, it becomes binding–limited, when the rate is determined by the area still available on the surface[. The nonlinear shape of the end tail in the descending phase suggests an RSA-type adsorption (see Fig. 3). Although the model considered diffusion, it failed in reproducing the

initial phase. Calculating k_m for the NaF measurement one can conclude that this system is far from remarkable transport limitation, as $(k_a + k_i)/k_m = 2.4 \times 10^{-2} << 1$. This suggests that not the transport, but flushing of the flow cell is responsible for the discrepancy between the observations and fit (Fig. 8 F, K). In the following, we analyze the effect of considering $dc_S/dt \neq 0$ and including flushing in the variation of c_B.

4.1. Dependence of the kinetic fit on fit parameters and model conditions

The dependence of the fitted RSA kinetic model on the fit parameters for protein adsorption has been analyzed by Kurrat et al. in depth [250]. The effect of hydrodynamic conditions on the observed kinetic curves has also been examined elsewhere, especially for SPR biosensors [225]. In this section we provide sets of simulated curves which are meaningful in demonstrating the effect of the kinetic regime and hydrodynamic conditions at which the system operates. The effect of systematically varied model parameters in the case of a Langmuir-type binding can be seen in Fig. 9 and Fig. 10. All the curves were simulated using our NBS-Kinetics software.

Similar tendencies can be observed for a more complex system than the Langmuir, as presented in Fig. 11 and Fig. 12. Here, varying kinetic curves are shown simulating the adsorption of flagellin molecules according to two-state parallel kinetics. It is obvious that if k_a increases, c_S will not follow c_B and the measured mass curve will be affected in the transient regime (see inset graphs in Fig. 11 B, D, F and Fig. 12 B), suggesting the need to calculate c_S as $c_S = c_B$ is not true.

Fig. 13 demonstrates how the fitted kinetic curve is influenced by calculating c_S with different ways and either considering flushing effect or not (for different model variations see the figure legend). As also shown in Fig. 8, the overall fit has a very good quality ($R^2 = 0.984$–0.996), however, there are larger errors around the transient
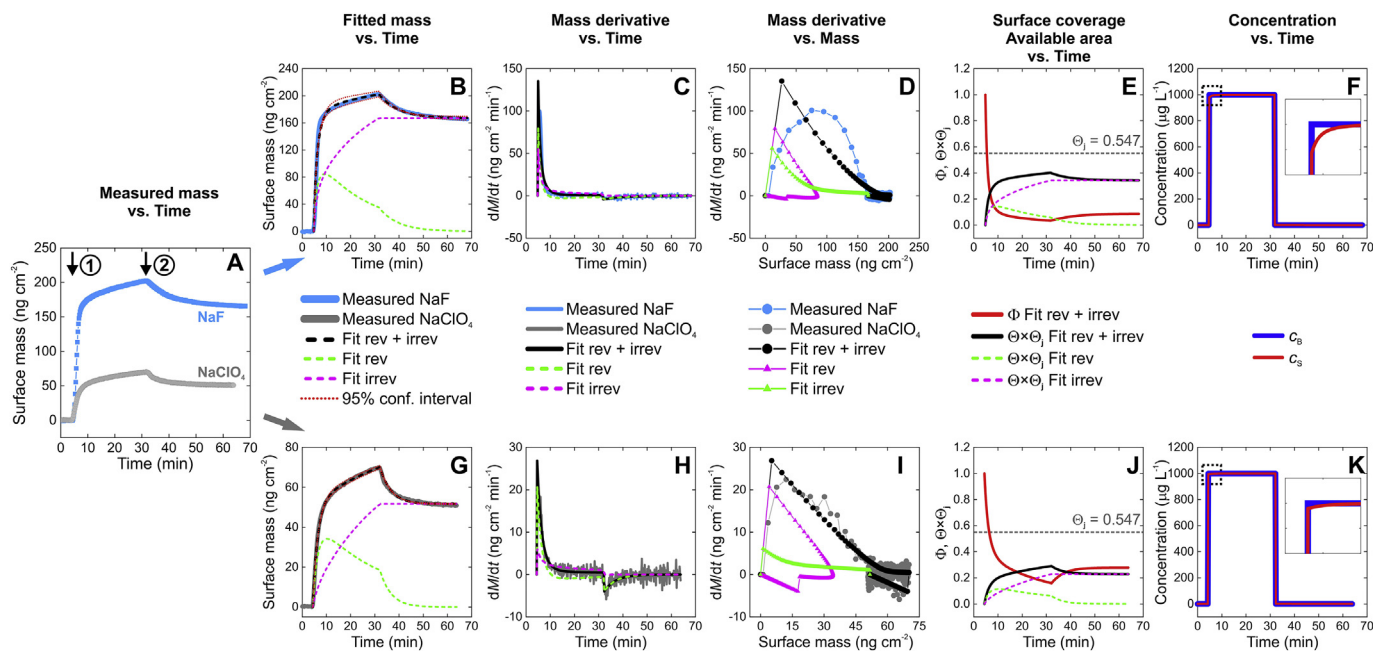
Fig. 8. Comprehensive analysis of adsorption kinetic data measured by a label-free biosensor. The measured raw curves (A) represent the adsorption of flagellin (FliC) molecules monitored by OWLS. Two datasets were analyzed: one when the protein solution contained a kosmotrope (NaF, blue curve) and one when it contained a chaotrope (NaClO$_4$, grey curve). The measured mass data were fitted with the two-state parallel RSA model using our developed kinetic analysis software. Fit results are shown according to the used two Hofmeister salts (top graphs: NaF, bottom graphs: NaClO$_4$). Arrows with the numerical markers indicate the start of adsorption (1) as well as the dissociation phase (2). The legends in the middle indicate the corresponding curves. B, G. Fitted kinetic curves showing the surface mass of the reversibly and irreversibly adsorbed components and their sum. C, H. Mass derivative highlighting the rate of variation in mass. D, I. Surface mass derivative as a function of surface mass illuminating the adsorption characteristics with time being implicit. E, J. Surface coverage and available area with the jamming limit Θ_j indicated. F, K. Variations in concentrations c_B and c_S as a function of time. Inset graphs highlights regions where c_S slightly deviates from c_B (of note, $dc_S/dt = 0$). Parameters obtained from the fits are the following: $k_a = 1.5 \times 10^{-6}$ cm s^{-1}, $k_d = 2.1 \times 10^{-3}$ s^{-1}, $k_i = 1.1 \times 10^{-6}$ cm s^{-1}, $a_r = 15$ nm^2, $a_i = 18$ nm^2, $R^2 = 0.9739$ (NaF); $k_a = 3.7 \times 10^{-7}$ cm s^{-1}, $k_d = 3.7 \times 10^{-3}$ s^{-1}, $k_i = 1.1 \times 10^{-7}$ cm s^{-1}, $a_r = 29$ nm^2, $a_i = 38$ nm^2, $R^2 = 0.9962$ (NaClO$_4$). Model conditions: $D = 8.8 \times 10^{-7}$ cm^2 s^{-1}, $c_B = 1000$ µg mL^{-1}, $Q = 1$ µL s^{-1}, $dc_S/dt = 0$, flow cell: OWLS SH-0812–08, $\delta_D = 79.8$ µm, $\Theta_j = 0.547$ (spherical objects; Φ was calculated accordingly).

k_a dependence
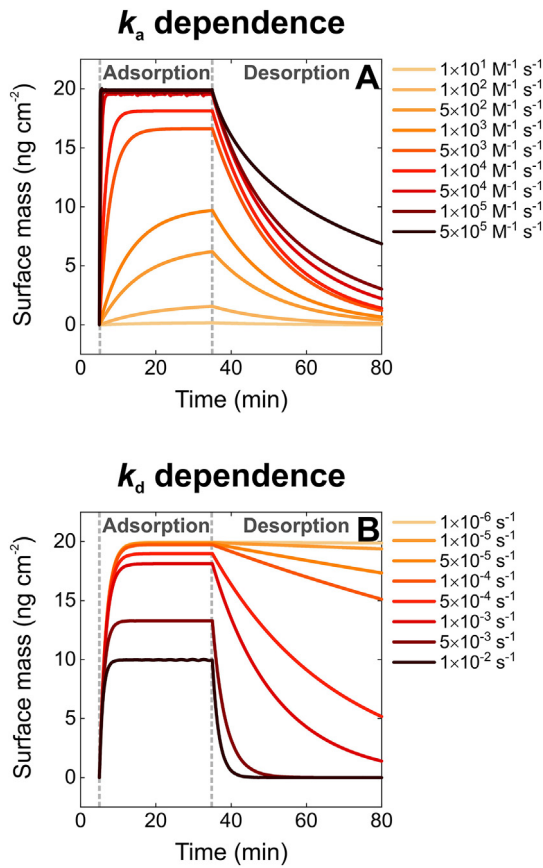
k_d dependence

Fig. 9. Dependence of a Langmuir-type adsorption kinetics on varying k_a and k_d kinetic rate constant values (A-B). All curves were generated using the *Simulation Tool* of the *NBS-Kinetics* software. Curves with different color tones ranging from pastel yellow to black indicate an increase in the related parameter value. Fixed model conditions (in case of the corresponding parameter was not varied): one-state L–A binding described by Eq. (37) and (36); c_B = 1000 nM, Q = 10 μL s^{-1}, MW = 6.65 kDa, $k_a = 1 \times 10^4$ M^{-1} s^{-1}, $k_d = 1 \times 10^{-3}$ s^{-1}, a = 55.4 nm^2.

phases. The initial adsorption section was best fitted by the model assuming $dc_S/dt = 0$ and involving flush effect (B). However, these conditions did not facilitate a better fitting of the washing section (C, D), and the best performing model was in fact the simplest one ($dc_S/dt = 0$, no flush). This interesting discrepancy should be lying on conditions which were not implemented in the model, including hydrodynamic parameters that are neglected in the simplified equations. Fitting the full PDE model is a good candidate to resolve such a minute effects, however as the best of our knowledge no attempt to fit the full PDE model has been published so far. Although the effect is minute, it can result in significant deviations in the fitted kinetic data, as seen in Table 1.

As seen in Fig. 14, considering larger V/S values in Eq. (47), c_S becomes heavily affected by V/S, which should be far from reality. The tendency of c_S shape shows that choosing smaller V/S values, c_S converges to c_B, suggesting that the simplified calculation mode represented by Eq. (49) provides a good approximation for c_S.

4.2. Surface energetics

The question of why certain types of molecules tend to adsorb on solid surfaces can be explained by energy conditions with energy contributors of the adsorbing molecules, the solvent molecules and the surface. In terms of proteins, the determinative energy–related parameters has been extensively studied by Norde and co-workers [266–268]. Information on the interaction of the adsorptive with the available surface area is contained in the rate coefficients. As the

adsorption and desorption are generally considered as thermally activated processes, it is assumed that the rate coefficients can be written in the form

$$k = F \cdot e^{-U_{act}/(k_B T)} \tag{51}$$

where U_{act} is an activation energy for the process, and F an appropriately dimensioned frequency factor. In order to identify the forces involved, it can be extremely valuable to measure the adsorption kinetics for a given protein/surface combination under different solution conditions, i.e. pH, ionic strength [269], cosolute composition, and temperature. Electrostatics alone do not seem able to account completely for what is observed in many cases. Complementary techniques, including titration of adsorbed proteins, electrokinetic measurements of the surface potential of absorbed layers, and the direct measurement of the surface forces between adsorbed layers are making an important contribution towards resolving the current ambiguities. However, under physiological conditions, electrostatic forces may be negligible [48].

Kinetic analysis of biosensor data also allows for estimating the adsorbate–water–substrate interfacial tension (γ_{PWS}) of the adsorbed species (e.g., a P protein molecule), which is defined as the specific work of adsorption during the adsorption process. To arrive at the determination of γ_{PWS} based on kinetic data, we first write the Gibbs free energy change during the adsorption process (work of adsorption, ΔG_a) as [184,251]

$$\Delta G_a = \Delta G_{PW} + \Delta G_{SW} + \Delta G_{PS} = -\gamma_{PW}a - \gamma_{SW}a + \gamma_{PS}a \tag{52}$$

where ΔG_{PW}, ΔG_{SW}, ΔG_{PS} as well as γ_{PW}, γ_{SW}, γ_{PS} are the Gibbs free energy changes and interfacial tensions at the protein–water substrate–water and protein–substrate interfaces (water can be substituted by any solvent). Here we assumed that the area of adsorbed protein in contact with the surface can be given by the a footprint and that in the dissolved state this area is surrounded exclusively by solvent molecules. Upon adsorption the area a is disappearing at the PW and SW interfaces and it is appearing at the PS interface. Rearranging Eq. (52) one can write

$$\Delta G_a = -(\gamma_{PW} + \gamma_{SW} - \gamma_{PS})a = -\gamma_{PWS}a \tag{53}$$

Here, a new quantity γ_{PWS} is introduced which is the protein–water–substrate interfacial tension defined as $\gamma_{PWS} = -(\gamma_{PW} + \gamma_{SW} + \gamma_{PS})$. An attempt to link ΔG_a to the quotient of the rate constants has been already made. Applying Eq. (51) for both k_a and k_d, the following equation can be obtained [251]:

$$\frac{k_a}{k_d \delta_S} = e^{-\Delta G_a/(k_B T)} \tag{54}$$

where the factor δ_S characterizes the thickness of surface adsorption zone potentially taking a value in the nanometer range. The reason for the appearance of δ_S is to harmonize the dimensions in Eq. (54) and convert the k_a dimension cm s^{-1} dimension to s^{-1}. Adsorbing species closer to the surface than δ_S are potentially in adsorbed state. In this sense, δ_S can be used to convert the volume concentration into surface concentration in a straightforward way and we can define a surface related $k_a' = k_a/\delta_S$, which can substitute k_a in, e.g. Eq. (43) such as $k_a'(c_S\delta_S)\Phi$. Rearranging Eq. (54) one can find that

$$\Delta G_a = -k_B T \ln \frac{k_a}{k_d d} \tag{55}$$

Expressing ΔG_a based on Eq. (53) and substituting into the above formula we arrive to calculate γ_{PWS} using k_a and k_d determined from a kinetic analysis [251]:

Q dependence
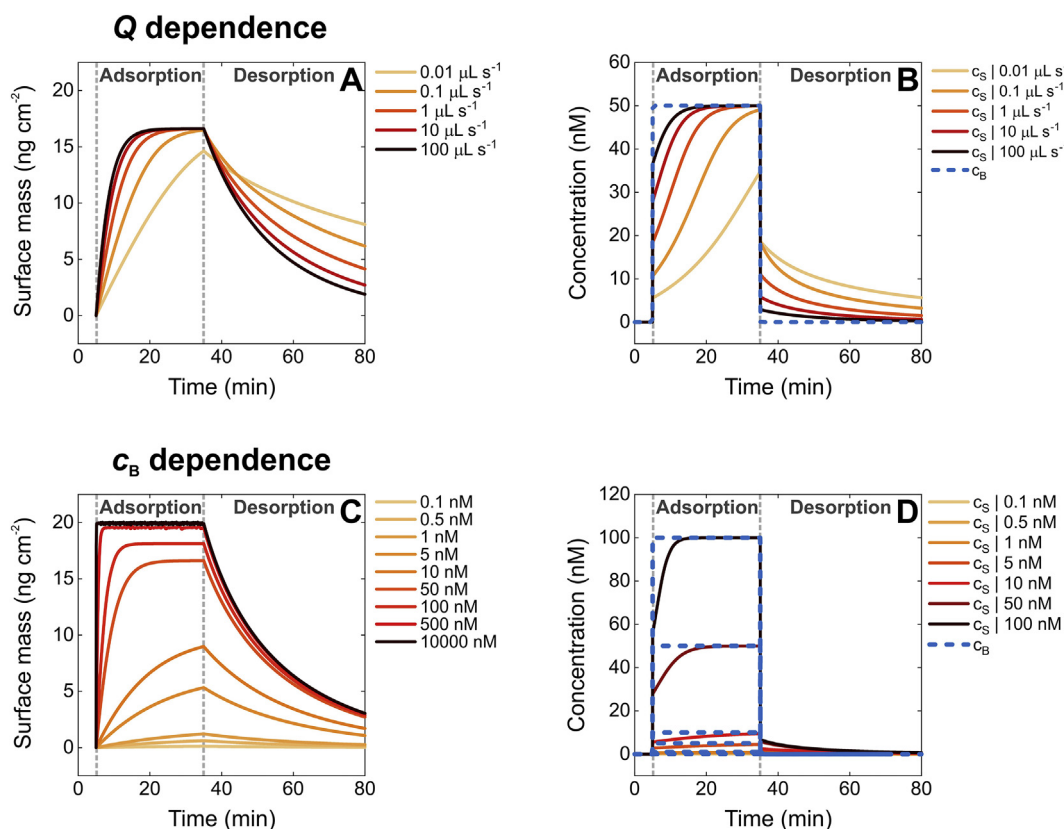
c_B dependence

Fig. 10. Dependence of a Langmuir-type adsorption kinetics on Q volumetric flow rate (A–B) and c_B bulk concentration (C–D) values. All curves were generated using the *Simulation Tool* of the *NBS-Kinetics* software. Curves with different color tones ranging from pastel yellow to black indicate an increase in the related parameter value. Fixed model conditions (in case of the corresponding parameter was not tuned): one-state L–A binding described by Eq. (37) and (36); $c_B = 50$ nM, $Q = 10$ μL s^{-1}, MW = 6.65 kDa, $k_a = 1 \times 10^5$ M^{-1} s^{-1}, $k_d = 1 \times 10^{-3}$ s^{-1}, $a = 55.4$ nm^2.

$$\gamma_{PWS} = \frac{k_B T}{a} \ln \frac{k_a}{k_d d} \tag{56}$$

In numerical calculations, $\delta_S = 10$ nm can be used, which is a reasonable approximation for the thickness of surface vicinal region. γ_{PWS} is a complex quantity, depending on the water-exposed adsorbate surface, the nature of substrate surface as well as the quality and concentration of dissolved cosolutes. The significance of γ_{PWS} is that it is a more precise characteristic parameter of the system than the previously studied γ_{PW} which does not deal with the hydrophobic/hydrophilic properties of the substrate. Moreover, the accuracy of the determined γ_{PW} was especially affected by the difficulties in determining interfacial tension in microscopic conditions. Based on these considerations, γ_{PWS} is assumed to be a critical parameter in the phenomenological interpretation of protein adsorption processes, such as γ_{PW} for conformation–related phenomena.

The application of the above theory in case of measured kinetic data was demonstrated in Kovacs et al. [251], where the dependence of flagellin–related γ_{PWS} on the presence of different Hofmeister salts was investigated. The calculated γ_{PWS} values followed the expected tendency (the presence of kosmotropes increased γ_{PWS} while chaotropes decreased) as well as agreed with (the available few) literature values, confirming the validity of calculating γ_{PWS} based on kinetic data.

5. Combined label-free measurements: unraveling structure and kinetics from biosensor data

5.1. Essence of combination. Hydration and viscoelasticity

In spite of the availability of various label-free techniques, each of which can monitor molecular interactions with good sensitivity and

throughput, no single technique can achieve a full characterization of biofunctional coatings. Soft and hydrated interfacial layers present the greatest challenge due to their small optical contrast and conformational variability. To expand the range of analysis, combined label-free methods have been developed, primarily exploiting the advantages of optical and acoustic biosensors. In principle, optical methods are not sensitive to solvent molecules associated with the adlayer, since compared to the solvent molecules already present in the bulk phase, they do not add a significant shift to the RI. As a result, when data are referenced to the baseline, the associated solvent is in effect subtracted, which means that only the signal of deposited analytes themselves (so-called "dry" mass) is recorded. Contrary to optical methods, QCM measures both the dry analyte and any associated solvent, because it is sensitive to *any* added mass within the penetration depth that oscillates together with the crystal (see the sensitivity of QCM to layer hydration and viscoelasticity in Fig. 15). Although the solvated mass in itself does not allow for the determination of solvent content, by using the "dry" OWLS mass measured on the same layer one can separate the solvated mass (M^{QCM}) into dry analyte ($M^{optical}$) and solvent masses (M^{QCM}–$M^{optical}$) and determine the solvation factor (H_A) [270,271]:

$$H = \frac{M^{QCM} - M^{optical}}{M^{QCM}} \tag{57}$$

A detailed in Section 2.1.4, QCM can provide quantitative information about the viscoelasticity of adlayers (Fig. 15). Evaluation of QCM data by the Kelvin–Voigt model requires knowledge of the mass density of the adlayer. Hitherto, when the layer is assumed to be strongly hydrated, $\rho_A = 1000$ kg m^{-3} is commonly used, with little understanding of the validity of the assumption. Now, the value of ρ_A can be determined from the measured optical and QCM mass data (the 3rd overtone
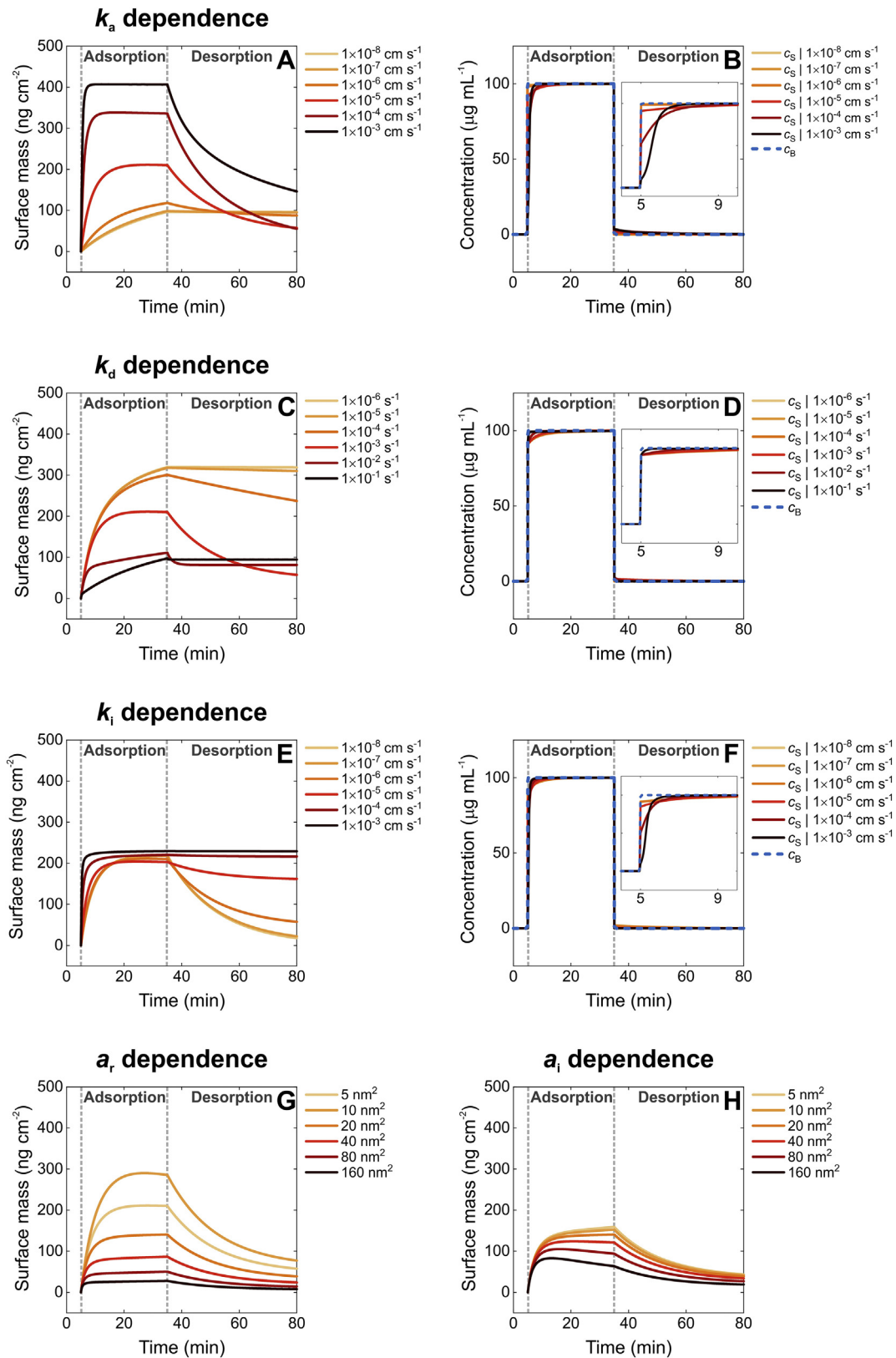
Fig. 11. Dependence of a two-state parallel type adsorption kinetics on varying k_a, k_d and k_i kinetic rate constant (A–B, C–D, E–F) as well as a_r and a_i footprint (G-H) values. Besides the surfaces mass curves (A, C, E, G, H), the given c_B and calculated c_S curves are also shown (B, D, F). All the curves were generated using the *Simulation Tool* of the *NBS-Kinetics* software. Curves with different color tones ranging from pastel yellow to black indicate an increase in the value of the related parameter. The model parameters used for the simulations were set based on a fit to FliC protein adsorption experiment in the presence of $NaClO_4$. Fixed model conditions (in case of the corresponding parameter was not tuned): two-state parallel model described by Eq. (43), (45) and (49); $dc_S/dt = 0$, $c_B = 100$ μg mL^{-1}, $Q = 1$ μL s^{-1}, MW = 51.5 kDa, $D = 8.8 \times 10^{-7}$ cm^2 s^{-1}, $k_a = 1 \times 10^{-5}$ cm s^{-1}, $k_d = 1 \times 10^{-3}$ s^{-1}, $k_i = 1 \times 10^{-8}$ cm s^{-1}, $a_r = 10$ nm^2, $a_i = 20$ nm^2.

Fig. 12. Dependence of a two-state parallel type adsorption kinetics on varying Q volumetric flow rate (A-B) as well as c_B bulk concentration (C-D) values. Besides surfaces mass (A, C), the given c_B and calculated c_S curves are also shown (B, D). All the curves were generated using the *Simulation Tool* of the *NBS-Kinetics* software. Curves with different color tones ranging from pastel yellow to black indicate an increase in the value of the related parameter. The model parameters used for the simulations were set based on a fit to FliC protein adsorption experiment in the presence of NaClO$_4$. Fixed model conditions (in case of the corresponding parameter was not tuned): two-state parallel model described by Eq. (43), (45) and (49); dc_S/d$t = 0$, $c_B = 10 \, \mu g \, mL^{-1}$, $Q = 1 \, \mu L \, s^{-1}$, MW $= 51.5$ kDa, $D = 8.8 \times 10^{-7} \, cm^2 \, s^{-1}$, $k_a = 1 \times 10^{-5} \, cm \, s^{-1}$, $k_d = 1 \times 10^{-3} \, s^{-1}$, $k_i = 1 \times 10^{-8} \, cm \, s^{-1}$, $a_r = 10 \, nm^2$, $a_i = 20 \, nm^2$.

QCM Sauerbrey mass ($M^{QCM,S}$) is recommended) if the density of adsorbing and solvent molecules are known [67,107]:

$$\rho_A = \frac{M^{QCM,S}}{\frac{M^{optical}}{\rho_{analyte}} + \frac{M^{QCM,S} - M^{optical}}{\rho_{solvent}}} \quad (58)$$

where $\rho_{analyte}$ and $\rho_{solvent}$ are the mass density of surface bound analyte and solvent molecules, respectively. Due to the ability to obtain information about the amount of coupled water inside the adlayer complemented by additional measured properties such as dominant chain conformation and viscoelasticity (Fig. 15 and 17), the combination of QCM and OWLS data offers an excellent tool for biolayer research [107,272].

The combination of QCM with optical techniques has been realized in three ways: (i) combination in one device probing exactly the same surface simultaneously by the two techniques; (ii) one device but the measurement is performed on separate surfaces using separate flow cells; and (iii) measurement by separate instruments on different surfaces albeit at the same time. Although the first approach is obviously the best, it is a great challenge for instrument developers; nevertheless SPR-QCM [273] and SE-QCM [106,274–276] (ellipsometry-compatible QCM module from Biolin Scientific AB) setups have been already demonstrated, but despite the benefits offered by waveguide–based methods, the combination with QCM has still not been achieved. Currently (ii) is available (OWLS QCM 3000 Biosensor system from MicroVacuum Ltd. [277]), allowing the same reagent solution to be used and maintaining the same temperature of the surfaces. The combination of QCM and OWLS data measured in parallel OWLS-QCM experiments have already shown its potential in hydrated nanolayer characterization [29,67,131,271]. Another interesting venture is the

combination of GCI with spectroscopic ellipsometry (GCI-SE) in one instrument, which may offer the simultaneous exploitation of the high sensitivity provided by GCI and the spectroscopic capabilities of SE, allowing complex multilayer structures to be analyzed in detail [278]. SE-SPR is a (i) type combination realizing the generation of surface plasmons and simultaneous SE measurement in the proper configuration [279–283]. Whether the data are obtained from (i) or (ii), the post-measurement combination of QCM and optical data are present complex data analysis challenges. Several comprehensive studies have already combined data obtained from separate SPR-QCM [104,107, 112,284–286], SE-QCM [107,270], OWLS-QCM [29,67,131,271], DPI-QCM [91,287,288] as well as RWG-OWLS [129,289] experiments. Currently available combinations of lable-free techniques focusing on optical methods and QCM are summarized in Fig. 16 and Table 2.

Of note, our recent work explored the possibility to calibrate the label-free optical biosensor signals with direct adhesion-force measuring technologies [162]. Such combinations will open up novel directions in adhesion research and could deepen our understanding in terms of structure-kinetic relations.

5.2. Chain conformation

OWLS is uniquely sensitive to the orientation of molecules in the adsorbed layer, owing to the fact that both TE and TM polarizations of the excited modes propagate in the waveguide layer. The field intensity of TE and TM waves oscillate in planes perpendicular to each other, thus they are differently sensitive to oriented molecules on the surface [264, 296 (see Fig. 17). An adlayer consisting of oriented molecules (ordered structure) is optically anisotropic, manifesting optical birefringence (or double reflection). In general, the RI of a birefringent layer can be
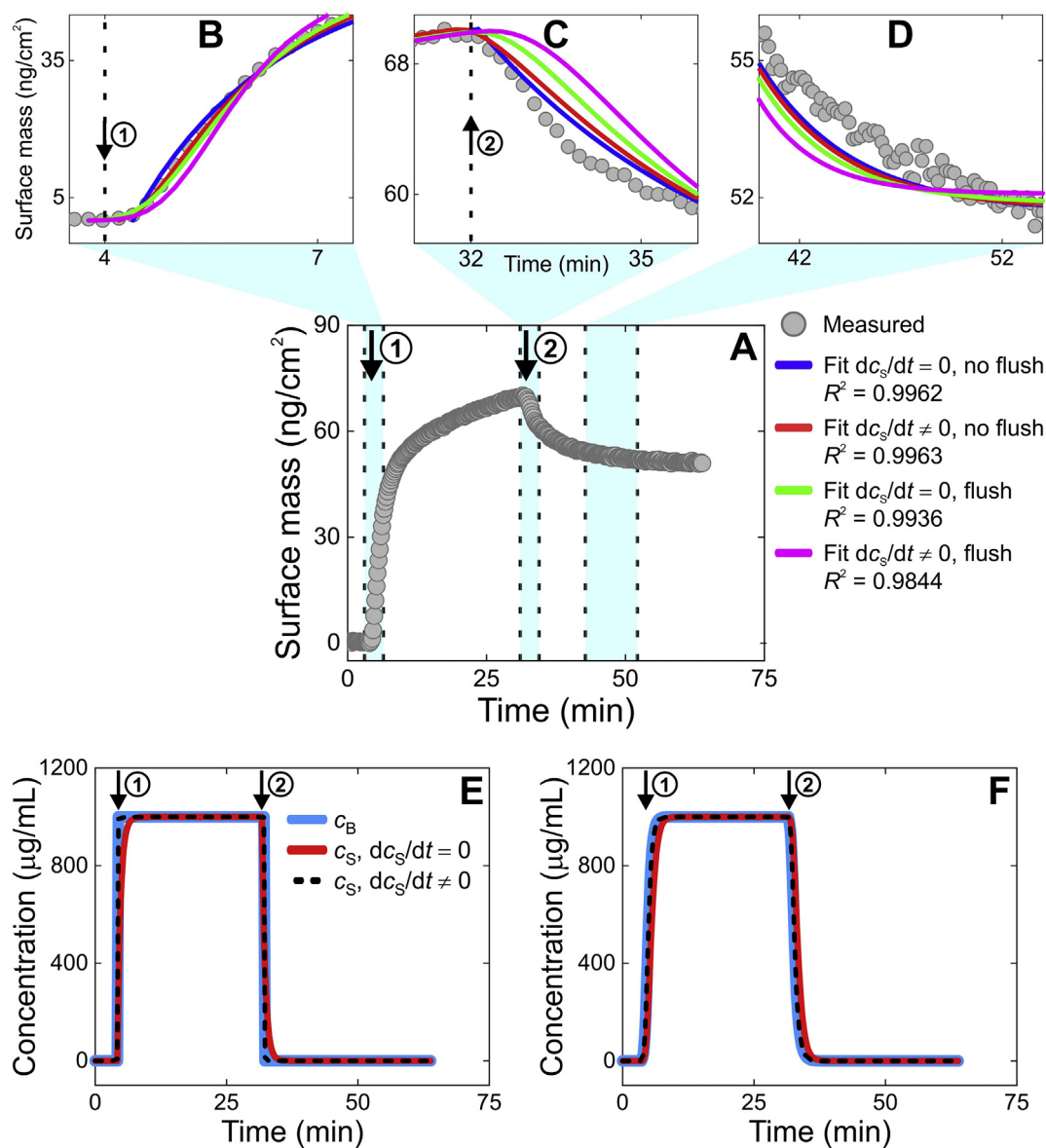
Fig. 13. Influence of different approaches in the implementation of c_S and c_B considering explicit time–dependence of c_S ($dc_S/dt \neq 0$) and the flush effect ($c_B(t)$ is not a step function, instead is described by a logistic equation) in the model. The regions of the fitted mass curve (A) being most sensitive to the model conditions are highlighted in graph B–D. Graph E and F represent the change of concentration over the examined time interval (E. no flush; F. flush). The other model conditions are the same as listed in Fig. 8 caption; experiment: FliC adsorption in presence of NaClO₄.

decomposed into ordinary ($n_{A,o}$) and extraordinary ($n_{A,e}$) RIs and the sign of birefringence is defined by the relative values of $n_{A,o}$ and $n_{A,e}$. Although the usually measured two waveguide modes do not allow the simultaneous determination of all the three optogeometrical parameters (d_A, $n_{A,o}$, $n_{A,e}$), the quasi-homogeneous adlayer RI $\tilde{n}_A$

calculated by the 4–layer homogeneous and isotropic mode equations can indicate the presence and extent of birefringence [297]. Alternatively, d_A should be independently measured, e.g. by X-ray diffraction [80]. Only a few techniques (e.g., polarized visible attenuated total reflection spectroscopy [290]) have the capability of measuring $n_{A,o}$ and

Table 1
Dependence of fitted kinetic data on different hydrodynamic conditions. For further details of fits, see Fig. 13.

	k_a (cm s⁻¹)	k_d (s⁻¹)	k_i (cm s⁻¹)	a_r (nm²)	a_i (nm²)	R^2
$dc_S/dt = 0$, flush	1.16×10^{-6}	5.97×10^{-3}	1.97×10^{-7}	45.1	39.7	0.9844
$dc_S/dt = 0$, no flush	5.08×10^{-7}	3.96×10^{-3}	1.35×10^{-7}	36.4	38.2	0.9963
$dc_S/dt \neq 0$, flush	5.88×10^{-7}	4.56×10^{-3}	1.34×10^{-7}	35.7	38.3	0.9936
$dc_S/dt \neq 0$, no flush	3.69×10^{-7}	3.67×10^{-3}	1.07×10^{-7}	28.6	37.9	0.9962
Average	6.56×10^{-7}	4.54×10^{-3}	1.43×10^{-7}	36.4	38.5	
Coefficient of variation	0.46	0.20	0.23	0.16	0.02	
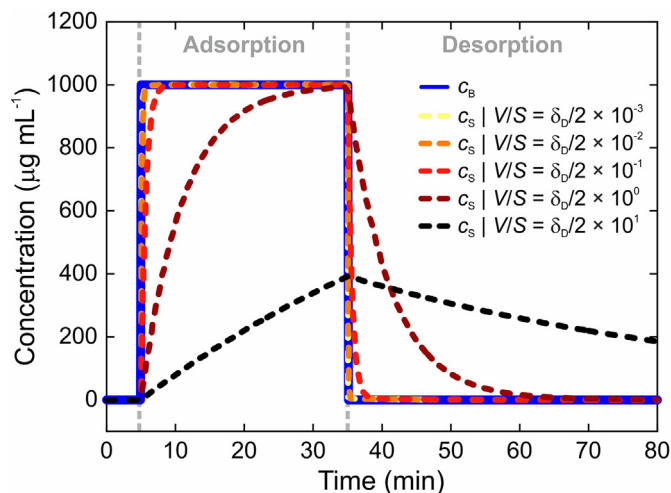
Fig. 14. Variation in c_S if a range of different V/S values are used in the equation describing dc_S/dt. V/S represents the thickness of the surface vicinal layer (δ_S), and its values were chosen relative to the DBL thickness δ_D which is known can be calculated from the known experimental conditions (see Section 3.5.2).

$n_{A,e}$ simultaneously. If one measures a thin adlayer made of molecules with predominantly parallel orientation with the surface, an overestimated $\tilde{n}_A$ is observed; for an adlayer consisting of molecules having their conformation predominantly perpendicular to the surface, an underestimated $\tilde{n}_A$ is observed. As a result, the magnitude of $\tilde{n}_A$ is an indication of the type of optical anisotropy and thus the adlayer nanostructure (see Fig. 18.) [264,296]. Employing the quasi-isotropic thin adlayer model one can obtain unrealistic $\tilde{n}_A$ and d_A values for adlayers partially covering the surface of the OWLS sensor, and for thicker adlayers with homogeneous or decaying RI profiles perpendicular to the surface. It was shown using model calculations that in these cases $\tilde{n}_A$ is always underestimated [302,302. (Considering the bulk RI of protein/biopolymer solutions, a reasonable range for the averaged RI of
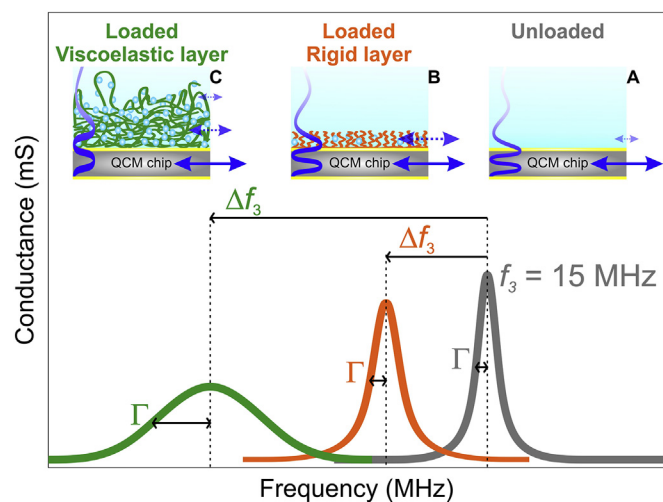
Fig. 15. Principle of QCM sensitivity to adlayer structure. The inset drawings on the top correspond to the bottom resonance curves and represent QCM chips in different conditions. See the colors for matching the drawings and curves. Inset image A represents an unloaded QCM chip, where only a thin part of the bulk solution oscillates together with the crystal. The shear wave generated by the chip oscillation is also shown. B. If the QCM chip is loaded by a thin and rigid adlayer with a low water content, the decay of the penetrating shear wave is similar to the unloaded case, only a frequency shift is detected, but Γ is almost unchanged. C. In case of a thick, viscoelastic adlayer potentially possessing a large water content, the layer does not oscillate perfectly together with the crystal resulting in an increase in dissipation and thus a marked widening in Γ.
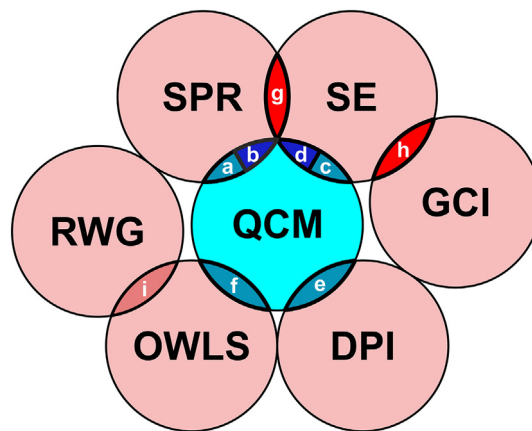
Fig. 16. Combination of label-free methods with focus on optical biosensors and QCM. Combined methods are represented by intersections with hue associated with the mode of combination (listed in Table 2 as (i)-(iii) in the related paragraph). See references of each available combination in Table 2.

compact layers is around 1.40–1.45. For example, n_A above 2.0 is truly unrealistic and a clear indication of optical anisotropy in the assembled layer.)

Once M is calculated, the NBS-OWLSanalysis software plots the $\tilde{n}_A$ vs. M curve, which time-implicitly shows the change in $\tilde{n}_A$ as a result of each unit of mass added to the surface (see Fig. 17), potentially indicating structural hysteresis [299]. As $\tilde{n}_A$ is sensitive to optical anisotropy in the adlayer, the observed deviation in $\tilde{n}_A$ compared to the expected value suggests the sign and magnitude of adlayer birefringence.

5.3. Complex structural and kinetic analysis with the combination of OWLS-QCM data

It has become a common strategy that an adlayer is examined both by an optical technique, such as SPR or OWLS, and by QCM (characterization of biomolecule adsorption and interactions [108,131,291] and living cell adhesion [292,293]) and the obtained data analyzed together. Fig. 18 outlines the workflow that can be applied when QCM and OWLS data are both available. Such analysis is especially relevant in case of nanolayers with high water content and ordered structure. The combination of QCM (whence hydrated mass, viscoelasticity) and OWLS (whence dry mass, optical anisotropy) data enables complex kinetic-structural analysis revealing conformational and hydration–related rearrangements of (bio)polymer chains. Further details of such evaluation can be found in Saftics et al. [29]. It should be emphasized that this type of analysis requires the adlayer under investigation to be formed on the same type of surface; i.e., with the same surface chemistry on both the OWLS and QCM sensing surfaces.

Table 2
Combination of label-free methods presented in Fig. 16.

Method	Intersection	Combination	References
SPR-QCM	a	Instrument (i)	[273]
	b	Data (iii)	[104,107,112,284–286]
SE-QCM	c	Instrument (i)	[106,274–276]
	d	Data (iii)	[107,270]
DPI-QCM	e	Data (iii)	[91,287,288]
OWLS-QCM	f	Instrument/data (ii-iii)*	[67,131,271,29]
SE-SPR	g	Instrument (i)	[279–283]
GCI-SE	h	Instrument (i)	[278]
RWG-OWLS	i	Data (iii)	[129,289]

* The two instruments are combined in a single fluidic line, but the sensing interfaces are not combined in the 2 in 1 instrument available from MicroVacuum Ltd.
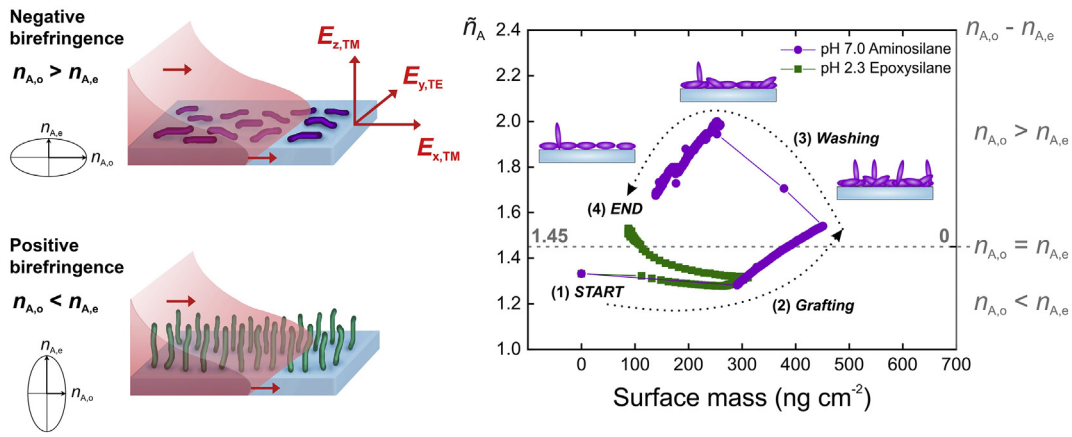
Fig. 17. Principle of OWLS sensitivity to adlayer structure and its exploitation in obtaining structural information. Two distinctive situations are shown: negative birefringence is produced by polymer chains lying down whereas positive birefringence is produced by end-grafted chains only. The refractive index ellipsoids (left) demonstrates the relative magnitude of $n_{A,o}$ and $n_{A,e}$ in the case of the two adlayer structures. The drawings highlight both the adlayer structures and the orientational sensitivity of the TE and TM waveguide modes by indicating the electric field directions of the sensing modes. The data shown in the $\tilde{n}_A$ vs. M graph represents the formation of carboxymethyl dextran (CMD) layer grafted to OWLS chip surface using different surface chemistries as indicated in the legend. The expected realistic RI value of CMD ($n_A = 1.45$) given on the $\tilde{n}_A$ axis can be used as a reference point on the right birefringence axis. The direction of the experiment in time and the separate experimental phases are indicated by the arrows and numbers. While using aminosilane-modified surface at pH 7.0 resulted in mostly side-on grafting of the CMD chains, on epoxysilane-modified surface at pH 2.3 the end-on grafting dominated over a considerable part of the grafting process. However, at the end of the experiment, the orientation of molecules was found to be rather side-on. [The data were adapted from Ref. [30], copyright 2016 Elsevier]

6. Introduction to software packages developed for label-free biosensor data analysis

We publish three software packages along with this paper: (i) *NBS-OWLSanalysis* and (ii) *NBS-QCManalysis* that allows for the evaluation of OWLS and QCM measurement data, respectively; and (iii) *NBS-Kinetics*, which provides a kinetic analysis platform for evaluating any biosensor kinetic data, especially for characterizing adsorption kinetics. All the programs were developed in MATLAB environment (The MathWorks,

Inc., Natick, MA, USA [304]). They have a graphical user interface (GUI) where the different analysis steps are separated in tab–based structure. The programs can be used both to load the measurement data, prepare them for the specific analysis (baseline- and offset-corrections), perform the evaluation based on the corresponding optical, mechanical or binding kinetic model, and finally to visualize and save data. Fig. 19 presents an overview about the GUI of the three programs. Further details about the software packages including a summary of main features and hints of some specific functions can be
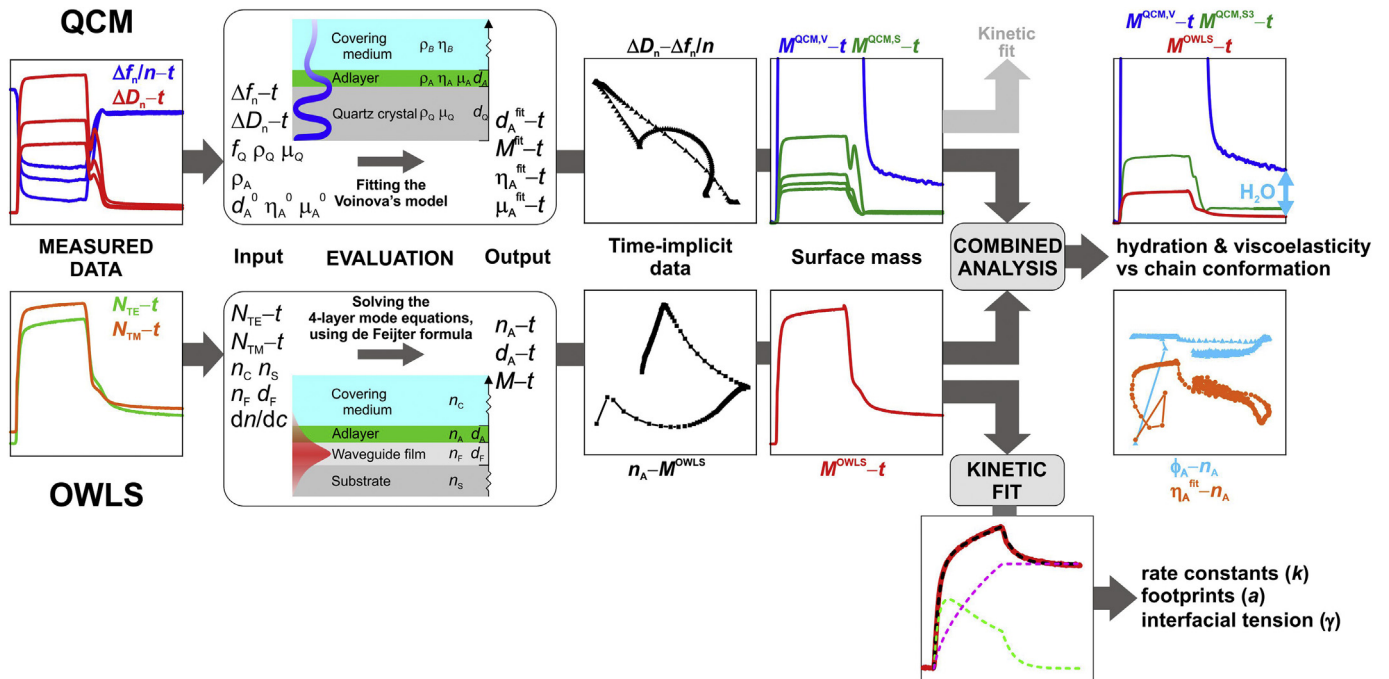
Fig. 18. Workflow for complex data analysis to reveal the dynamics of structural changes in a thick, hydrated adlayer based on combination of QCM and OWLS measurement data. The figure directs through the key stages of data analysis starting with the measured kinetic data. The second stage demonstrates the model applied for evaluating the listed input data with providing the resulted important outputs which are then further analyzed. These analysis stages involve both simple data visualization strategies (combined analysis) and fitting of kinetic models (kinetic fit). The complex data post-processing and analysis emphasize that the quantities obtained in the first evaluation round offer deeper insight into the structure and dynamic behavior of hydrated nanolayers. [The figure contains measurement data adapted from Ref. [29] copyright 2016 Springer Nature used under CC BY]
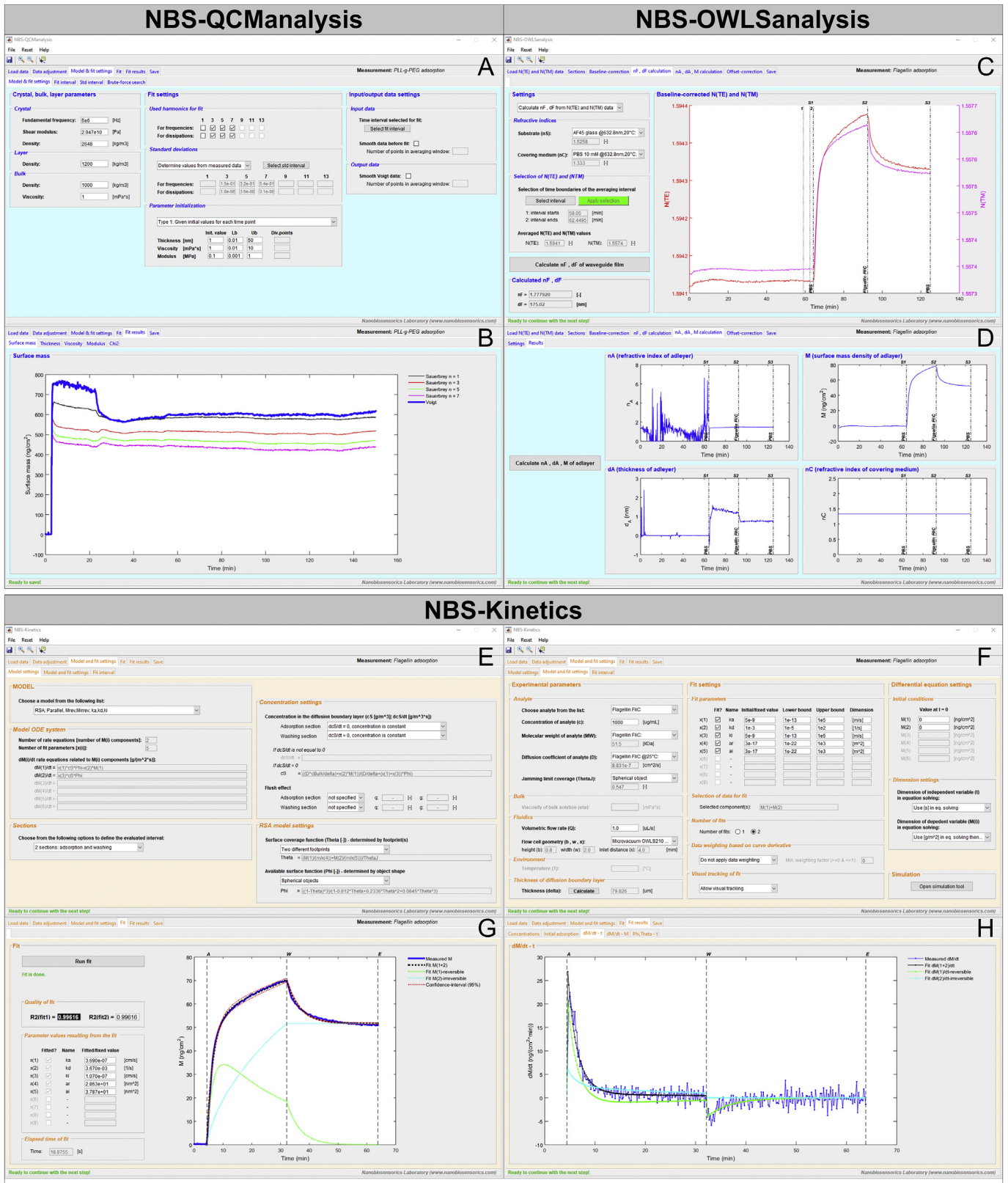
Fig. 19. Overview on the GUI of the NBS software packages developed in MATLAB (The MathWorks, Inc.). Of note, the figure does not completely cover all software features. A–B. Model settings and resulted data from fitting the measured frequency and dissipation data in the *NBS-QCManalysis* software. C–D. Calculation of n_F, d_F as well as n_A, d_A and M data from the recorded N_{TE} and N_{TM} signal in *NBS-OWLSanalysis*. E–H. Model settings, kinetic fit, and resulted data in the *NBS-Kinetics* software.

found in the Supporting Information file. Note: the software is under continuous development and improvements may be provided in later versions.

7. Summary

In this study, we have presented an extensive review on label-free biosensor techniques capable of revealing the nanostructure and formation kinetics of nanolayers with especial relevance for biomedical research. Our principal intention was to demonstrate the variety of available label-free methods, whose ongoing development and expanding field enables one to study fast and complex interfacial biophysicochemical phenomena on the nanoscale with unprecedented throughput and sensitivity. The fundamentally different measurement principles provide broad insight, obtaining both the optical and mechanical characteristics of interfacial layers, determining their mass and thickness as well as deducing their nanostructure and dynamic alterations. Exceptional measurement data can be obtained if the combination of such methods can be established, making it possible to resolve the structure and formation kinetics of ultrathin layers in aqueous conditions. The combination of OWLS (or DPI) and QCM data is especially powerful as it allows for the simultaneous determination of chain orientation and hydration degree through detecting anisotropy as well as dry and hydrated mass. The kinetics of adsorption processes on the solid/liquid interface has great importance, e.g. in drug discovery or in the development of biofunctional and antifouling coatings for biosensors.

With particular focus on hydrodynamic conditions and the mass transport limitation problem, we discussed the experimental and theoretical considerations that should be addressed when kinetic data are fitted. Starting from the PDE model, we devised the widely used two-compartment model in detail. To provide representative examples, we presented kinetic curves simulated with our developed kinetic analysis tool. Taking advantage from these simulations, we showed how the kinetic curves depend on variations in parameters (kinetic rate constants, footprints, concentration, flow rate) involved in the model equations. We demonstrated that using the two-compartment model with modeling surface vicinal concentration differently, even at exceptional fit quality, small discrepancies in the fit may result in relatively large variations in the fitted data.

As a significant addition to this review, we introduced our software packages developed for the evaluation of OWLS and QCM measurement data and for kinetic analysis, providing useful analysis tools for the scientific community.

Software availability

The MATLAB-based software packages presented in this review are available upon request at the email address of robert.horvath "at" energia.mta.hu or r74horvath "at" gmail.com. The software packages will also be made available on the website of the Nanobiosensorics Laboratory (www.nanobiosensorics.com).

Declaration of Competing Interest

None.

Acknowledgements

Appendix A. *Nomenclature*
Abbreviations and Symbols

BAW	bulk acoustic wave
BIA	biointeraction analysis
BLI	bio-layer interferometry
BSA	bovine serum albumin
DBL	diffusion boundary layer
DPI	dual polarization interferometry
EM	electromagnetic
GCI	grating coupled interferometry
HTS	high-throughput screening
MW	molecular weight
ODE	ordinary differential equation
PDE	partial differential equation
OWLS	optical waveguide lightmode spectroscopy
QCM	quartz crystal microbalance
RI	refractive index
RIU	refractive index unit
RSA	random sequential adsorption
RWG	resonant waveguide grating
RU	resonance unit
SPR	surface plasmon resonance
TE	transverse electric mode of guided light
TIRF	Total internal reflection fluorescence
TM	transverse magnetic mode of guided light
t	time [s]
x, y, z	Cartesian coordinates [μm]
P	adsorbing species (adsorptive), e.g. a protein molecule
S^*	surface binding site
A	adsorbed species (adsorbate)
Θ	fractional coverage
Θ_j	jamming limit
Φ	fraction of available surface area (available surface function)
m	mass of one molecule (or adsorbing species) [ng]
ν	number per unit area [cm^{-2}]
ν_{max}	number per unit area at 100% coverage [cm^{-2}]
M	mass per unit area or surface mass density [ng cm^{-2}]
M_{max}	surface mass density at 100% coverage [ng cm^{-2}]
M_r, M_i	reversibly and irreversibly adsorbed surface mass density [ng cm^{-2}]
R	biosensor response [a.u.] or [RU]
R_{max}	biosensor response at 100% coverage [a.u.] or [RU]
N_{Av}	Avogadro number [mol^{-1}]
a_r, a_i	footprint of reversibly and irreversibly adsorbed analyte [nm^2]
s	diameter of a spherical adsorbate [nm]
$k_a = k_{a,mass}$	adsorption/association rate constant of reversibly adsorbed analytes, referred to mass–based (M) surface concentration [cm s^{-1}]
$k_{a,num}$	k_a referred to number–based (ν) surface concentration [cm^{-1} s^{-1}]
$k_{a,resp}$	k_a referred to response–based (R) surface concentration [M^{-1} s^{-1}]
k_d	desorption/dissociation rate constant of reversibly adsorbed analytes [s^{-1}]
$k_{a1,resp}, k_{a2,resp}$	adsorption rate constant [M^{-1} s^{-1}], [s^{-1}]
$k_{d1,resp}, k_{d2,resp}$	adsorption rate constant [s^{-1}], [s^{-1}]
k_i	adsorption rate constant of irreversibly adsorbed analytes [s^{-1}]
k_m	mass transfer coefficient [cm s^{-1}]
$<k_m>$	average mass transfer coefficient over the full length of the channel [cm s^{-1}]
k_f	forward rate constant [cm s^{-1}]
k_r	reverse rate constant [s^{-1}]
j_R	reaction/adsorption flux density [μg m^{-2} s^{-1}]
j_M	mass flux density of analyte towards the surface [μg m^{-2} s^{-1}]
u_{max}, u_{mean}	maximal and mean linear flow rate [m s^{-1}]
Q	volumetric flow rate [μL s^{-1}]
T	absolute temperature [K]
δ_D	thickness of diffusion boundary layer [μm]
δ_S	thickness of surface vicinal region [nm]
D	bulk diffusion coefficient of analyte in solution [cm^2 s^{-1}]
$c_{B,num}$	number concentration of solution in bulk phase [mL^{-1}]
$c_B = c_{B,mass}$	mass concentration of solution in bulk phase [μg mL^{-1}]
c_A	mass concentration of adlayer [μg mL^{-1}]
c_S	mass concentration of analyte solution in the close vicinity of the surface [μg mL^{-1}]
c_D	average mass concentration of analyte solution in the diffusion boundary layer [μg mL^{-1}]

c_{inj}	mass concentration of injected analyte solution [μg mL^{-1}]
S	unit area [μm^2]
V	unit volume [μm^3]
b, h, w, l, r, x	flow cell geometry: full height, half height, width, length, radius, and inlet distance [mm]
Pe	Péclet number
Re	Reynolds number
Y_0, Y_{max}	initial and maximal value of measured data for logistic fit
q, g	fit parameters in logistic equation
σ	field decay length (penetration depth) [nm]
α_{TE}, α_{TM}	incoupling angle for TE and TM modes [deg]
N_{TE}, N_{TM}	effective refractive index of TE and TM modes
Δn	refractive index shift
n_0, n_S, n_F, n_A	refractive index of air, substrate, waveguide film and adlayer
$\tilde{n}_A$	quasi-homogeneous adlayer refractive index calculated from the 4–layer homogeneous and isotropic mode equation
$n_{A,o}, n_{A,e}$	ordinary and extraordinary refractive index of adlayer
n_B	refractive index of bulk solution
n_{medium}	refractive index of medium
dn/dc	refractive index increment of solution [mL g^{-1}]
d_A	thickness of adlayer [nm]
d_A	quasi-homogeneous adlayer thickness calculated from the 4–layer homogeneous and isotropic mode equation [nm]
n	overtone number
ω_n	angular frequency at overtone n [Hz]
$f_n, \Delta f_n$	resonance frequency and its shift at overtone n [Hz]
$D_n, \Delta D_n$	dissipation and its shift at overtone n
τ_n	oscillation decay time at overtone n [ms]
$U_{dissipated}, U_{stored}$	energy dissipated in one oscillation cycle and energy stored in the oscillating system [J]
Γ_n	half-width at half maximum at overtone n [Hz]
C	mass sensitivity constant [ng cm^{-1} Hz^{-1}]
η_A, η_B	viscosity of adlayer and bulk solution [Pa s]
μ_A	shear elastic modulus of adlayer [MPa]
ρ_A, ρ_B, ρ_Q	mass density of adlayer, bulk and quartz crystal [kg m^{-3}]
$\rho_{analyte}, \rho_{solvent}$	mass density of analyte molecules and solvent [kg m^{-3}]
d_Q	thickness of quartz crystal [μm]
G^*	complex shear modulus [MPa]
G', G''	storage and loss shear modulus [MPa]
$std_{\Delta fnm}, std_{\Delta Dnm}$	standard deviation of measured frequency shift [Hz] and dissipation data
χ^2	error function
$E_{x,TM}, E_{y,TE}, E_{z,TM}$	electric field strength of TE and TM modes in different directions [J C^{-1} m^{-1}]
H_A	hydration degree
U_{act}	activation energy [J]
ΔG_a	total Gibbs free energy change characterizing the adsorption process [J]
$\Delta G_{PW}, \Delta G_{SW}, \Delta G_{PS}$	Gibbs free energy change at protein–water, substrate–water and protein–substrate interface [J]
$\gamma_{PW}, \gamma_{SW}, \gamma_{PS}$	protein–water, substrate–water and protein–substrate interfacial tension [mN m^{-1}]
γ_{PWS}	protein–water-substrate interfacial tension [mN m^{-1}]
k_B	Boltzmann constant [m^2 kg s^{-2} K^{-1}]
F	frequency factor with dimension of e.g. [cm s^{-1}]
$\Delta\varphi$	phase shift
λ	wavelength [nm]
λ_R	resonant wavelength [nm]

Appendix B. Supplementary data

Supplementary data to this article can be found online at https://doi.org/10.1016/j.cis.2021.102431.

References

[1] Liu S. Bioprocess engineering: kinetics, sustainability, and reactor design. 3rd ed.. Amsterdam: Elsevier; 2020. https://doi.org/10.1016/C2019-0-02589-7.

[2] Schmidt DR, Waldeck H, Kao WJ. Biological interactions on materials surfaces. Springer US: New York, NY; 2009. https://doi.org/10.1007/978-0-387-98161-1.

[3] Simavilla DN, Huang W, Vandestrick P, Ryckaert J-P, Sferrazza M, Napolitano S. Mechanisms of polymer adsorption onto solid substrates. ACS Macro Lett. 2017; 6:975–9. https://doi.org/10.1021/acsmacrolett.7b00473.

[4] Ramsden JJ, Máté M. Kinetics of monolayer particle deposition. J Chem Soc Faraday Trans. 1998;94:783–8. https://doi.org/10.1039/a708384j.

[5] Cacace MG, Ramsden JJ. In situ monitoring of adsorbed enzyme activity. J Biol Phys Chem. 2007;7:65–8. https://doi.org/10.4024/20705.jbpc.07.02.

[6] Zhou F, editor. Antifouling surfaces and materials. Berlin, Heidelberg: Springer Berlin Heidelberg; 2015. https://doi.org/10.1007/978-3-662-45204-2.

[7] Sabaté del Río J, Henry OYF, Jolly P, Ingber DE. An antifouling coating that enables affinity–based electrochemical biosensing in complex biological fluids. Nat Nanotechnol. 2019;14:1143–9. https://doi.org/10.1038/s41565-019-0566-z.

[8] Malmsten M, editor. Biopolymers at interfaces. 2nd ed. New York, NY: CRC Press; 2003.

[9] de Araújo GRS, Viana NB, Gómez F, Pontes B, Frases S. The mechanical properties of microbial surfaces and biofilms. Cell Surf. 2019;5:100028. https://doi.org/10.1016/j.tcsw.2019.100028.

[10] Saftics A, Türk B, Sulyok A, Nagy N, Gerecsei T, Szekacs I, et al. Biomimetic dextran–based hydrogel layers for cell micropatterning over large areas using the FluidFM BOT technology. Langmuir. 2019;35:2412–21. https://doi.org/10.1021/acs.langmuir.8b03249.

[11] Constable EC, Harverson P, Ramsden JJ. Adsorption of ruthenadendrimers to silica–titania surfaces studied by optical waveguide lightmode spectroscopy (OWLS). Chem Commun. 1997:1683–4. https://doi.org/10.1039/a704638c.

[12] Hochella MF, White AF, editors. Mineral-water interface geochemistry. De Gruyter; 1990. https://doi.org/10.1515/9781501509131.

[13] Ramsden JJ. A sum parameter sensor for water quality. Water Res. 1999;33: 1147–50. https://doi.org/10.1016/S0043-1354(98)00317-0.

[14] Influence of adsorption on electrochemical properties. In: Bénard J, Berthier Y, Delarnare F, Hondros E, Huber M, Marcus P, et al, editors. Stud. surf. sci. catal. Elsevier; 1983. p. 211–44. https://doi.org/10.1016/S0167-2991(08)64969-1.

[15] Maurice V, Marcus P. Application of surface science to corrosion. Surf. interface sci. Wiley; 2020; 799–825. https://doi.org/10.1002/9783527822508.ch78.

[16] Che M, Védrine JC, editors. Characterization of solid materials and heterogeneous catalysts. Weinheim, Germany: Wiley-VCH Verlag GmbH & Co. KGaA; 2012. https://doi.org/10.1002/9783527645329.

[17] Szekacs I, Farkas E, Gemes BL, Takacs E, Szekacs A, Horvath R. Integrin targeting of glyphosate and its cell adhesion modulation effects on osteoblastic MC3T3-E1 cells revealed by label-free optical biosensing. Sci Rep. 2018;8:17401. https://doi.org/10.1038/s41598-018-36081-0.

[18] Goutev N, Nickolov ZS, Ramsden JJ. Waveguide Raman spectroscopy of Si(Ti)O2 thin films with grating coupling. J Raman Spectrosc. 1996;27:897–900. https://doi.org/10.1002/(SICI)1097-4555(199612)27:12<897::AID-JRS49>3.0.CO;2-R.

[19] Marks RS. Handbook of biosensors and biochips. , 2Chichester, UK: John Wiley & Sons, Ltd; 2007. https://doi.org/10.1002/9780470061565.

[20] Kozma P, Hámori A, Kurunczi S, Cottier K, Horvath R. Grating coupled optical waveguide interferometer for label-free biosensing. Sensors Actuators B Chem. 2011; 155:446–50. https://doi.org/10.1016/j.snb.2010.12.045.

[21] Fang Y. Live cell optical sensing for high throughput applications. Whole cell sens. syst. II. Berlin, Heidelberg: Springer Berlin Heidelberg; 2009. p. 153–63. https://doi.org/10.1007/10_2009_4.

[22] Duan X, Li Y, Rajan NK, Routenberg DA, Modis Y, Reed MA. Quantification of the affinities and kinetics of protein interactions using silicon nanowire biosensors. Nat Nanotechnol. 2012;7:401–7. https://doi.org/10.1038/nnano.2012.82.

[23] Ramsden JJ. Biospecific interaction analysis using integrated optics techniques. In: Lundahl P, Lundqvist A, Greijer E, editors. Quant. anal. biospecific interact. Amsterdam: Hardwood Academic Publishers; 1998. p. 149–62.

[24] Farkas E, Szekacs A, Kovacs B, Olah M, Horvath R, Szekacs I. Label-free optical biosensor for real-time monitoring the cytotoxicity of xenobiotics: a proof of principle study on glyphosate. J Hazard Mater. 2018;351:80–9. https://doi.org/10.1016/j.jhazmat.2018.02.045.

[25] Coan KED, Swann MJ, Ottl J. Measurement and differentiation of ligand–induced calmodulin conformations by dual polarization interferometry. Anal Chem. 2012; 84:1586–91. https://doi.org/10.1021/ac202844e.

[26] Squires TM, Messinger RJ, Manalis SR. Making it stick: convection, reaction and diffusion in surface-based biosensors. Nat Biotechnol. 2008;26:417–26. https://doi.org/10.1038/nbt1388.

[27] Orgovan N, Patko D, Hos C, Kurunczi S, Szabó B, Ramsden JJ, et al. Sample handling in surface sensitive chemical and biological sensing: a practical review of basic fluidics and analyte transport. Adv Colloid Interface Sci. 2014;211:1–16. https://doi.org/10.1016/j.cis.2014.03.011.

[28] Migliorini E, Weidenhaupt M, Picart C. Practical guide to characterize biomolecule adsorption on solid surfaces (review). Biointerphases. 2018;13:06D303. https://doi.org/10.1116/1.5045122.

[29] Saftics A, Prósz GA, Türk B, Péter B, Kurunczi S, Horvath R. Viscoelastic properties of heavily hydrated carboxymethyl dextran and PLL-g-PEG layers: a comparative study using OWLS and QCM-I chips coated with waveguide material. Sci Rep. 2018;8:11840. https://doi.org/10.1038/s41598-018-30201-6.

[30] Saftics A, Kurunczi S, Szekrényes Z, Kamarás K, Khánh NQ, Sulyok A, et al. Fabrication and characterization of ultrathin dextran layers: time dependent nanostructure in aqueous environments revealed by OWLS. Colloids Surf B Biointerfaces. 2016;146:861–70. https://doi.org/10.1016/j.colsurfb.2016.06.057.

[31] McColl J, Yakubov GE, Ramsden JJ. Complex desorption of mucin from silica. Langmuir. 2007;23:7096–100. https://doi.org/10.1021/la0630918.

[32] Ramsden JJ. Experimental methods for investigating protein adsorption kinetics at surfaces. Q Rev Biophys. 1994;27:41–105. https://doi.org/10.1017/S0033583500002900.

[33] Nirschl M, Reuter F, Vörös J. Review of transducer principles for label-free biomolecular interaction analysis. Biosensors. 2011;1:70–92. https://doi.org/10.3390/bios1030070.

[34] Fan X, White IM, Shopova SI, Zhu H, Suter JD, Sun Y. Sensitive optical biosensors for unlabeled targets: a review. Anal Chim Acta. 2008;620:8–26. https://doi.org/10.1016/j.aca.2008.05.022.

[35] Lee T-H, Hirst DJ, Aguilar M-I. New insights into the molecular mechanisms of biomembrane structural changes and interactions by optical biosensor technology.

Biochim Biophys Acta. 1848;2015:1868–85. https://doi.org/10.1016/j.bbamem.2015.05.012.

[36] Ramsden JJ. Optical biosensors. J Mol Recognit. 1997;10:109–20. https://doi.org/10.1002/(SICI)1099-1352(199705/06)10:3<109::AID-JMR361>3.0.CO;2-D.

[37] Hall D. Use of optical biosensors for the study of mechanistically concerted surface adsorption processes. Anal Biochem. 2001;288:109–25. https://doi.org/10.1006/abio.2000.4851.

[38] Ismail IM, Gray ND, Owen JR. A QCM analysis of water absorption in lithium polymer electrolytes. J Chem Soc Faraday Trans. 1996;92:4115. https://doi.org/10.1039/ft9969204115.

[39] Marx KA. Quartz crystal microbalance: a useful tool for studying thin polymer films and complex biomolecular systems at the solution−surface interface. Biomacromolecules. 2003;4:1099–120. https://doi.org/10.1021/bm020116i.

[40] Kittle JD, Du X, Jiang F, Qian C, Heinze T, Roman M, et al. Equilibrium water contents of cellulose films determined via solvent exchange and quartz crystal microbalance with dissipation monitoring. Biomacromolecules. 2011;12:2881–7. https://doi.org/10.1021/bm200352q.

[41] Norde W, Rouwendal E. Streaming potential measurements as a tool to study protein adsorption kinetics. J Colloid Interface Sci. 1990;139:169–76. https://doi.org/10.1016/0021-9797(90)90454-V.

[42] Etayash H, Thundat T. Microcantilever chemical and biological sensors. In: Bhushan B, editor. Encycl. nanotechnol. Dordrecht: Springer Netherlands; 2015. p. 1–9. https://doi.org/10.1007/978-94-007-6178-0_187-2.

[43] Yang F, Zhang G-J. Silicon nanowire-transistor biosensor for study of molecule-molecule interactions. Rev Anal Chem. 2014;33:95–110. https://doi.org/10.1515/revac-2014-0010.

[44] Homola J. Surface plasmon resonance sensors for detection of chemical and biological species. Chem Rev. 2008;108:462–93. https://doi.org/10.1021/cr068107d.

[45] Singh P. SPR biosensors: historical perspectives and current challenges. Sensors Actuators B Chem. 2016;229:110–30. https://doi.org/10.1016/j.snb.2016.01.118.

[46] Bocková M, Slabý J, Špringer T, Homola J. Advances in surface plasmon resonance imaging and microscopy and their biological applications. Annu Rev Anal Chem. 2019;12:151–76. https://doi.org/10.1146/annurev-anchem-061318-115106.

[47] Lukosz W. Principles and sensitivities of integrated optical and surface plasmon sensors for direct affinity sensing and immunosensing. Biosens Bioelectron. 1991;6:215–25. https://doi.org/10.1016/0956-5663(91)80006-J.

[48] Cacace MG, Landau EM, Ramsden JJ. The Hofmeister series: salt and solvent effects on interfacial phenomena. Q Rev Biophys. 1997;30:241–77. https://doi.org/10.1017/S0033583597003363.

[49] Schuck P. Kinetics of ligand binding to receptor immobilized in a polymer matrix, as detected with an evanescent wave biosensor. I. A computer simulation of the influence of mass transport. Biophys J. 1996;70:1230–49. https://doi.org/10.1016/S0006-3495(96)79681-9.

[50] Jankovics H, Kovacs B, Andras S, Gerecsei T, Tóth É, Szekacs I, et al. Grating-coupled interferometry reveals binding kinetics and affinities of Ni ions to genetically engineered protein layers. Sci Rep. 2020;10:22253. https://doi.org/10.1038/s41598-020-79226-w.

[51] Day YSN, Baird CL, Rich RL, Myszka DG. Direct comparison of binding equilibrium, thermodynamic, and rate constants determined by surface- and solution-based biophysical methods. Protein Sci. 2002;11:1017–25. https://doi.org/10.1110/ps.4330102.

[52] Rich RL, Day YSN, Morton TA, Myszka DG. High-resolution and high-throughput protocols for measuring drug/human serum albumin interactions using BIACORE. Anal Biochem. 2001;296:197–207 10.1006/abio.2001.5314.

[53] Kanyo N, Kovacs KD, Saftics A, Szekacs I, Peter B, Santa-Maria AR, et al. Glycocalyx regulates the strength and kinetics of cancer cell adhesion: biophysical models based on high resolution label-free optical data. Sci Rep. 2020;10:22422. https://doi.org/10.1038/s41598-020-80033-6.

[54] Market Data Forecast. Surface plasmon resonance market. data based on report of marcetdataforecast.com https://www.marketdataforecast.com/market-reports/surface-plasmon-resonance-market; 2020.

[55] Cytiva. Biacore S200. https://www.cytivalifesciences.com/en/gb/shop/protein-analysis/spr-label-free-analysis/systems/biacore-s200-p-05541; 2021.

[56] Cytiva. Biacore 8K+. https://www.cytivalifesciences.com/en/gb/shop/protein-analysis/spr-label-free-analysis/systems/biacore-8k-p-09826; 2021.

[57] De Feijter JA, Benjamins J, Veer FA. Ellipsometry as a tool to study the adsorption behavior of synthetic and biopolymers at the air-water interface. Biopolymers. 1978;17:1759–72. https://doi.org/10.1002/bip.1978.360170711.

[58] Ball V, Ramsden JJ. Buffer dependence of refractive index increments of protein solutions. Biopolymers. 1998;46:489–92. https://doi.org/10.1002/(SICI)1097-0282(199812)46:7<489::AID-BIP6>3.3.CO;2-5.

[59] Theisen A, Johann C, Deacon MP, Harding SE. Refractive increment data-book: for polymer and biomolecular scientists. Nottingham: Nottingham University Press; 1999.

[60] Székács A, Adányi N, Székács I, Majer-Baranyi K, Szendrő I. Optical waveguide lightmode spectroscopy immunosensors for environmental monitoring. Appl Opt. 2009;48:B151. https://doi.org/10.1364/AO.48.00B151.

[61] Adányi N, Majer-Baranyi K, Berki M, Darvas B, Wang B, Szendrő I, et al. Development of immunosensors based on optical waveguide lightmode spectroscopy (OWLS) technique for determining active substance in herbs. Sensors Actuators B Chem. 2017;239:413–20. https://doi.org/10.1016/j.snb.2016.08.011.

[62] Adányi N, Levkovets IA, Rodriguez-Gil S, Ronald A, Váradi M, Szendro I. Development of immunosensor based on OWLS technique for determining Aflatoxin B1 and Ochratoxin A. Biosens Bioelectron. 2007;22:797–802. https://doi.org/10.1016/j.bios.2006.02.015.

[63] Vörös J, Ramsden J, Csúcs G, Szendrő I, De Paul S, Textor M, et al. Optical grating coupler biosensors. Biomaterials. 2002;23:3699–710. https://doi.org/10.1016/S0142-9612(02)00013-5.

[64] MicroVacuum Ltd. OWLS 210 label-free, real-time biosensor system. https://www.owls-sensors.com/OWLS-System; 2021.

[65] Ball V, Ramsden JJ. Absence of surface exclusion in the first stage of lysozyme adsorption is driven through electrostatic self-assembly. J Phys Chem B. 1997;101:5465–9. https://doi.org/10.1021/jp963812j.

[66] Guemouri L, Ogier J, Ramsden JJ. Optical properties of protein monolayers during assembly. J Chem Phys. 1998;109:3265–8. https://doi.org/10.1063/1.476917.

[67] Vörös J. The density and refractive index of adsorbing protein layers. Biophys J. 2004;87:553–61. https://doi.org/10.1529/biophysj.103.030072.

[68] Kurrat R, Wälivaara B, Marti A, Textor M, Tengvall P, Ramsden JJ, et al. Plasma protein adsorption on titanium: comparative in situ studies using optical waveguide lightmode spectroscopy and ellipsometry. Colloids Surf B Biointerfaces. 1998;11:187–201. https://doi.org/10.1016/S0927-7765(98)00039-3.

[69] Kurunczi S, Horvath R, Yeh Y-P, Muskotál A, Sebestyén A, Vonderviszt F, et al. Self-assembly of rodlike receptors from bulk solution. J Chem Phys. 2009;130:011101. https://doi.org/10.1063/1.3037245.

[70] Kleinjung F, Bier FF, Warsinke A, Scheller FW. Fibre-optic genosensor for specific determination of femtomolar DNA oligomers. Anal Chim Acta. 1997;350:51–8. https://doi.org/10.1016/S0003-2670(97)00192-X.

[71] Bier FF, Scheller FW. Label-free observation of DNA-hybridisation and endonuclease activity on a wave guide surface using a grating coupler. Biosens Bioelectron. 1996;11:669–74. https://doi.org/10.1016/0956-5663(96)83300-8.

[72] Ramsden JJ, Dreier J. Kinetics of the interaction between DNA and the type IC restriction enzyme eco R124II. Biochemistry. 1996;35:3746–53. https://doi.org/10.1021/bi952158f.

[73] Horvath R, Pedersen HC, Cuisinier FJG. Guided wave sensing of polyelectrolyte multilayers. Appl Phys Lett. 2006;88:111102. https://doi.org/10.1063/1.2184756.

[74] Perry SS, Yan X, Limpoco FT, Lee S, Müller M, Spencer ND. Tribological properties of poly(<scp>l</scp>-lysine)- *graft* -poly(ethylene glycol) films: influence of polymer architecture and adsorbed conformation. ACS Appl Mater Interfaces. 2009;1:1224–30. https://doi.org/10.1021/am900101m.

[75] Ramsden JJ, Li S-Y, Prenosil JE, Heinzle E. Kinetics of adhesion and spreading of animal cells. Biotechnol Bioeng. 1994;43:939–45. https://doi.org/10.1002/bit.260431007.

[76] Aref A, Horvath R, Ramsden JJ. Spreading kinetics for quantifying cell state during stem cell differentiation. J Biol Phys Chem. 2010;10:145–51. https://doi.org/10.4024/17AR10A.jbpc.10.04.

[77] Horváth R, Pedersen HC, Skivesen N, Selmeczi D, Larsen NB. Optical waveguide sensor for on-line monitoring of bacteria. Opt Lett. 2003;28:1233. https://doi.org/10.1364/OL.28.001233.

[78] Kovacs B, Patko D, Klein A, Kakasi B, Saftics A, Kurunczi S, et al. Bacteria repellent layer made of flagellin. Sensors Actuators B Chem. 2018;257:839–45. https://doi.org/10.1016/j.snb.2017.11.027.

[79] Csúcs G, Ramsden JJ. Interaction of phospholipid vesicles with smooth metal-oxide surfaces. Biochim Biophys Acta. 1998;1369:61–70. https://doi.org/10.1016/S0005-2736(97)00209-5.

[80] Ramsden JJ. Molecular orientation in lipid bilayers. Philos Mag B. 1999;79:381–6. https://doi.org/10.1080/13642819908206414.

[81] Ramsden JJ. On protein-lipid membrane interactions. Colloids Surfaces B Biointerfaces. 1999;14:77–81. https://doi.org/10.1016/S0927-7765(99)00026-0.

[82] Shanshiashvili L, Suknidze NC, Machaidze G, Mikeladze D, Ramsden JJ. Adhesion and clustering of charge isomers of myelin basic protein at model myelin membranes. Arch Biochem Biophys. 2003;419:170–7. https://doi.org/10.1016/j.abb.2003.09.020.

[83] Michielin O, Vergères G, Ramsden JJ. Myristoylation-induced compaction of a membrane-binding protein. J Am Chem Soc. 1999;121:6523–6. https://doi.org/10.1021/ja990239j.

[84] Cross GH, Reeves AA, Brand S, Popplewell JF, Peel LL, Swann MJ, et al. A new quantitative optical biosensor for protein characterisation. Biosens Bioelectron. 2003;19:383–90. https://doi.org/10.1016/S0956-5663(03)00203-3.

[85] Swann MJ, Peel LL, Carrington S, Freeman NJ. Dual-polarization interferometry: an analytical technique to measure changes in protein structure in real time, to determine the stoichiometry of binding events, and to differentiate between specific and nonspecific interactions. Anal Biochem. 2004;329:190–8. https://doi.org/10.1016/j.ab.2004.02.019.

[86] Freeman N. Dual polarisation interferometry: an optical technique to measure the orientation and structure of proteins at the solid–liquid interface in real time. Proteins at solid–liquid interfaces. Heidelberg: Springer Berlin; 2006; 75–104.

[87] Sanghera N, Swann MJ, Ronan G, Pinheiro TJT. Insight into early events in the aggregation of the prion protein on lipid membranes. Biochim Biophys Acta. 1788; 2009:2245–51. https://doi.org/10.1016/j.bbamem.2009.08.005.

[88] Boudjemline A, Saridakis E, Swann MJ, Govada L, Mavridis IM, Chayen NE. Use of dual polarization interferometry as a diagnostic tool for protein crystallization. Anal Chem. 2011;83:7881–7. https://doi.org/10.1021/ac2017844.

[89] Sörensen MH, Samoshina Y, Claesson PM, Alberius P. Sustained release of ibuprofen from polyelectrolyte encapsulated mesoporous carriers. J Dispers Sci Technol. 2009;30:892–902. https://doi.org/10.1080/01932690802644095.

[90] Ouberai MM, Dos Santos ALG, Kinna S, Madalli S, Hornigold DC, Baker D, et al. Controlling the bioactivity of a peptide hormone in vivo by reversible self-assembly. Nat Commun. 2017;8:1026. https://doi.org/10.1038/s41467-017-01114-1.

[91] Escorihuela J, González-Martínez MÁ, López-Paz JL, Puchades R, Maquieira Á, Gimenez-Romero D. Dual-polarization interferometry: a novel technique to light

up the nanomolecular world. Chem Rev. 2015;115:265–94. https://doi.org/10.1021/cr5002063.

[92] Su Y, Xu H, Chen Y, Qi J, Zhou X, Ge R, et al. Real-time and label-free detection of bisphenol A by an ssDNA aptamer sensor combined with dual polarization interferometry. New J Chem. 2018;42:2850–6. https://doi.org/10.1039/C7NJ05064J.

[93] Coffey PD, Swann MJ, Waigh TA, Schedin F, Lu JR. Multiple path length dual polarization interferometry. Opt Express. 2009;17:10959. https://doi.org/10.1364/OE.17.010959.

[94] Ferreira GNM, Da-Silva A-C, Tomé B. Acoustic wave biosensors: physical models and biological applications of quartz crystal microbalance. Trends Biotechnol. 2009;27:689–97. https://doi.org/10.1016/j.tibtech.2009.09.003.

[95] Johannsmann D. The quartz crystal microbalance in soft matter research. Cham: Springer International Publishing; 2015. https://doi.org/10.1007/978-3-319-07836-6.

[96] Johannsmann D. Viscoelastic, mechanical, and dielectric measurements on complex samples with the quartz crystal microbalance. Phys Chem Chem Phys. 2008; 10:4516. https://doi.org/10.1039/b803960g.

[97] Biolin Scientific AB. QSense QCMD instruments. https://www.biolinscientific.com/qsense/instruments; 2021.

[98] Rodahl M, Höök F, Krozer A, Brzezinski P, Kasemo B. Quartz crystal microbalance setup for frequency and Q - factor measurements in gaseous and liquid environments Quartz crystal microbalance setup for frequency and G !? -factor rneasurements in gaseous and liquid environments. Rev Sci Instrum. 1995;66: 3924–30. https://doi.org/10.1063/1.1145396.

[99] Reviakine I, Johannsmann D, Richter RP. Hearing what you cannot see and visualizing what you hear: interpreting quartz crystal microbalance data from solvated interfaces. Anal Chem. 2011;83:8838–48. https://doi.org/10.1021/ac201778h.

[100] MicroVacuum Ltd. QCM-I quartz crystal microbalance with impedance measurement. https://www.owls-sensors.com/qcm-i-quartz-crystal-microbalance-with-impedance-measurement; 2021.

[101] Sauerbrey G. Verwendung von Schwingquarzen zur Wägung dünner Schichtenund zur Mikrowägung. Z Phys. 1959;155:206–22. https://doi.org/10.1007/BF01337937.

[102] Vogt BD, Lin EK, Wu WI, White CC. Effect of film thickness on the validity of the sauerbrey equation for hydrated polyelectrolyte films. J Phys Chem B. 2004;108: 12685–90. https://doi.org/10.1021/jp0481005.

[103] Dutta AK, Belfort G. Adsorbed gels versus brushes: viscoelastic differences. Langmuir. 2007;23:3088–94. https://doi.org/10.1021/la0624743.

[104] Liu Z, Choi H, Gatenholm P, Esker AR. Quartz crystal microbalance with dissipation monitoring and surface plasmon resonance studies of carboxymethyl cellulose adsorption onto regenerated cellulose surfaces. Langmuir. 2011;27:8718–28. https://doi.org/10.1021/la200628a.

[105] Voinova MV, Rodahl M, Jonson M, Kasemo B. Viscoelastic acoustic response of layered polymer films at fluid-solid interfaces: continuum mechanics approach. Phys Scr. 1999;59:391–6. https://doi.org/10.1238/Physica.Regular.059a00391.

[106] Domack A, Prucker O, Rühe J, Johannsmann D. Swelling of a polymer brush probed with a quartz crystal resonator. Phys Rev E. 1997;56:680–9. https://doi.org/10.1103/PhysRevE.56.680.

[107] Höök F, Kasemo B, Nylander T, Fant C, Sott K, Elwing H. Variations in coupled water, viscoelastic properties, and film thickness of a Mefp-1 protein film during adsorption and cross-linking: a quartz crystal microbalance with dissipation monitoring, ellipsometry, and surface plasmon resonance study. Anal Chem. 2001;73: 5796–804. https://doi.org/10.1021/ac0106501.

[108] Stengel G, Höök F, Knoll W. Viscoelastic modeling of template-directed DNA synthesis. Anal Chem. 2005;77:3709–14. https://doi.org/10.1021/ac048302x.

[109] Irwin EF, Ho JE, Kane SR, Healy KE. Analysis of interpenetrating polymer networks via quartz crystal microbalance with dissipation monitoring. Langmuir. 2005;21: 5529–36. https://doi.org/10.1021/la0470737.

[110] Tammelin T, Merta J, Johansson L-S, Stenius P. Viscoelastic properties of cationic starch adsorbed on quartz studied by QCM-D. Langmuir. 2004;20:10900–9. https://doi.org/10.1021/la0487693.

[111] Yi P, Chen KL. Release kinetics of multiwalled carbon nanotubes deposited on silica surfaces: quartz crystal microbalance with dissipation (QCM-D) measurements and modeling. Environ Sci Technol. 2014;48:4406–13. https://doi.org/10.1021/es405471u.

[112] Larsson C, Rodahl M, Höök F. Characterization of DNA immobilization and subsequent hybridization on a 2D arrangement of streptavidin on a biotin-modified lipid bilayer supported on SiO2. Anal Chem. 2003;75:5080–7. https://doi.org/10.1021/ac034269n.

[113] Hovgaard MB, Dong M, Otzen DE, Besenbacher F. Quartz crystal microbalance studies of multilayer glucagon fibrillation at the solid-liquid interface. Biophys J. 2007; 93:2162–9. https://doi.org/10.1529/biophysj.107.109686.

[114] Johannsmann D. QTM software. QCM model. https://www.pc.tu-clausthal.de/en/research/qcm-modelling/; 2021.

[115] Martin EJ, Mathew MT, Shull KR. Viscoelastic properties of electrochemically deposited protein/metal complexes. Langmuir. 2015;31:4008–17. https://doi.org/10.1021/acs.langmuir.5b00169.

[116] Sadman K, Wiener CG, Weiss RA, White CC, Shull KR, Vogt BD. Quantitative rheometry of thin soft materials using the quartz crystal microbalance with dissipation. Anal Chem. 2018;90:4079–88. https://doi.org/10.1021/acs.analchem.7b05423.

[117] DeNolf GC, Sturdy LF, Shull KR. High-frequency rheological characterization of homogeneous polymer films with the quartz crystal microbalance. Langmuir. 2014; 30:9781–40. https://doi.org/10.1021/la502090a.

[118] Delgado DE, Sturdy LF, Burkhart CW, Shull KR. Validation of quartz crystal rheometry in the megahertz frequency regime. J Polym Sci Part B Polym Phys. 2019;57:1246–54. https://doi.org/10.1002/polb.24812.

[119] Zhang M, Wiener CG, Sepulveda-Medina PI, Douglas JF, Vogt BD. Influence of sodium salts on the swelling and rheology of hydrophobically cross-linked hydrogels determined by QCM-D. Langmuir. 2019;35:16612–23. https://doi.org/10.1021/acs.langmuir.9b03063.

[120] Sun L, Svedhem S, Åkerman B. Construction and modeling of concatemeric dna multilayers on a planar surface as monitored by QCM-D and SPR. Langmuir. 2014;30:8432–41. https://doi.org/10.1021/la500716d.

[121] Munro JC, Frank CW. Polyacrylamide adsorption from aqueous solutions on gold and silver surfaces monitored by the quartz crystal microbalance. Macromolecules. 2004;37:925–38. https://doi.org/10.1021/ma030297w.

[122] Hillman AR, Jackson A, Martin SJ. The problem of uniqueness of fit for viscoelastic films on thickness-shear mode resonator surfaces. Anal Chem. 2001;73:540–9. https://doi.org/10.1021/ac001065n.

[123] Strasser J, de Jong RN, Beurskens FJ, Schuurman J, Parren PWHI, Hinterdorfer P, et al. Weak fragment crystallizable (Fc) domain interactions drive the dynamic assembly of IgG oligomers upon antigen recognition. ACS Nano. 2020;14:2739–50. https://doi.org/10.1021/acsnano.9b08347.

[124] Yazawa K, Furusawa H. Probing multiple binding modes of DNA hybridization: a comparison between single-molecule observations and ensemble measurements; 2018. https://doi.org/10.1021/acsomega.8b00135.

[125] Li X, Song S, Shuai Q, Pei Y, Aastrup T, Pei Y, et al. Real-time and label-free analysis of binding thermodynamics of carbohydrate-protein interactions on unfixed cancer cell surfaces using a QCM biosensor. Sci Rep. 2015;5:14066. https://doi.org/10.1038/srep14066.

[126] Wu C, Li X, Song S, Pei Y, Guo L, Pei Z. QCM biosensor based on polydopamine surface for real-time analysis of the binding kinetics of protein-protein interactions. Polymers (Basel). 2017;9:482. https://doi.org/10.3390/polym9100482.

[127] Dubiel EA, Martin B, Vigier S, Vermette P. Real-time label-free detection and kinetic analysis of Etanercept—Protein A interactions using quartz crystal microbalance. Colloids Surfaces B Biointerfaces. 2017;149:312–21. https://doi.org/10.1016/j.colsurfb.2016.10.036.

[128] Biolin Scientific AB. QSense Pro. https://www.biolinscientific.com/qsense/instruments/qsense-pro; 2021.

[129] Orgovan N, Kovacs B, Farkas E, Szabó B, Zaytseva N, Fang Y, et al. Bulk and surface sensitivity of a resonant waveguide grating imager. Appl Phys Lett. 2014; 104:083506. https://doi.org/10.1063/1.4866460.

[130] Orgovan N, Peter B, Bősze S, Ramsden JJ, Szabó B, Horvath R. Dependence of cancer cell adhesion kinetics on integrin ligand surface density measured by a high-throughput label-free resonant waveguide grating biosensor. Sci Rep. 2015;4: 4034. https://doi.org/10.1038/srep04034.

[131] Höök F, Vörös J, Rodahl M, Kurrat R, Böni P, Ramsden J, et al. A comparative study of protein adsorption on titanium oxide surfaces using in situ ellipsometry, optical waveguide lightmode spectroscopy, and quartz crystal microbalance/dissipation. Colloids Surfaces B Biointerfaces. 2002;24:155–70. https://doi.org/10.1016/S0927-7765(01)00236-3.

[132] Peter B, Saftics A, Kovacs B, Kurunczi S, Horvath R. Oxidization increases the binding of EGCG to serum albumin revealed by kinetic data from label-free optical biosensor with reference channel. Analyst. 2020;145:588–95. https://doi.org/10.1039/C9AN01779H.

[133] Gatterdam V, Frutiger A, Stengele K-P, Heindl D, Lübbers T, Vörös J, et al. Focal molography is a new method for the in situ analysis of molecular interactions in biological samples. Nat Nanotechnol. 2017;12:1089–95. https://doi.org/10.1038/nnano.2017.168.

[134] Frutiger A, Blickenstorfer Y, Bischof S, Forró C, Lauer M, Gatterdam V, et al. Principles for sensitive and robust biomolecular interaction analysis: the limits of detection and resolution of diffraction–limited focal molography. Phys Rev Appl. 2019; 11:014056. https://doi.org/10.1103/PhysRevApplied.11.014056.

[135] Kozma P, Kehl F, Ehrentreich-Förster E, Stamm C, Bier FF. Integrated planar optical waveguide interferometer biosensors: a comparative review. Biosens Bioelectron. 2014;58:287–307. https://doi.org/10.1016/j.bios.2014.02.049.

[136] Kormányos B, Horváth AK, Peintler G, Nagypál I. Inherent pitfalls in the simplified evaluation of kinetic curves. J Phys Chem A. 2007;111:8104–9. https://doi.org/10.1021/jp072817l.

[137] Kozma P, Hamori A, Cottier K, Kurunczi S, Horvath R. Grating coupled interferometry for optical sensing. Appl Phys B. 2009;97:5–8. https://doi.org/10.1007/s00340-009-3719-1.

[138] Patko D, Cottier K, Hamori A, Horvath R. Single beam grating coupled interferometry: high resolution miniaturized label-free sensor for plate based parallel screening. Opt Express. 2012;20:23162. https://doi.org/10.1364/oe.20.023162.

[139] Creoptix AG. The creoptix WAVEsystem. https://www.creoptix.com/products; 2021.

[140] Hohmann U, Nicolet J, Moretti A, Hothorn LA, Hothorn M. The SERK3 elongated allele defines a role for BIR ectodomains in brassinosteroid signalling. Nat Plants. 2018;4:345–51. https://doi.org/10.1038/s41477-018-0150-9.

[141] Hohmann U, Santiago J, Nicolet J, Olsson V, Spiga FM, Hothorn LA, et al. Mechanistic basis for the activation of plant membrane receptor kinases by SERK-family coreceptors. Proc Natl Acad Sci. 2018;115:3488–93. https://doi.org/10.1073/pnas.1714972115.

[142] Okuda S, Fujita S, Moretti A, Hohmann U, Doblas VG, Ma Y, et al. Molecular mechanism for the recognition of sequence-divergent CIF peptides by the plant receptor kinases GSO1/SGN3 and GSO2. Proc Natl Acad Sci. 2020;117:2693–703. https://doi.org/10.1073/pnas.1911553117.

[143] Moussu S, Broyart C, Santos-Fernandez G, Augustin S, Wehrle S, Grossniklaus U, et al. Structural basis for recognition of RALF peptides by LRX proteins during pollen tube growth. Proc Natl Acad Sci. 2020;202000100. https://doi.org/10.1073/pnas.2000100117.

[144] Lau K, Podolec R, Chappuis R, Ulm R, Hothorn M. Plant photoreceptors and their signaling components compete for COP1 binding via VP peptide motifs. EMBO J. 2019;38:1–18. https://doi.org/10.15252/embj.2019102140.

[145] Lorenzo-Orts L, Hohmann U, Zhu J, Hothorn M. Molecular characterization of CHAD domains as inorganic polyphosphate-binding modules. Life Sci Alliance. 2019;2: e201900385. https://doi.org/10.26508/lsa.201900385.

[146] Doll NM, Royek S, Fujita S, Okuda S, Chamot S, Stintzi A, et al. A two-way molecular dialogue between embryo and endosperm is required for seed development. Science (80-). 2020;367:431–5. https://doi.org/10.1126/science.aaz4131.

[147] Sandoval PJ, Santiago J. In vitro analytical approaches to study plant ligand–receptor interactions. Plant Physiol. 2020;182:1697–712. https://doi.org/10.1104/pp.19.01396.

[148] Andres F, Iamele L, Meyer T, Stüber JC, Kast F, Gherardi E, et al. Inhibition of the MET kinase activity and cell growth in MET-addicted cancer cells by bi-paratopic linking. J Mol Biol. 2019;431:2020–39. https://doi.org/10.1016/j.jmb.2019.03.024.

[149] Pitsawong W, Buosi V, Otten R, Agafonov RV, Zorba A, Kern N, et al. Dynamics of human protein kinase aurora a linked to drug selectivity. Elife. 2018;7:1–30. https://doi.org/10.7554/eLife.36656.

[150] Li G, Ferrie AM, Fang Y. Label-free profiling of ligands for endogenous GPCRs using a cell-based high-throughput screening technology. J Assoc Lab Autom. 2006;11: 181–7. https://doi.org/10.1016/j.jala.2006.06.001.

[151] Corning Inc. Corning epic BT system; 2021 (https://ecatalog.corning.com/life-sciences/b2c/US/en/Label-Free-Detection/Epic®-Benchtop/Corning®-Epic®-BT-System/p/5053?lang=en).

[152] Fang Y, Ferrie AM, Fontaine NH, Mauro J, Balakrishnan J. Resonant waveguide grating biosensor for living cell sensing. Biophys J. 2006;91:1925–40. https://doi.org/10.1529/biophysj.105.077818.

[153] Fang Y. Ligand–receptor interaction platforms and their applications for drug discovery. Expert Opin Drug Discov. 2012;7:969–88. https://doi.org/10.1517/17460441.2012.715631.

[154] Fang Y. Label-free biosensors for cell biology. Int J Electrochem. 2011;2011:1–16. https://doi.org/10.4061/2011/460850.

[155] Fang Y. Label-free cell-based assays with optical biosensors in drug discovery. Assay Drug Dev Technol. 2006;4:583–95. https://doi.org/10.1089/adt.2006.4.583.

[156] Orgovan N, Peter B, Bősze S, Ramsden JJ, Szabó B, Horvath R. Label-free profiling of cell adhesion: determination of the dissociation constant for native cell membrane adhesion receptor-ligand interaction. In: Fang Y, editor. Label-free biosens. methods drug discov. New York, NY: Springer New York; 2015. p. 1–390. https://doi.org/10.1007/978-1-4939-2617-6.

[157] Orgovan N, Ungai-Salánki R, Lukácsi S, Sándor N, Bajtay Z, Erdei A, et al. Adhesion kinetics of human primary monocytes, dendritic cells, and macrophages: dynamic cell adhesion measurements with a label-free optical biosensor and their comparison with end-point assays. Biointerphases. 2016;11:031001. https://doi.org/10.1116/1.4954789.

[158] Zaytseva N, Lynn JG, Wu Q, Mudaliar DJ, Sun H, Kuang PQ, et al. Resonant waveguide grating biosensor-enabled label-free and fluorescence detection of cell adhesion. Sensors Actuators B Chem. 2013;188:1064–72. https://doi.org/10.1016/j.snb.2013.08.012.

[159] Szekacs I, Orgovan N, Peter B, Kovacs B, Horvath R. Receptor specific adhesion assay for the quantification of integrin–ligand interactions in intact cells using a microplate based, label-free optical biosensor. Sensors Actuators B Chem. 2018;256: 729–34. https://doi.org/10.1016/j.snb.2017.09.208.

[160] Verrier F, An S, Ferrie AM, Sun H, Kyoung M, Deng H, et al. GPCRs regulate the assembly of a multienzyme complex for purine biosynthesis. Nat Chem Biol. 2011;7: 909–15. https://doi.org/10.1038/nchembio.690.

[161] Kurucz I, Peter B, Prosz A, Szekacs I, Horvath R, Erdei A. Label-free optical biosensor for on-line monitoring the integrated response of human B cells upon the engagement of stimulatory and inhibitory immune receptors. Sensors Actuators B Chem. 2017;240:528–35. https://doi.org/10.1016/j.snb.2016.09.015.

[162] Sztilkovics M, Gerecsei T, Peter B, Saftics A, Kurunczi S, Szekacs I, et al. Single-cell adhesion force kinetics of cell populations from combined label-free optical biosensor and robotic fluidic force microscopy. Sci Rep. 2020;10:61. https://doi.org/10.1038/s41598-019-56898-7.

[163] Wang R, Wang J, Liu Y, Zhang X, Liang X. Resonant waveguide grating based assays for colloidal aggregate detection and promiscuity characterization in natural products. RSC Adv. 2019;9:38055–64. https://doi.org/10.1039/C9RA06466D.

[164] Song H-P, Wang H, Zhao X, He L, Zhong H, Wu S-Q, et al. Label-free pharmacological profiling based on dynamic mass redistribution for characterization and authentication of hazardous natural products. J Hazard Mater. 2017;333:265–74. https://doi.org/10.1016/j.jhazmat.2017.03.025.

[165] Peter B, Ungai-Salanki R, Szabó B, Nagy AG, Szekacs I, Bösze S, et al. High-resolution adhesion kinetics of EGCG-exposed tumor cells on biomimetic interfaces: comparative monitoring of cell viability using label-free biosensor and classic end-point assays. ACS Omega. 2018;3:3882–91. https://doi.org/10.1021/acsomega.7b01902.

[166] Peter B, Farkas E, Forgacs E, Saftics A, Kovacs B, Kurunczi S, et al. Green tea polyphenol tailors cell adhesivity of RGD displaying surfaces: multicomponent models monitored optically. Sci Rep. 2017;7:42220. https://doi.org/10.1038/srep42220.

[167] Peter B, Lagzi I, Teraji S, Nakanishi H, Cervenak L, Zámbó D, et al. Interaction of positively charged gold nanoparticles with cancer cells monitored by an in situ label-free optical biosensor and transmission electron microscopy. ACS Appl Mater Interfaces. 2018;10:26841–50. https://doi.org/10.1021/acsami.8b01546.

[168] Németh A, Orgovan N, Sódar BW, Osteikoetxea X, Pálóczi K, Szabó-Taylor KÉ, et al. Antibiotic-induced release of small extracellular vesicles (exosomes) with surface-associated DNA. Sci Rep. 2017;7:8202. https://doi.org/10.1038/s41598-017-08392-1.

[169] Debreczeni ML, Szekacs I, Kovacs B, Saftics A, Kurunczi S, Gál P, et al. Human primary endothelial label-free biochip assay reveals unpredicted functions of plasma serine proteases. Sci Rep. 2020;10:3303. https://doi.org/10.1038/s41598-020-60158-4.

[170] Petersen R. Strategies using bio-layer interferometry biosensor technology for vaccine research and development. Biosensors. 2017;7:49. https://doi.org/10.3390/bios7040049.

[171] FortéBio. Label-free BLI detection systems. https://www.fortebio.com/products/label-free-bli-detection; 2021.

[172] Kamat V, Rafique A. Designing binding kinetic assay on the bio-layer interferometry (BLI) biosensor to characterize antibody-antigen interactions. Anal Biochem. 2017;536:16–31. https://doi.org/10.1016/j.ab.2017.08.002.

[173] Mechaly A, Cohen H, Cohen O, Mazor O. A biolayer interferometry-based assay for rapid and highly sensitive detection of biowarfare agents. Anal Biochem. 2016;506: 22–7. https://doi.org/10.1016/j.ab.2016.04.018.

[174] Özkumur E, Yalçın A, Cretich M, Lopez CA, Bergstein DA, Goldberg BB, et al. Quantification of DNA and protein adsorption by optical phase shift. Biosens Bioelectron. 2009;25:167–72. https://doi.org/10.1016/j.bios.2009.06.033.

[175] Daaboul GG, Vedula RS, Ahn S, Lopez CA, Reddington A, Ozkumur E, et al. LED-based Interferometric Reflectance Imaging Sensor for quantitative dynamic monitoring of biomolecular interactions. Biosens Bioelectron. 2011;26:2221–7. https://doi.org/10.1016/j.bios.2010.09.038.

[176] Daaboul GG, Gagni P, Benussi L, Bettotti P, Ciani M, Cretich M, et al. Digital detection of exosomes by interferometric imaging. Sci Rep. 2016;6:37246. https://doi.org/10.1038/srep37246.

[177] NanoView ExoView R100. https://www.nanoviewbio.com/exoview-r100-product; 2021.

[178] Fattinger C. Focal molography: coherent microscopic detection of biomolecular interaction. Phys Rev X. 2014;4:031024. https://doi.org/10.1103/PhysRevX.4.031024.

[179] Manghani S, Ramsden JJ. The efficiency of chemical detectors. J Biol Phys Chem. 2003;3:11–7. https://doi.org/10.4024/1030302.jbpc.03.01.

[180] McArthur SL, McLean KM, Kingshott P, St John HAW, Chatelier RC, Griesser HJ. Effect of polysaccharide structure on protein adsorption. Colloids Surfaces B Biointerfaces. 2000;17:37–48. https://doi.org/10.1016/S0927-7765(99)00086-7.

[181] Ramsden JJ. The specificity of biomolecular particle adhesion. Colloids Surfaces A Physicochem Eng Asp. 2000;165:25–38. https://doi.org/10.1016/S0927-7757(99)00411-2.

[182] Reichmuth AM, Zimmermann M, Wilhelm F, Frutiger A, Blickenstorfer Y, Fattinger C, et al. Quantification of molecular interactions in living cells in real time using a membrane protein nanopattern. Anal Chem. 2020;92:8983–91. https://doi.org/10.1021/acs.analchem.0c00987.

[183] Binnig G. Coherent signal picks out biomolecular interactions. Physics (College Park Md). 2014;7:84. https://doi.org/10.1103/Physics.7.84.

[184] Ramsden JJ. Protein adsorption kinetics. In: Malmsten M, editor. Biopolym. interfaces. 2nd ed. New York, NY: CRC Press; 2003. p. 928. https://doi.org/10.1201/9780824747343.

[185] Ramsden JJ, Schneider P. Membrane insertion and antibody recognition of a glycosylphosphatidylinositol-anchored protein: an optical study. Biochemistry. 1993;32:523–9. https://doi.org/10.1021/bi00053a017.

[186] Ramsden JJ. Puzzles and paradoxes in protein adsorption. Chem Soc Rev. 1995;24: 73. https://doi.org/10.1039/cs9952400073.

[187] Ramsden JJ. Kinetics of protein adsorption. In: Malmsten M, editor. Biopolym. interfaces. 1st ed. New York, NY: Marcel Dekker, Inc; 1998. p. 680.

[188] Migliorini E, Weidenhaupt M, Picart C. Practical guide to characterize biomolecule adsorption on solid surfaces (review). Biointerphases. 2018;13:06D303. https://doi.org/10.1116/1.5045122.

[189] Manzi BM, Werner M, Ivanova EP, Crawford RJ, Baulin VA. Simulations of protein adsorption on nanostructured surfaces. Sci Rep. 2019;9:4694. https://doi.org/10.1038/s41598-019-40920-z.

[190] Cooper MA, Williams DH. Kinetic analysis of antibody–antigen interactions at a supported lipid monolayer. Anal Biochem. 1999;276:36–47. https://doi.org/10.1006/abio.1999.4333.

[191] Kurrat R, Prenosil JE, Ramsden JJ. Kinetics of human and bovine serum albumin adsorption at silica–titania surfaces. J Colloid Interface Sci. 1997;185:1–8. https://doi.org/10.1006/jcis.1996.4528.

[192] Wojciechowski PW. Transport and adsorption of cells and proteis at interfaces. In: Brash J, editor. Interfacial phenom. bioprod. (biotechnology bioprocess. ser.) 1st ed. CRC Press; 1996. p. 528.

[193] Swenson H, Stadie NP. Langmuir's theory of adsorption: a centennial review. Langmuir. 2019;35:5409–26. https://doi.org/10.1021/acs.langmuir.9b00154.

[194] Ramsden JJ, Bachmanova GI, Archakov AI. Kinetic evidence for protein clustering at a surface. Phys Rev E. 1994;50:5072–6. https://doi.org/10.1103/PhysRevE.50.5072.

[195] Vergères G, Ramsden JJ. Regulation of the binding of myristoylated alanine-rich C kinase substrate (MARCKS) related protein to lipid bilayer membranes by calmodulin. Arch Biochem Biophys. 2000;378:45–50. https://doi.org/10.1006/abbi.2000.1809.

[196] Gelinsky-Wersing D, Wersing W, Pompe W. Bivalent kinetic binding model to surface plasmon resonance studies of antigen–antibody displacement reactions. Anal Biochem. 2017;518:110–25. https://doi.org/10.1016/j.ab.2016.11.012.

[197] Garrido G, Tikhomirov IA, Rabasa A, Yang E, Gracia E, Iznaga N, et al. Bivalent binding by intermediate affinity of nimotuzumab: a contribution to explain antibody clinical profile. Cancer Biol Ther. 2011;11:373–82. https://doi.org/10.4161/cbt.11.4.14097.

[198] Kirkbride KC, Townsend TA, Bruinsma MW, Barnett JV, Blobe GC. Bone morphogenetic proteins signal through the transforming growth factor-β type III receptor. J Biol Chem. 2008;283:7628–37. https://doi.org/10.1074/jbc.M704883200.

[199] Masel RI. Principles of adsorption and reaction on solid surfaces. 2nd ed.. New York, NY: Wiley; 1996.

[200] Feder J, Giaever I. Adsorption of ferritin. J Colloid Interface Sci. 1980;78:144–54. https://doi.org/10.1016/0021-9797(80)90502-0.

[201] Schaaf P, Talbot J. Surface exclusion effects in adsorption processes. J Chem Phys. 1989;91:4401–9. https://doi.org/10.1063/1.456768.

[202] Ramsden JJ. Concentration scaling of protein deposition kinetics. Phys Rev Lett. 1993;71:295–8. https://doi.org/10.1103/PhysRevLett.71.295.

[203] Jin X, Wang NHL, Tarjus G, Talbot J. Irreversible adsorption on nonuniform surfaces: the random site model. J Phys Chem. 1993;97:4256–8. https://doi.org/10.1021/j100119a003.

[204] Van Tassel PR, Viot P, Tarjus G, Talbot J. Irreversible adsorption of macromolecules at a liquid–solid interface: theoretical studies of the effects of conformational change. J Chem Phys. 1994;101:7064–73. https://doi.org/10.1063/1.468332.

[205] Van Tassel PR, Talbot J, Tarjus G, Viot P. Kinetics of irreversible adsorption with a particle conformational change: a density expansion approach. Phys Rev E. 1996;53:785–98. https://doi.org/10.1103/PhysRevE.53.785.

[206] Van Tassel PR, Viot P, Tarjus G. A kinetic model of partially reversible protein adsorption. J Chem Phys. 1997;106:761–70. https://doi.org/10.1063/1.473164.

[207] Van Tassel PR, Guemouri L, Ramsden JJ, Tarjus G, Viot P, Talbot J. A particle-level model of irreversible protein adsorption with a postadsorption transition. J Colloid Interface Sci. 1998;207:317–23. https://doi.org/10.1006/jcis.1998.5781.

[208] Brusatori MA, Van Tassel PR. A kinetic model of protein adsorption/surface-induced transition kinetics evaluated by the scaled particle theory. J Colloid Interface Sci. 1999;219:333–8. https://doi.org/10.1006/jcis.1999.6496.

[209] Calonder C, Van Tassel PR. Kinetic regimes of protein adsorption. Langmuir. 2001;17:4392–5. https://doi.org/10.1021/la001734s.

[210] Luthi PO, Ramsden JJ, Chopard B. Role of diffusion in irreversible deposition. Phys Rev E. 1997;55:3111–5. https://doi.org/10.1103/PhysRevE.55.3111.

[211] Bafaluy J, Senger B, Voegel J-C, Schaaf P. Effect of hydrodynamic interactions on the distribution of adhering Brownian particles. Phys Rev Lett. 1993;70:623–6. https://doi.org/10.1103/PhysRevLett.70.623.

[212] Gromenko O, Privman V. Random sequential adsorption of objects of decreasing size. Phys Rev E. 2009;79:011104. https://doi.org/10.1103/PhysRevE.79.011104.

[213] Ricci SM, Talbot J, Tarjus G, Viot P. Random sequential adsorption of anisotropic particles. II. Low coverage kinetics. J Chem Phys. 1992;97:5219–28. https://doi.org/10.1063/1.463988.

[214] Viot P, Tarjus G, Ricci SM, Talbot J. Random sequential adsorption of anisotropic particles. I. Jamming limit and asymptotic behavior. J Chem Phys. 1992;97:5212–8. https://doi.org/10.1063/1.463820.

[215] Adamczyk Z, Weroński P. Random sequential adsorption of spheroidal particles: kinetics and jamming limit. J Chem Phys. 1996;105:5562–73. https://doi.org/10.1063/1.472409.

[216] Fernández A, Ramsden JJ. On adsorption-induced denaturation of folded proteins. J Biol Phys Chem. 2001;1:81–4. https://doi.org/10.4024/12FE01L01.02.

[217] Mason T, Pineda AR, Wofsy C, Goldstein B. Effective rate models for the analysis of transport-dependent biosensor data. Math Biosci. 1999;159:123–44. https://doi.org/10.1016/S0025-5564(99)00023-1.

[218] Schuck P, Zhao H. The role of mass transport limitation and surface heterogeneity in the biophysical characterization of macromolecular binding processes by SPR biosensing. In: Mol NJ, Fisher MJE, editors. Surface Plasmon Resonance, Methods and Protocols. Springer; 2010. p. 15–54.

[219] Quinn JG, Steffek M, Bruning JM, Frommlet A, Mulvihill MM. Unlocking latent kinetic information from label-free binding. Sci Rep. 2019;9:18389. https://doi.org/10.1038/s41598-019-54485-4.

[220] Watkins RW, Robertson CR. A total internal-reflection technique for the examination of protein adsorption. J Biomed Mater Res. 1977;11:915–38. https://doi.org/10.1002/jbm.820110611.

[221] Lok BK, Cheng Y-L, Robertson CR. Total internal reflection fluorescence: a technique for examining interactions of macromolecules with solid surfaces. J Colloid Interface Sci. 1983;91:87–103. https://doi.org/10.1016/0021-9797(83)90316-8.

[222] Lok BK, Cheng Y-L, Robertson CR. Protein adsorption on crosslinked polydimethylsiloxane using total internal reflection fluorescence. J Colloid Interface Sci. 1983;91:104–16. https://doi.org/10.1016/0021-9797(83)90317-X.

[223] Sjölander S, Urbaniczky C. Integrated fluid handling system for biomolecular interaction analysis. Anal Chem. 1991;63:2338–45. https://doi.org/10.1021/ac00020a025.

[224] Christensen LLH. Theoretical analysis of protein concentration determination using biosensor technology under conditions of partial mass transport limitation. Anal Biochem. 1997;249:153–64. https://doi.org/10.1006/abio.1997.2182.

[225] Myszka DG, He X, Dembo M, Morton TA, Goldstein B. Extending the range of rate constants available from BIACORE: interpreting mass transport-influenced binding data. Biophys J. 1998;75:583–94. https://doi.org/10.1016/S0006-3495(98)77549-6.

[226] Brusatori MA, Tie Y, Van Tassel PR. Protein adsorption kinetics under an applied electric field: an optical waveguide lightmode spectroscopy study. Langmuir. 2003;19:5089–97. https://doi.org/10.1021/la0269558.

[227] Van Tassel PR. Protein adsorption kinetics: influence of substrate electric potential. In: Déjardin P, editor. Proteins at solid–liquid interfaces. Berlin, Heidelberg: Springer Berlin Heidelberg; 2006. p. 1–22.

[228] Anderson JJ, Moldoveanu S. Numerical simulation of convective diffusion at a rectangular channel flow electrode. J Electroanal Chem Interfacial Electrochem. 1984;179:107–17. https://doi.org/10.1016/S0022-0728(84)80280-6.

[229] Compton RG, Pilkington MBG, Stearn GM. Mass transport in channel electrodes. The application of the backwards implicit method to electrode reactions (EC, ECE and DISP) involving coupled homogeneous kinetics. J Chem Soc Faraday Trans 1 Phys Chem Condens Phases. 1988;84:2155. https://doi.org/10.1039/f19888402155.

[230] Hansen R, Bruus H, Callisen TH, Hassager O. Transient convection, diffusion, and adsorption in surface-based biosensors. Langmuir. 2012;28:7557–63. https://doi.org/10.1021/la3000763.

[231] Lebedev K, Mafé S, Stroeve P. Convection, diffusion and reaction in a surface-based biosensor: modeling of cooperativity and binding site competition on the surface and in the hydrogel. J Colloid Interface Sci. 2006;296:527–37. https://doi.org/10.1016/j.jcis.2005.09.032.

[232] Lynn NS, Šípová H, Adam P, Homola J. Enhancement of affinity-based biosensors: effect of sensing chamber geometry on sensitivity. Lab Chip. 2013;13:1413. https://doi.org/10.1039/c2lc41184a.

[233] Gervais T, Jensen KF. Mass transport and surface reactions in microfluidic systems. Chem Eng Sci. 2006;61:1102–21. https://doi.org/10.1016/j.ces.2005.06.024.

[234] Yang C-K, Chang J-S, Chao SD, Wu K-C. Effects of diffusion boundary layer on reaction kinetics of immunoassay in a biosensor. J Appl Phys. 2008;103:084702. https://doi.org/10.1063/1.2909980.

[235] Murthy C, Armani A. Mass transport effects in suspended waveguide biosensors integrated in microfluidic channels. Sensors. 2012;12:14327–43. https://doi.org/10.3390/s121114327.

[236] Selmi M, Gazzah MH, Belmabrouk H. Optimization of microfluidic biosensor efficiency by means of fluid flow engineering. Sci Rep. 2017;7:5721. https://doi.org/10.1038/s41598-017-06204-0.

[237] Vijayendran RA, Ligler FS, Leckband DE. A computational reaction−diffusion model for the analysis of transport-limited kinetics. Anal Chem. 1999;71:5405–12. https://doi.org/10.1021/ac990672b.

[238] Nernst W. Theorie der Reaktionsgeschwindigkeit in heterogenen Systemen. Zeitschrift Für Phys Chemie. 1904;47U:52–5. https://doi.org/10.1515/zpch-1904-4704.

[239] Lévêque AM. Les lois de la transmission de chaleur par convection. Ann Des Mines. 1928;13:201–409.

[240] Levich VG. Physicochemical hydrodynamics. Physicochem. hydrodyn. Englewood Cliffs, N.J.: Prentice-Hall, Inc.; 1962. p. 112–6.

[241] Blaedel WJ, Olson CL, Sharma LR. The tubular platinum electrode. Anal Chem. 1963;35:2100–3. https://doi.org/10.1021/ac60206a034.

[242] Blaedel WJ, Klatt LN. Reversible charge transfer at the tubular platinum electrode. Anal Chem. 1966;38:879–83. https://doi.org/10.1021/ac60239a021.

[243] Klatt LN, Blaedel WJ. Quasi-reversible and irreversible charge transfer at the tubular electrode. Anal Chem. 1967;39:1065–72. https://doi.org/10.1021/ac60254a014.

[244] Matsuda H. Zur theorie der stationären strom-spannungs-kurven von redox-elektrodenreaktionen in hydrodynamischer voltammetrie. J Electroanal Chem Interfacial Electrochem. 1967;15:109–27. https://doi.org/10.1016/0022-0728(67)85016-2.

[245] Meyer RE, Banta MC, Lantz PM, Posey FA. Chronopotentiometry and voltammetry of the Ag-AgCl electrode in flowing streams. I Experimental J Electroanal Chem Interfacial Electrochem. 1971;30:345–58. https://doi.org/10.1016/0368-1874(71)87019-3.

[246] Posey FA, Meyer RE. Chronopotentiometry and voltammetry of the Ag-AgCl electrode in flowing streams. II. Thereotical. J Electroanal Chem Interfacial Electrochem. 1971;30:359–73. https://doi.org/10.1016/0368-1874(71)87020-X.

[247] Elbicki JM, Morgan DM, Weber SG. Theoretical and practical limitations on the optimization of amperometric detectors. Anal Chem. 1984;56:978–85. https://doi.org/10.1021/ac00270a026.

[248] Compton RG, Unwin PR. Channel and tubular electrodes. J Electroanal Chem Interfacial Electrochem. 1986;205:1–20. https://doi.org/10.1016/0022-0728(86)90219-6.

[249] Ramsden JJ. Review of new experimental techniques for investigating random sequential adsorption. J Stat Phys. 1993;73:853–77. https://doi.org/10.1007/BF01052813.

[250] Kurrat R, Ramsden JJ, Prenosil JE. Kinetic model for serum albumin adsorption : experimental verification. J Chem Soc Faraday Trans. 1994;90:587. https://doi.org/10.1039/ft9949000587.

[251] Kovacs B, Saftics A, Biro A, Kurunczi S, Szalontai B, Kakasi B, et al. Kinetics and structure of self-assembled flagellin monolayers on hydrophobic surfaces in the presence of hofmeister salts: experimental measurement of the protein interfacial tension at the nanometer scale. J Phys Chem C. 2018;122:21375–86. https://doi.org/10.1021/acs.jpcc.8b05026.

[252] Karlsson R, Roos H, Fägerstam L, Persson B. Kinetic and concentration analysis using BIA technology. Methods. 1994;6:99–110. https://doi.org/10.1006/meth.1994.1013.

[253] Biacore assay handbook. AA. GE Healthcare Bio-Sciences AB; 2012.

[254] Pol E, Roos H, Markey F, Elwinger F, Shaw A, Karlsson R. Evaluation of calibration-free concentration analysis provided by Biacore™ systems. Anal Biochem. 2016;510:88–97. https://doi.org/10.1016/j.ab.2016.07.009.

[255] Karlsson R. Biosensor binding data and its applicability to the determination of active concentration. Biophys Rev. 2016;8:347–58. https://doi.org/10.1007/s12551-016-0219-5.

[256] Moradi-Monfared S, Krishnamurthy V, Cornell BC. Chemical kinetics and mass transport in an ion channel based biosensor. 49th IEEE conf. decis. control. IEEE; 2010. p. 4685–90. https://doi.org/10.1109/CDC.2010.5718085.

[257] Moradi-Monfared S, Krishnamurthy V, Cornell B. A molecular machine biosensor: construction, predictive models and experimental studies. Biosens Bioelectron. 2012;34:261–6. https://doi.org/10.1016/j.bios.2012.02.018.

[258] Abolfath-Beygi M, Krishnamurthy V. Biosensor arrays for estimating molecular concentration in fluid flows. IEEE Trans Signal Process. 2014;62:239–51. https://doi.org/10.1109/TSP.2013.2287680.

[259] Schuck P, Minton AP. Analysis of mass transport-limited binding kinetics in evanescent wave biosensors. Anal Biochem. 1996;240:262–72. https://doi.org/10.1006/abio.1996.0356.

[260] Wasilewska M, Adamczyk Z, Sadowska M, Boulmedais F, Cieśla M. Mechanisms of fibrinogen adsorption on silica sensors at various pHs: experiments and theoretical modeling. Langmuir. 2019;35:11275–84. https://doi.org/10.1021/acs.langmuir.9b01341.

[261] Dejardin P, Le MT, Johner A, Wittmer J. Adsorption rate in the convection-diffusion model. Langmuir. 1994;10:3898–901. https://doi.org/10.1021/la00022a081.

[262] Déjardin P, Vasina EN. An accurate simplified data treatment for the initial adsorption kinetics in conditions of laminar convection in a slit: application to protein adsorption. Colloids Surfaces B Biointerfaces. 2004;33:121–7. https://doi.org/10.1016/j.colsurfb.2003.09.005.

[263] Richards FJ. A flexible growth function for empirical use. J Exp Bot. 1959;10:290–301. https://doi.org/10.1093/jxb/10.2.290.

[264] Kovacs N, Patko D, Orgovan N, Kurunczi S, Ramsden JJ, Vonderviszt F, et al. Optical anisotropy of flagellin layers: in situ and label-free measurement of adsorbed protein orientation using OWLS. Anal Chem. 2013;85:5382–9. https://doi.org/10.1021/ac3034322.

[265] Kovacs B, Patko D, Szekacs I, Orgovan N, Kurunczi S, Sulyok A, et al. Flagellin based biomimetic coatings: from cell-repellent surfaces to highly adhesive coatings. Acta Biomater. 2016;42:66–76. https://doi.org/10.1016/j.actbio.2016.07.002.

[266] Norde W. Adsorption of proteins from solution at the solid-liquid interface. Adv Colloid Interface Sci. 1986;25:267–340. https://doi.org/10.1016/0001-8686(86)80012-4.

[267] Norde W, Lyklema J. Why proteins prefer interfaces. J Biomater Sci Polym Ed. 1991;2:183–202. https://doi.org/10.1080/09205063.1991.9756659.

[268] Norde W. My voyage of discovery to proteins in flatland … and beyond. Colloids Surfaces B Biointerfaces. 2008;61:1–9. https://doi.org/10.1016/j.colsurfb.2007.09.029.

[269] Ramsden JJ, Prenosil JE. Effect of ionic strength on protein adsorption kinetics. J Phys Chem. 1994;98:5376–81. https://doi.org/10.1021/j100071a031.

[270] Halthur TJ, Elofsson UM. Multilayers of charged polypeptides as studied by in situ ellipsometry and quartz crystal microbalance with dissipation. Langmuir. 2004;20:1739–45. https://doi.org/10.1021/la035475t.

[271] Müller MT, Yan X, Lee S, Perry SS, Spencer ND. Lubrication properties of a brushlike copolymer as a function of the amount of solvent absorbed within the brush. Macromolecules. 2005;38:5706–13. https://doi.org/10.1021/ma0501545.

[272] Konradi R, Textor M, Reimhult E. Using complementary acoustic and optical techniques for quantitative monitoring of biomolecular adsorption at interfaces. Biosensors. 2012;2:341–76. https://doi.org/10.3390/bios2040341.

[273] Köβlinger C, Uttenthaler E, Drost S, Aberl F, Wolf H, Brink G, et al. Comparison of the QCM and the SPR method for surface studies and immunological applications. Sensors Actuators B Chem. 1995;24:107–12. https://doi.org/10.1016/0925-4005(95)85023-6.

[274] Bittrich E, Rodenhausen KB, Eichhorn K-J, Hofmann T, Schubert M, Stamm M, et al. Protein adsorption on and swelling of polyelectrolyte brushes: a simultaneous ellipsometry-quartz crystal microbalance study. Biointerphases. 2010;5:159–67. https://doi.org/10.1116/1.3530841.

[275] Rodenhausen KB, Guericke M, Sarkar A, Hofmann T, Ianno N, Schubert M, et al. Micelle-assisted bilayer formation of cetyltrimethylammonium bromide thin films studied with combinatorial spectroscopic ellipsometry and quartz crystal microbalance techniques. Thin Solid Films. 2011;519:2821–4. https://doi.org/10.1016/j.tsf.2010.11.078.

[276] Laskarakis A, Logothetidis S. Coupling spectroscopic ellipsometry and quartz crystal microbalance to study organic films at the solid–liquid interface. In: Hinrichs K, Eichhorn K-J, editors. Ellipsom. funct. org. surfaces film. Cham: Springer International Publishing; 2018. p. 437–58. https://doi.org/10.1007/978-3-319-75895-4.

[277] MicroVacuum Ltd. OWLS QCM 3000 biosensor system. https://www.owls-sensors.com/qcm-quartz-crystal-microbalance-owls-electrochemical-sensor; 2021.

[278] Agocs E, Kozma P, Nador J, Hamori A, Janosov M, Kalas B, et al. Grating coupled optical waveguide interferometry combined with in situ spectroscopic ellipsometry to monitor surface processes in aqueous solutions. Appl Surf Sci. 2017;421:289–94. https://doi.org/10.1016/j.apsusc.2016.07.166.

[279] Moirangthem RS, Chang Y-C, Hsu S-H, Wei P-K. Surface plasmon resonance ellipsometry based sensor for studying biomolecular interaction. Biosens Bioelectron. 2010;25:2633–8. https://doi.org/10.1016/j.bios.2010.04.037.

[280] Pant U, Mohapatra S, Moirangthem RS. Total internal reflection ellipsometry based SPR sensor for studying biomolecular interaction. Mater Today Proc. 2020;28:254–7. https://doi.org/10.1016/j.matpr.2020.01.602.

[281] Nador J, Kalas B, Saftics A, Agocs E, Kozma P, Korosi L, et al. Plasmon–enhanced two–channel in situ Kretschmann ellipsometry of protein adsorption , cellular adhesion and polyelectrolyte deposition on titania nanostructures. Opt Express. 2016;24:4812–23.

[282] Kalas B, Nador J, Agocs E, Saftics A, Kurunczi S, Fried M, et al. Protein adsorption monitored by plasmon-enhanced semi-cylindrical Kretschmann ellipsometry. Appl Surf Sci. 2017;421:585–92. https://doi.org/10.1016/j.apsusc.2017.04.064.

[283] Kalas B, Ferencz K, Saftics A, Czigany Z, Fried M, Petrik P. Bloch surface waves biosensing in the ultraviolet wavelength range – Bragg structure design for investigating protein adsorption by in situ Kretschmann-Raether ellipsometry. Appl Surf Sci. 2021;536:147869. https://doi.org/10.1016/j.apsusc.2020.147869.

[284] Granéli A, Edvardsson M, Höök F. DNA-based formation of a supported, three-dimensional lipid vesicle matrix probed by QCM-D and SPR. ChemPhysChem. 2004;5:729–33. https://doi.org/10.1002/cphc.200301061.

[285] Malmström J, Agheli H, Kingshott P, Sutherland DS. Viscoelastic modeling of highly hydrated laminin layers at homogeneous and nanostructured surfaces: quantification of protein layer properties using QCM-D and SPR. Langmuir. 2007;23:9760–8. https://doi.org/10.1021/la701233y.

[286] Thiele S, Andersson J, Dahlin A, Hailes RLN. Tuning the thermoresponsive behavior of surface-attached PNIPAM networks: varying the crosslinker content in SI-ATRP. Langmuir. 2021;37:3391–8. https://doi.org/10.1021/acs.langmuir.0c03545.

[287] Ouberai MM, Xu K, Welland ME. Effect of the interplay between protein and surface on the properties of adsorbed protein layers. Biomaterials. 2014;35:6157–63. https://doi.org/10.1016/j.biomaterials.2014.04.012.

[288] Hu Y, Jin J, Han Y, Yin J, Jiang W, Liang H. Study of fibrinogen adsorption on poly (ethylene glycol)-modified surfaces using a quartz crystal microbalance with dissipation and a dual polarization interferometry. RSC Adv. 2014;4:7716. https://doi.org/10.1039/c3ra46934d.

[289] Peter B, Farkas E, Forgacs E, Saftics A, Kovacs B, Kurunczi S, et al. Green tea polyphenol tailors cell adhesivity of RGD displaying surfaces: multicomponent models monitored optically. Sci Rep. 2017;7:42220. https://doi.org/10.1038/srep42220.

[290] Runge AF, Rasmussen NC, Saavedra SS, Mendes SB. Determination of anisotropic optical constants and surface coverage of molecular films using polarized visible ATR spectroscopy. application to adsorbed cytochrome c films. J Phys Chem B. 2005;109:424–31. https://doi.org/10.1021/jp045727e.

[291] Reimhult E, Larsson C, Kasemo B, Höök F. Simultaneous surface plasmon resonance and quartz crystal microbalance with dissipation monitoring measurements of biomolecular adsorption events involving structural transformations and variations in coupled water. Anal Chem. 2004;76:7211–20. https://doi.org/10.1021/ac0492970.

[292] Chen JY, Penn LS, Xi J. Quartz crystal microbalance: sensing cell-substrate adhesion and beyond. Biosens Bioelectron. 2018;99:593–602. https://doi.org/10.1016/j.bios.2017.08.032.

[293] Lord MS, Modin C, Foss M, Duch M, Simmons A, Pedersen FS, et al. Extracellular matrix remodelling during cell adhesion monitored by the quartz crystal microbalance. Biomaterials. 2008;29:2581–7. https://doi.org/10.1016/j.biomaterials.2008.03.002.

[294] Grieshaber D, MacKenzie R, Vörös J, Reimhult E. Electrochemical Biosensors - Sensor Principles and Architectures. Sensors. 2008;8:1400–58. https://doi.org/10.3390/s80314000.

[295] Zhang Y, Du B, Chen X, Ma H. Convergence of Dissipation and ImpedanceAnalysis of Quartz Crystal Microbalance Studies. Anall Chem. 2009;81:642–8. https://doi.org/10.1021/ac8019762.

[296] Horvath R, Ramsden JJ. Quasi-isotropic Analysis of Anisotropic Thin Films on Optical Waveguides. Langmuir. 2007;23(18):9330–4. https://doi.org/10.1021/la701405n.

[297] Horváth R, Fricsovszky G, Papp E. Application of the optical waveguide lightmode spectroscopy to monitor lipid bilayer phase transition. Biosens Bioelectron. 2003;18:415–28. https://doi.org/10.1016/S0956-5663(02)00154-9.

[298] Horvath R, McColl J, Yakubov GE, Ramsden JJ. Structural hysteresis and hierarchy in adsorbed glycoproteins. J Chem Phys. 2008;129:071102. https://doi.org/10.1063/1.2968127.

[299] Horvath R, Pedersen HC, Skivesen N. Monitoring of living cell attachment and spreading using reverse symmetry waveguide sensing. Appl Phys Lett. 2005;86:071101. https://doi.org/10.1063/1.1862756.

[300] Horvath R, Kobzi B, Keul H, Moeller M, Kiss É. Molecular Interaction of a New Antibacterial Polymer with a Supported Lipid Bilayer Measured by an in situ Label-Free Optical Technique. J Mol Ssci. 2013;14(5):9722–36. https://doi.org/10.3390/ijms14059722.

[301] Juhasz K, Horvath R. Intrinsic structure of biological layers: Vertical inhomogeneity profiles characterized by label-free optical waveguide biosensors. Sens Actuators B Chem. 2014;200:297–303. https://doi.org/10.1016/j.snb.2014.04.064.

[302] Kovacs B, Horvath R. Modeling of Label-Free Optical Waveguide Biosensors with Surfaces Covered Partially by Vertically Homogeneous and Inhomogeneous Films. J Sens. 2019;2019:1762450. https://doi.org/10.1155/2019/1762450.

[303] A sensitivity metric and software to guide the analysis of soft films measured by a quartz crystal microbalance. Analyst. 2016;141:2911–9. https://doi.org/10.1039/C6AN00143B.

[304] MATLAB. version R2015a. Natick, Massachusetts: The MathWorks Inc. 2015.